Università degli Studi di Ferrara
Corso di Dottorato in Fisica
Dipartimento di Fisica e Scienze della Terra

Physics (DM 45/2013)

Advanced Techniques for Border Security: Contributions to the ENTRANCE and MULTISCAN 3D Projects

Candidate
Jessica Carolina
Delgado Alvarez

Supervisors
Prof. Fabio Mantovani

Prof. Sandra Moretto

PhD Coordinator
Prof. Paolo Lenisa

ciclo XXXVII, 2021-2024

Università degli Studi di Ferrara, Dipartimento di Fisica e Scienze della Terra.

Acknowledgments

First and foremost, I would like to express my deepest gratitude to my family for their constant support and encouragement throughout this journey. To my parents, whose love, guidance, and sacrifices have been the the foundation of my achievements.

To my sister and her husband, whose presence and support have been invaluable. I am also deeply grateful to my little brother and my two nephews, whose love and enthusiasm have been a source of motivation.

A special thanks goes to my boyfriend, Alessandro, whose love, support, and constant companionship have been essential throughout this journey.

I am profoundly thankful to my supervisors, Sandra and Felix, for their exceptional guidance, insightful feedback, and constant support. Your expertise and encouragement have been crucial to the completion of this thesis, and I have learned immensely from both of you.

Thank you all for your invaluable contributions to this journey.

Jessica Delgado

Abstract

The objective of this Ph.D. thesis is to make significant contributions to the advancement of neutron interrogation and photofission techniques within the framework of the ENTRANCE and MULTISCAN 3D projects. Both are EU-funded initiatives dedicated to developing and testing innovative, non-intrusive inspection systems to combat the illicit trafficking of hazardous materials or contraband items in cross-border cargo containers. This research encompasses simulation studies, experimental testing, participation in field campaigns, and the development of novel detection systems.

First, this work involved a detailed simulation study of the tagged neutron interrogation system using 14 MeV neutrons within the ENTRANCE project. The simulation focused on optimizing the system's geometry and provided valuable insights into key aspects such as time-of-flight spectra, energy deposition, and back-scattered neutron effects. Furthermore, this thesis presents the results of field tests conducted to evaluate the performance of the neutron interrogation system developed as part of the ENTRANCE project. These tests, carried out at the Port of Rijeka in May 2023, demonstrated the system's high accuracy in identifying explosives and moderate effectiveness in detecting drugs across a total of 18 mock-up containers and 18 commercial containers.

This research also explored the use of the ^{9}Be(d,n)^{10}B nuclear reaction to generate the neutron source needed for the interrogation technique in the MULTISCAN 3D project. This approach was motivated by the need to replace the tritium-based neutron source (14 MeV) employed in ENTRANCE, thereby addressing safety and logistical challenges associated with tritium-based systems. Experiments conducted at the Van de Graaff accelerator (INFN in Legnaro) successfully demonstrated the ability of this reaction to produce a continuous neutron spectrum. The detection of gamma-ray peaks in certain materials further confirmed the reaction's effectiveness and its potential for neutron interrogation applications.

Additionally, this thesis introduces two innovative detection systems for photofission applications in both projects. The first is a ZnS:Ag/LiBO/PDMS neutron scintillator, which demonstrated excellent thermal neutron detection efficiency, flexibility, and strong gamma-ray rejection capabilities. The second system is a compact gamma-ray detection unit consisting of an organic scintillator coupled with a SiPM array. This setup was evaluated in various configurations, including two organic scintillators (EJ-276G and EJ-309) and three SiPM arrays (AdvanSiD-NUV, Hamamatsu, and Ketek). Each configuration was studied in terms of its energy resolution, time resolution, and neutron/gamma-ray discrimination.

Contents

List of Figures

List of Tables

Glossary

ABCD	Acquisition and Broadcast of Collected Data
API	Active Photon Interrogation
APT	Associated Particle Technique
BCP RPMs	Border Control Point Radiation Portal Monitor
BF_3	Boron-trifluoride
CBORD	Effective Container Inspection at BORDer Control Points
CBRN-E	Chemical, Biological, Radiological and Nuclear substances and Explosive
CT	Computed Tomography
DC	Direct Current
DCFD	Digital Constant Fraction Discrimination
DAQ	Data Acquisition
DMMC	Declared vs Measured Mass Consistency
EJ-309	Neutron/gamma-ray PSD liquid scintillator
EJ-301	High-flash point neutron/gamma-ray PSD liquid scintillator
EJ-276	Neutron/gamma-ray PSD plastic scintillator
EJ-276G	Neutron/gamma-ray PSD plastic scintillator, with green fluorescence
EJ-200	Plastic scintillator
ENARTIS	ENTRANCE Automated Risk Assessment, Threat Recognition and Information Sharing Platform
ENTRANCE	EfficieNT Risk-bAsed iNspection of freight Crossing bordErs without disrupting business
EURITRACK	EURopean Illicit TRAfficking Countermeasures Kit
EU	European Union
FPGA	Field Programmable Gate Array
FoM	Figure of Merit

GEANT4	GEometry ANd Tracking
GRR	Gamma Rejection Ratio
HR-XRD	High-Resolution X-ray Diffraction
ICS	Inverse Compton Scattering
INFN-LNL	National Institute of Nuclear Physics in Legnaro
K-NN	k-nearest Neighbors
$LaBr_3$:Ce	Cerium Activated Lanthanum Bromide
LiBO	Lithium Tetraborate
LPAs	Laser-plasma Accelerators
MCNP	Monte Carlo N-Particle Transport
MISE	Italian Ministry for Economic Development
MPPC	Multi-Pixel Photon Counter
NaCl	Sodium Chloride
NaI:Tl	Sodium-doped Cesium Iodide
NUV	Near Ultraviolet Light
NRF	Nuclear Resonance Fluorescence
NR	Nuclear and Radioactive
PENELOPE	Penetration and ENErgy LOss of Positrons and Electrons
PET	Polyethylene Terephthalate
PENTRIT	Pentaerythritol Tetranitrate
PDE	Photon Detection Efficiency
PMT	Photomultiplier
PSD	Pulse Shape Discrimination
ROI	Region of Interest
RPM	Radiation Portal Monitors
R&D	Research and Development
RRTNIS	Rapidly Relocatable Tagged Neutron Inspection System
SEM-EDS	Scanning Electron Microscopy-Energy Dispersive X-ray Spectrometry
SiPM	Silicon Photomultiplier
SMANDRA	Sistema Mobile per Analisi Non Distruttive e RAdiometriche
SMEs	Small and Medium-sized Enterprises
SODERN	Space Optronics and Neutron Technology

SNM	Special Nuclear Material
SWaP	Size, Weight, and Power
TNIS	Tagged Neutron Inspection System
ToF	Time-of-Flight
TNT	Trinitrotoluene
YAP:Ce	Cerium-doped Yttrium Aluminum Perovskite
ZnS:Ag	Silver-activated Zinc Sulfide

Chapter 1

Introduction

The transportation of goods via maritime, land, or air routes is fundamental to the functioning of our global economy, facilitating trade and contributing to economic growth and development worldwide. Goods, commonly called cargo or freight, are transported across borders and regions, encompassing a wide range of products from raw materials, manufactured products, food items, machinery, and consumer goods. The efficient cargo movement is essential for sustaining international trade, creating job opportunities, and fostering economic cooperation among nations.

The European Union (EU) holds a significant position in global trade due to its open trade policies, positioning it as a primary player worldwide and creating favorable conditions for commercial activities. Every day, the EU performed substantial trade, exporting hundreds of millions of euros worth of goods and importing a similar value. It is recognized as one of the largest exporters of manufactured goods and services globally, and it serves as the primary export market for around 80 countries, in contrast, the United States serves as the primary trading partner for just over 20 countries [1]. Additionally, the EU actively promotes trade by eliminating barriers within its member states and cultivating trade relationships with other nations, particularly prioritizing openness with developing countries. In 2022, the EU's goods exports comprised 16% of global exports, with imports representing an equivalent value. This firmly establishes the EU as one of the world's leading trade entities, alongside the US and China [1, 2].

Within the global trade landscape, the maritime industry assumes a crucial role, facilitating the movement of over 95% of the world's trade volume. This industry operates a vast network of merchant vessels, annually transporting billions of tons of goods and linking producers to consumers worldwide [3]. Particularly within economic zones like the EU, nearly 90% of the EU's external freight trade relies on maritime transport [4]. Thus, the efficiency and reliability of maritime transport infrastructure, including ports, terminals, and shipping lanes, are pivotal for ensuring the smooth transit of goods and their timely delivery to global markets.

However, confirming and ensuring the legal transportation of goods within each container is an impossible task. While the majority of trade flowing through EU ports is legitimate, these ports also face the infiltration of illegal goods by criminal networks. Only a very small percentage of the vast volume of containers in the EU zone undergo physical inspection each year, making the detection of illicit goods very challenging. Criminal networks exploit vulnerabilities in transportation and port security systems to smuggle illegal items, including drugs, illegal tobacco, weapons, and contraband. Despite efforts to combat such activities through enhanced regulations and surveillance measures, the large volume of cargo and the limited capacity for physical inspections present significant obstacles in detecting and preventing illicit trade [5].

The consequences of illicit trade are transmitted across societies, impacting governance, public health, and security. These actions diminish confidence in government institutions and contribute to instability, presenting significant risks to national security. For instance, cigarette smuggling and illicit trade in tobacco products result in an estimated loss of 10 billion euros to the EU budget annually [6]. Moreover, these illegal practices often finance organized crime, with a particular focus on vulnerable populations, undermining efforts to discourage tobacco use.

On the other hand, the cocaine trade causes public health crises, violent crime, corruption, and societal decay. This illicit market fuels addiction, violence, and instability, with an estimated 3.7 million Europeans consuming cocaine annually, leading to around 6.000 overdose deaths yearly in the EU. Confiscations of cocaine in the EU have surged to record levels, with over 300 tons seized annually in recent years. Only in Belgium, authorities confiscated a record of 121 tons of cocaine at the port of Antwerp in 2023, marking a 10 percent increase over the previous year [7].

Beyond drugs and tobacco, illicit trade extends to weapons and explosives, posing grave security risks. Terrorist attacks often involve firearms, explosives, and even nuclear materials, making them a growing threat to public safety. Criminals hide these dangerous items in cargo or personal luggage, creating major challenges for security authorities who work to control this trade and prevent attacks.

Intensified efforts have been undertaken to combat these threats and illegal trades, aiming to safeguard communities and ensure security. However, traditional inspection methods struggle to uncover illicit materials hidden within cargo containers, often yielding incomplete or unreliable results. This emphasizes the urgent need for innovative solutions to strengthen border security and effectively combat illicit trade. Addressing these challenges demands a multifaceted approach, including technological innovation, international cooperation, and robust regulatory frameworks.

The present technologies employed for container inspection are ineffective and unreliable, leading to prolonged inspection duration. As a result, inspections predominantly focus on cargoes with irregular documentation or those flagged by intelligence services. Hence, all relevant cargo details, including quantity, contents, weight, and destination, must be analyzed before inspections are conducted. If an irregularity is found containers are initially scanned using X-ray technology, allowing authorities to reveal unusual shapes or densities that might indicate hidden compartments or illicit materials inside the container. This scanning process typically takes a few minutes, depending on the scanner, as some fast path-through X-ray scans can take less than one minute. This is followed by an additional fifteen minutes for evaluating the X-ray images [8]. Density meters are also utilized to identify significant variations in cargo density, which may indicate hidden compartments or undeclared materials. If suspicious items are found during initial inspections, further examinations may involve the full opening of the container, a process that can be time-consuming, and then any substances identified as potentially illicit undergo chemical testing, which requires taking samples and conducting tests, adding minutes to the inspection time.

On the other hand, detecting illicit trafficking of nuclear materials, particularly Special Nuclear Material (SNM) such as ^{235}U or ^{239}Pu, is crucial due to their potential use in nuclear weapon production. Additionally, it is important to detect radiological dispersal devices (RDDs), also known as "dirty bombs", which combine radioactive materials with conventional explosives. Common radioactive materials used in these devices are typically sourced from medical or industrial applications, such as ^{137}Cs or ^{60}Co. To address these threats, radiation detection and identification equipment are extensively employed by front-line officers and installed at strategic checkpoints, including road and rail border crossings, airports, and seaports [9].

Nevertheless, in homeland security applications, nuclear materials are often well shielded to evade passive detection. SNM, in particular, naturally emit neutrons and/or gamma rays, but these emissions are typically of low intensity and low energy. As a result, accurate detection and quantification of well-shielded nuclear materials using passive techniques is nearly impossible [10].

In the search to mitigate illicit trafficking and address the time-consuming and inefficient inspection systems currently placed at border controls, the ENTRANCE and MULTISCAN 3D projects, both EU-funded initiatives, aim to develop and validate a comprehensive, user-based toolbox for risk-based non-intrusive inspection of cross-border freight movements, particularly at the EU Customs Union borders. The objective of these toolboxes is to reinforce the capabilities of border security practitioners in safeguarding against a wide range of dangerous and illicit materials while minimizing disruption to the flow of goods across borders [11–14].

Both projects propose user-friendly toolboxes for customs officers, along with flexible relocatable facilities or mobile systems capable of providing high-quality information. Following container selection for inspection based on risk analysis or surveillance information, the inspection process begins with X-ray scanning of the entire cargo using large, high-energy systems. These scans generate high-resolution images that not only reveal the position in depth of the items inside the container but also classify the materials present, in terms of their density. If a suspicious area containing organic material cannot be cleared by the initial X-ray scanner, a second-line inspection system, known as tagged neutron interrogation, is employed. This technique irradiates the cargo area of interest with neutrons to provide detailed information on the chemical composition of the suspicious material, enabling the identification of explosives, illicit drugs, and various chemical elements without the need to open the container or perform time-consuming chemical tests. Additionally, the information obtained allows for the volumetric positioning of pixels of the inspected material within the container. In the current research phase of the project, container inspection using this technique typically lasts around 15 minutes, providing customs officers with a reliable and rapid response.

Furthermore, passive radiation portal monitors (RPMs) serve as a first-line inspection system for detecting nuclear radioactive materials. These systems can detect radiation quickly, often within a few seconds, without disrupting the flow of containers and while they are in motion. If there is suspicion of Special Nuclear Materials (SNM) within the containers, more advanced techniques such as photofission interrogation may be employed for further inspection. The photofission technique induces nuclear reactions in the suspicious zone using high-energy photons, enabling the detection of unique signatures of the fission produced and facilitating the identification and quantification of nuclear materials, even if the materials are shielded. Currently, methods involving active interrogation, which rely on the detection of high-energy gamma rays or neutrons, are recognized as the effective way for identifying SNM [10].

Therefore, the ENTRANCE and MULTISCAN 3D projects represent significant advancements in border security measures, offering innovative solutions to mitigate illicit trafficking and enhance inspection processes. By developing user-friendly toolboxes and implementing state-of-the-art technologies such as advanced X-ray scanning, tagged neutron interrogation, photofission systems, and passive detection systems, these initiatives aim to revolutionize the way border controls operate. With a focus on efficiency, accuracy, and reliability, seeking to minimize disruption to the flow of goods across borders while strengthening the ability of customs officers to detect and prevent the illicit transportation of dangerous materials, including nuclear substances. Contributing significantly to enhancing global security and contributing to the safeguarding of international trade and commerce, which are fundamental for the functioning of the global economy and worldwide development.

1.1 Background

Before the existence of the ENTRANCE and MULTISCAN 3D projects, both EU-funded initiatives aiming to revolutionize cargo security and inspection processes, a series of groundbreaking research projects were initiated to address the multifaceted challenges encountered in border controls over the past two decades. These challenges derive from the inefficiency in identifying dangerous and illicit materials using conventional non-intrusive inspection methods such as radiation portal monitors (RPM) and X-ray scanners, where discriminating between illicit and benign substances remains a persistent challenge, especially when materials overlap in the cargo [15].

Pioneering research efforts to address these challenges and enhance cargo security through innovative inspection technologies were undertaken within the European Union. Between 2004 and 2008, the EURITRACK project, funded under the European Union's Framework Program (FP6), focused on developing a neutron inspection system to detect threat materials (explosives, illicit drugs, etc.) in cargo containers. This project centered on developing a container inspection system based on a Tagged Neutron Inspection System (TNIS). Neutrons produced by a generator were tagged and scattered by materials inside the container, and the resulting gamma rays were used to determine the chemical composition. Field tests in the port of Rijeka, Croatia, yielded successful results, demonstrating the feasibility of the system with the complementary use of X-ray equipment [15, 16].

On the other hand, for monitoring sources of ionizing radiation inside cargo containers, the SLIMPORT project, financed by the Italian Ministry for Economic Development (MISE), aimed to develop an integrated toolbox for a complete security system to monitor harbor activities from 2009 to 2012. Within this project, the SMANDRA mobile inspection station was created to conduct non-destructive analysis alongside existing monitoring devices such as radiation portal monitors and x-ray scanners. The aim was to detect and identify sources of ionizing radiation or illegal materials within suspect volumes identified by conventional scanners. The SMANDRA system consisted of a passive unit with gamma-ray and neutron detectors and an active unit with a portable sealed neutron generator. It could function both as a standalone radiometer for detecting radiation and as part of an active interrogation system using tagged neutrons. Laboratory tests have shown promising results for detecting special nuclear materials (SNM), particularly plutonium, with passive interrogation. However, uranium detection, due to its low neutron yield and shielding capabilities, required active interrogation with tagged neutrons. In this process, neutrons were directed at the material, and the gamma-ray and neutron yields were measured in coincidence, providing the signature of the uranium. While the SMANDRA system was not specifically designed for SNM detection, its results could help the development of future portable systems tailored for this purpose, particularly for detecting masked samples [17].

Subsequently, the MODES SNM project, conducted from 2012 to 2014 and co-funded by the EU Commission under the FP7-Cooperation program, focused on technical research to develop a prototype for a mobile, modular detection system for radioactive and Special Nuclear Materials (SNM). The project aimed to deliver a tested prototype of a modular mobile system capable of passively detecting weak or shielded radioactive sources with higher accuracy than currently available systems. To maximize detection capability for SNM, the project developed new detectors for fast and thermal neutrons, as well as gamma-rays, based on high-pressure scintillation cells using noble gases. The prototype underwent laboratory commissioning at the NCBJ (National Center for Nuclear Research), followed by installation in a van for on-field demonstrations, demonstrating satisfactory performance in identifying different radioisotopes [18]. However, the challenge of identifying uranium remained, particularly in cases where the material is well-shielded.

Simultaneously, since 2009, as part of the French trans-governmental R&D program addressing CBRN-E threats (Chemical, biological, radiological, and nuclear substances, and explosives), the CEA (French Alternative Energies and Atomic Energy Commission) has been investigating the detection of SNM using neutron interrogation with the Associated Particle Technique (APT), in efforts to combat illegal trafficking of SNM at borders. The CEA developed a non-destructive method based on high-energy photon interrogation of containers, followed by the detection of particles emitted after fission. This method, originally used in nuclear waste management, relies on the identification of delayed neutrons and gamma rays emitted by fission products and has been adapted for border container control. To demonstrate the effectiveness of the technique, they conducted various studies, simulations, and experimental tests, showing promising results in identifying SNM even when the material is well-shielded and located inside a container [19–21].

Following this, from 2015 to 2018, the C-BORD project aimed to construct a comprehensive platform emphasizing the collaboration and integration of the multiple mentioned non-intrusive inspection technologies, including radiation portal monitors, X-ray scanners, tagged neutron inspection, photofission, and trace gas analyzers. The project, which took place under the European Union's Horizon 2020 program, pursued a holistic approach to maximize detection capabilities while ensuring operational efficiency and minimizing the need for physical inspections, especially for dense containerized cargo.

To achieve C-BORD's goal, its included technologies underwent rigorous testing in real-world operational conditions in collaboration with customs partners. Field trials were conducted at three customs sites: Rotterdam, The Netherlands, for testing equipment in a fully automated seaport setting; Gdansk, Poland, for implementing a rapidly relocatable checkpoint for ports; and Roszke, Hungary, for deploying mobile equipment at a land border checkpoint. These trials allowed for the assessment of enhanced technologies and demonstrated how their combined use enables the reliable detection of various illicit materials concealed within cargo containers, including radioactive substances, explosives, chemicals, drugs, and tobacco. As a result, C-BORD helped customs services figure out the best ways to use and deploy these technologies to meet their specific needs [15, 22].

1.2 Motivation

As the C-BORD project demonstrated remarkable success between 2015 and 2018 under the European Union's Horizon 2020 program, a subsequent project called ENTRANCE was initiated to build upon these achievements. The ENTRANCE project, also funded under the European Union's Horizon 2020 program, aims to develop and test a non-intrusive inspection system for cross-border cargo containers. The three-year project, launched in 2020, involves the same technologists from the C-BORD project. However, its focus is on enhancing the existing platform's capabilities by integrating artificial intelligence for material recognition and decision-making. This aims to help end-users efficiently conduct risk-based inspections of freight crossing borders while minimizing disruptions to business operations [11, 14].

Additionally, another groundbreaking initiative, the MULTISCAN 3D project, funded also under the European Union's Horizon 2020 program, and focuses on Laser-plasma-based source 3D Tomography for inspecting cargo. Launched on September 1st, 2021, with a duration of 42 months. The MULTISCAN 3D project aims to create an innovative static radiation generation method to address customs challenges effectively. By integrating advanced laser-plasma technologies, including laser-based plasma radiation production techniques, the project seeks to develop a user-friendly, flexible, and relocatable all-in-one inspection system capable of providing high-quality information through a combination of advanced techniques, such as high-energy X-ray tomography, neutron interrogation/photofission for elemental identification, and narrow gamma-ray beams based on NRF (Nuclear Resonance Fluorescence) for detecting light nuclei materials. This comprehensive approach aims to revolutionize cargo inspection, contributing to increased security and efficiency at border crossings [12, 13].

The primary motivation of this work is to make substantial contributions to both the ENTRANCE and MULTISCAN 3D projects through comprehensive testing, simulation, and refinement of the techniques used in these initiatives. Recognizing the critical need to advance and enhance these projects, which represent major improvements in border security measures, the contributions include a variety of activities. These activities involve participating in experimental tests and field trials, setting up and removing an inspection technique for field test, conducting simulations to optimize configurations and calculate dose rate maps, proposing improvements to existing techniques, and testing new detectors for potential use. Additionally, proof-of-concept tests are conducted to explore alternative neutron source reactions, aiming to boost the capabilities and efficiency of both projects.

Chapter 2

EU-funded projects

This chapter provides a comprehensive overview of the ENTRANCE and MULTISCAN 3D projects, both EU-funded initiatives aimed at enhancing border security measures with innovative technologies while ensuring smooth freight crossing without disruption. The chapter details the objectives of the projects, methodologies applied, explanation of the techniques involved, conducted tests, and their significance in border security measures. These projects are pivotal in the development of this work, which focuses on testing, improving, and simulating some of the techniques included in these two initiatives.

2.1 ENTRANCE

The EU-funded ENTRANCE (for EfficieNT Risk-bAsed iNspection of freight Crossing bordErs without disrupting business) project, aims to develop and test a non-intrusive inspection system for cross-border cargo containers, primarily at the EU Customs Union borders. The objective of this system is to empower border security professionals, providing them with enhanced capabilities to detect and prevent a broad spectrum of hazardous and illicit materials, all while minimizing disruptions in the flow of goods across borders. The 3 years project was launched on the 1st of October 2020 and it was co-funded by the EU Commission under the Horizon 2020 Research and Innovation program, with a budget of EUR 7 million. The project involves 18 partners from 9 European countries, including research institutes, universities, small and medium-sized enterprises (SMEs), and public bodies.

ENTRANCE aims to create an improved toolbox for checking cargo at borders. This toolbox uses advanced technologies to better detect various threats and illegal items without causing delays to cargo movement. The key to this improvement is a platform called ENARTIS, which automates risk assessment and information sharing. It works with both First-line NII technologies, providing real-time data on potential risks without slowing down cargo processing, and Second-line NII technologies, which come into play when a more detailed inspection is needed to find dangerous or illegal items. The goal is to enhance efficiency and security in cross-border cargo inspection [11, 14].

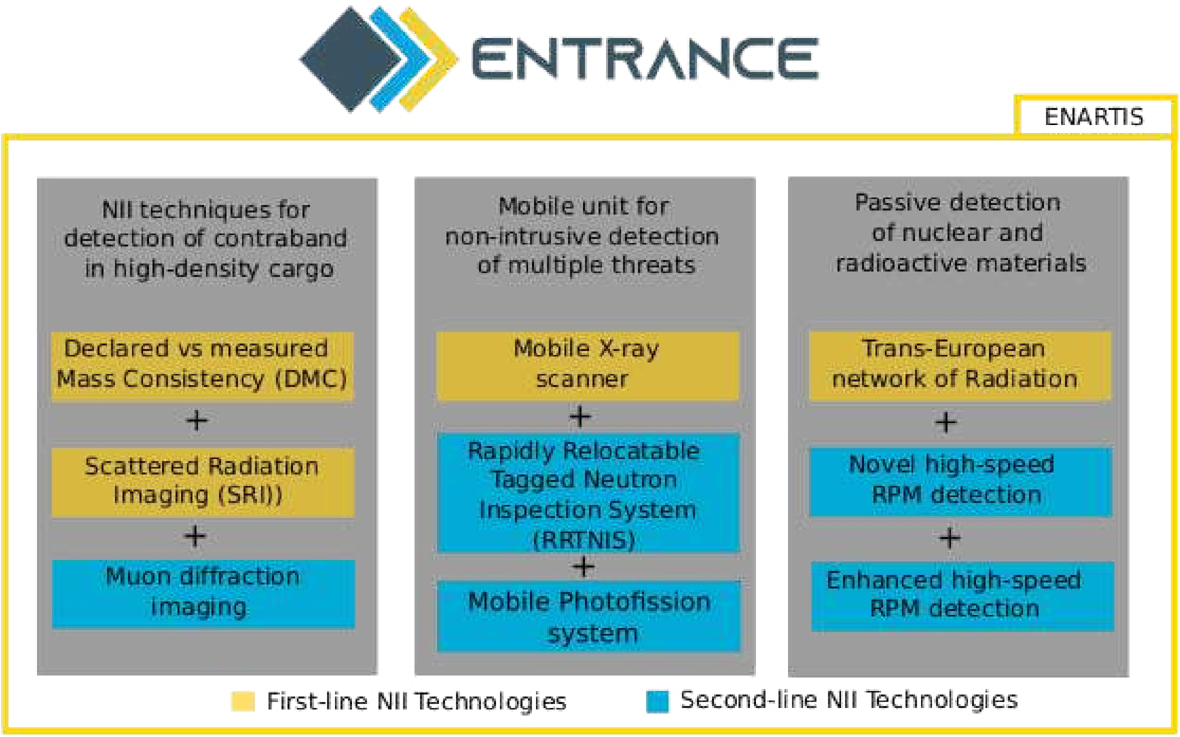

Figure 2.1: Scheme of the ENTRANCE components

The ENTRANCE project consists of three main components (as illustrated in Figure 2.1) designed to function as system nodes, ensuring compatibility with a wide range of applications. Each component operates collaboratively with the ENARTIS platform and is equipped with both First-line and Second-line Non-Intrusive Inspection NII technologies [11, 14].

- **NII techniques for detection of contraband in high-density cargo.**

  Integrating three innovative Non-Intrusive Inspection (NII) techniques to identify and offer image details on the shape, size, and location of contraband within the high-density cargo. The two First-line methods are employed for the systematic scanning of incoming open railway cargo while the train is in motion. If a more detailed inspection is needed, a Second-line technique is utilized to provide additional information. The three techniques are as follows:

  - Declared vs measured Mass Consistency (DMMC): this method consists in inspecting ore-filled, open railcars. This non-intrusive method consists of finding an anomaly between an estimation of railcar content's weight and what has been declared at customs. DMMC provides invaluable insights in identifying and intercepting shipments that may contain contraband, including drugs, weapons, and explosives.

  - Scattered Radiation Imaging (SRI): It's a promising tool for finding hidden objects or illegal items. SRI uses scattered gamma rays to create images inside an object, and it's especially good at looking through dense materials. This makes it a great choice for inspecting cargo containers with tightly packed items.
  - Muon diffraction imaging: This technique involves reconstructing muon trajectories after they pass through an object to create a density map known as muography. It's a safe method that does not expose customs officers or merchandise to radiation. This technology is especially effective at discovering hidden objects, such as contraband, especially in train cars filled with dense materials like steel balls.

- **Mobile unit for non-intrusive detection of multiple threats.**

  The relocatable unit is specifically designed for non-intrusive detection, equipped with advanced identification and discrimination capabilities. It effectively identifies a diverse range of threats, encompassing explosives, illicit drugs, chemical warfare agents, and radioactive materials such as enriched uranium and plutonium. The unit integrates one First-line technique and two Second-line techniques.

  The operational process, outlined in Figure 2.2, involves scanning incoming vehicles/containers with a mobile X-ray scanner (First-line NII) while they are still in motion, ensuring minimal disruption to the flow. If ENARTIS detects the presence of threats, illicit declarations, or suspicious zones containing organic materials or materials with high atomic numbers (Z), it issues a warning and provides detailed information about the nature, form, size, and location of the suspicious zone.

  In cases where the suspicious zone contains organic materials, the RRTNIS (Second-line NII) is deployed to identify the type of threat or clear the cargo. Alternatively, if the suspicious zone contains materials with high atomic numbers, the mobile photo-fission system (Second-line NII) is employed to identify the type, whether it be nuclear or radioactive material or SMN (Special Nuclear Material).

  - Mobile X-ray scanner: advanced X-ray functionalities, with a 7 MeV mobile container X-ray scanner, providing detailed image information on the positioning of a given threat inside the container. This advanced technology ensures good image resolution, depth information, and material discrimination. It also helps separate overlapping objects more clearly, making it easier to identify each object individually and avoid confusion caused by them being stacked on top of each other. In contrast to traditional backscatter X-rays, this innovative approach employs transmission X-rays, offering increased penetration to visualize organic threat materials, even when concealed by metal.

  - Rapidly Relocatable Tagged Neutron Inspection System: in cases where a suspicious zone containing organic material cannot be cleared by the First-line X-ray scanner, the RRTNIS system comes into play to provide detailed information on its chemical composition, enabling precise threat identification. The TNIS (Tagged Neutron Inspection System) utilizes inelastic neutron scattering technology combined with associated particle time-of-flight spectroscopy, creating a highly effective and accurate system for threat detection and identification. This neutron inspection is capable of identifying explosives, illicit drugs, and various chemical elements that could be utilized in chemical warfare, including sulfur, phosphorus, fluorine, sodium, and others. It plays an important role in dealing with both security issues and illegal activities.
  - Mobile Photofission system: the photofission system serves as a secondary technology for detecting SNM, such as uranium and plutonium isotopes. When a suspicious zone involving an SNM risk is identified by the X-ray scanner or by the Radiation Portal Monitors (RPM), the photofission system is implemented to confirm or clear this risk. The measurements are conducted using the same mobile unit as the X-ray system. The procedure involves irradiating the potential risk with high-energy photons. Due to the physical properties of the material, photofission is induced in the presence of SNM. The main signatures of this reaction: prompt neutrons, delayed neutrons, and high-energy delayed gamma rays are measured in order to identify the presence of SNM.

- **Passive detection of nuclear and radioactive materials.**

  Creation and validation of the first trans-European Radiation Portal Monitors (RPM) Network, integrating different types and technologies of RPM from different suppliers into a single common supervision system for passive detection of nuclear and radioactive material with minimal disturbance of flow. Key components:

  - Trans-European network of Radiation: Common software interface for Border Control Point Radiation Portal Monitors (BCP RPMs) with standardized data exchange format allowing for the integration of different types of RPM into the network.
  - Radiation Portal Monitors (RPMs): These monitors integrate diverse detection technologies to passively identify illicit nuclear and radioactive (NR) materials, equipped with both gamma-ray and neutron detectors. Key techniques include:
    - Novel high-speed RPM detection technology: This innovation minimizes flow disruption during passive detection of NR. A groundbreaking Rapid Radiation Portal Monitor (RPM) system, featuring three detectors in line, achieved detection at speeds of up to 30 km/h for radioactive sources.

∗ Mobile Radiation Detection System: This rapidly relocatable system, transportable in two cases and operable by a single operator, detects both neutron and gamma radiation. It functions as a versatile solution, serving as a 1st level control in container compounds where an RPM is impractical, or as a 2nd level control providing spectroscopic information after an RPM gamma alarm. During tests, the system was installed in a static van and scanned containers moving at speeds of 5-10 km/h, containing various radionuclides [11, 14].

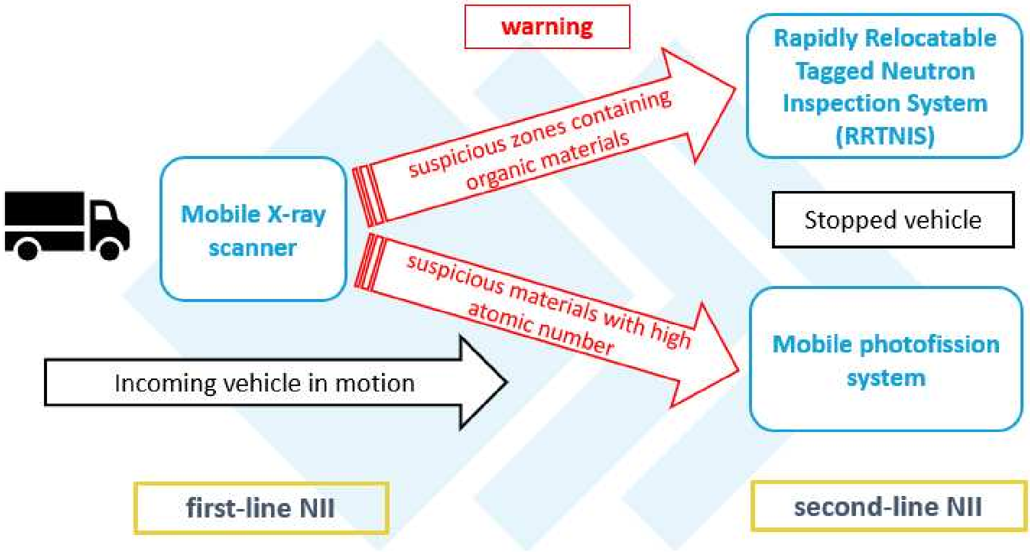

Figure 2.2: Ilustratrives procedure of the Mobile unit for non-intrusive detection of multiple threats. Figure taken from [11]

The efficacy of the ENTRANCE toolbox was assessed through three field trials, each led by practitioners at strategic locations within the EU Customs Union borders. These trials were meticulously selected based on their relevance, strategic significance, and feasibility.

1. **May 2023:** The most extensive trial took place in Rijeka, Croatia, for three weeks. This trial assessed seven technologies (RX-scanner, RPM (3 techniques), Photofission, RRTNIS, ENARTIS platform), with testing conducted on both mock-up and commercial containers. Some pictures of the ENTRANCE techniques during the field test can be seen in Figure 2.3.

2. **July 2023 and October 2023:** DMMC and Muon technology (and SRI) were tested at Vitry, France, specifically at SMITHD facilities. Measurements were conducted on trucks loaded with boxes concealed in sand.

3. **End of October 2023:** Mobile RPM from Arktis underwent testing at CERN facilities.

Mobile X-ray scanner

Mobile Photofission system

RRTNIS

Rapid Radiation Portal Monitor (RPMs)

Figure 2.3: Pictures of some of the ENTRANCE techniques during the field test in Rijeka, Croatia.

2.2 MULTISCAN 3D

The MULTISCAN 3D project, funded by the European Union, focuses on a Laser-plasma-based source 3D Tomography for inspecting cargo. The primary goal of the project is to create an innovative static radiation generation method that can effectively address customs challenges. The project was launched on the 1st of September 2021, with a duration of 42 months, and is co-funded by the EU Commission through the Horizon 2020 research and innovation program, with a budget of EUR 7 million. It is carried out by a consortium comprising 18 partners from 9 different countries [13].

X-ray screening methods used in border and customs inspections for the past two decades have become inadequate in detecting diverse and evolving trafficking materials. The limitations of radiography in border controls have prompted customs authorities to seek additional technologies for conducting comprehensive container inspections. Therefore, in an effort to move beyond traditional 2D scanning approaches, the EU-funded MULTISCAN 3D project aims to explore the potential of high-energy X-rays for conducting volumetric inspections of large cargo. The objective is to develop a 3D high-energy X-ray tomograph that is compatible with rapid customs procedures. Nevertheless, the most difficult challenge of the project lies in achieving precise 3D imaging using innovative laser-based plasma radiation production techniques. In addition, the project aims to explore the capability of laser-plasma technologies in generating various types of radiation, including neutrons and gamma-rays, as illustrated in Figure 2.4, in order to perform a complete inspection of the container, in this way a chemical identification of goods can be achieved [12]. The idea is to create an all-in-one inspection system that is user-friendly, flexible, and relocatable, providing high-quality information through the following techniques:

- Fast high-energy 3D X-ray tomography (as the first line) for detailed imaging with low emitted dose. It is applied to identify anomalies in the inspected object or its contents, including sizes and volumes.
- Neutron interrogation/photofission is employed as a secondary technique for elemental identification (e.g., explosives, illicit drugs, and chemical components) and for detecting Special Nuclear Materials (SNM), including uranium and plutonium isotopes.
- Narrow gamma-ray beam based on NRF (Nuclear Resonance Fluorescence) as an additional second-line technique, which enables the detection of light nuclei material including carbon, oxygen, fluorine, etc.

Designs, simulations, lab validations, and real-environment demonstrations will be conducted during the whole period of the project. In particular, in the first year, the MULTISCAN project focused on designing the system, clarifying use cases, and defining requirements with customs partners. Simulations were conducted on laser production, 3D tomographic reconstruction, and detector technologies. The second year involved confirming X-ray feasibility, optimizing configurations, and progressing in design aspects through regular meetings. Technical developments, including measurement campaigns and validation at XXL-CT, were carried out. The third phase will focus on laboratory validation and addressing remaining challenges, with experimental tests and field tests planned for Rotterdam in 2025.

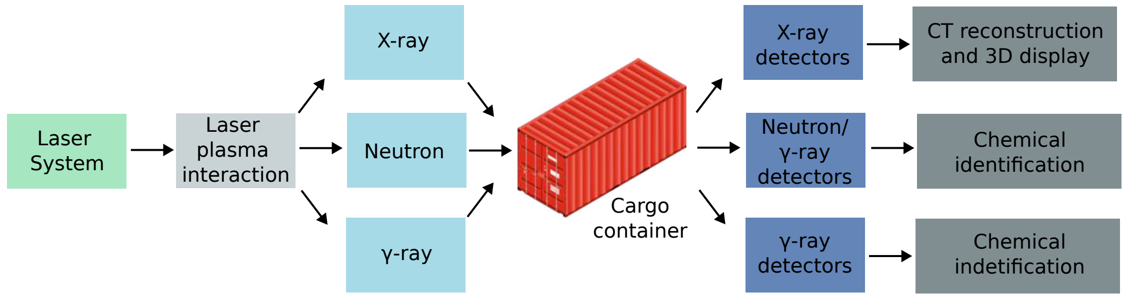

Figure 2.4: System diagram of the MULTISCAN project

Chapter 3

Theoretical Framework

In this chapter, some fundamental physics concepts, applied methodologies, and detailed explanations of interrogation techniques are presented to facilitate the comprehension and understanding of this research. The discussion begins with a description of the interaction of gamma-rays and neutrons with matter, including their detection mechanisms. Adding also information about how organic scintillators can detect and discriminate between gamma rays and neutrons. Subsequently, the physical principles underlying neutron interrogation and photofission techniques are exposed. Additionally, the operation of laser-plasma accelerators is provided, along with proposed reactions for generating the neutron source required for the interrogation technique, but with the use of laser-driven accelerator-based. Finally, it is explained how simulations are performed to cover different aspects of this research.

3.1 Interaction of uncharged radiation with matter

The interaction of uncharged particles with matter differs from that of charged particles due to the absence of an electric charge. While uncharged particles do not directly interact with matter via electromagnetic forces, they can still interact through other fundamental forces such as gravity, weak nuclear force, strong nuclear force, or through indirect processes. Consequently, the detection of uncharged particles often involves indirect methods, such as detecting secondary particles or the effects of their interactions with matter [23]. In this section, the interaction mechanisms of uncharged radiation, including gamma-rays and neutrons, along with their detection methods, are explained.

3.1.1 Interaction of gamma-rays

Gamma rays, a type of electromagnetic radiation, interact with matter through various mechanisms, primarily photoelectric absorption, Compton scattering, and pair production. These interactions result in the partial or complete transfer of the gamma-ray's energy to electron energy. In contrast to charged particles, which lose energy gradually through continuous collisions with atoms, gamma rays experience abrupt and sudden changes in their trajectories [23]. Principal interaction mechanisms:

- **Photoelectric Absorption:** In this process, a gamma ray interacts with an atom, causing the photon to completely disappear. Instead, an energetic photoelectron is ejected from one of the atom's bound shells. This interaction primarily occurs with atoms having higher atomic numbers (Z) and is significant for low-energy gamma-rays.

- **Compton Scattering:** Compton scattering involves the interaction between a gamma-ray photon and a free electron in an absorbing material. The photon is deflected from its original path, transferring a portion of its energy to the electron, resulting in the creation of a recoil electron. Compton scattering is the predominant interaction mechanism for medium to high-energy gamma-rays.

- **Pair Production:** Pair production occurs when a gamma-ray photon's energy exceeds twice the rest-mass energy of an electron (1.02 MeV). In this process, the photon is annihilated, and an electron-positron pair is created. Pair production becomes more likely as the energy of the gamma-ray photon increases into the many-MeV range.

Gamma-rays detection:

Gamma-ray detection relies on the interaction between gamma-ray radiation emitted from a radioisotope and the detector material. The probability of interaction depends on the incident photon energy and the atomic number (Z) of the material. Typical detectors used for gamma-ray detection include scintillation detectors, semiconductor detectors (such as germanium detectors), and gas-filled detectors. These detectors exploit the interaction mechanisms mentioned above to detect and measure gamma-ray radiation. For instance, scintillation detectors detect the light emitted when gamma rays interact with scintillating materials, while semiconductor detectors measure the charge generated by gamma-ray interactions in a semiconductor material [23]. Understanding these interaction mechanisms is essential for designing efficient gamma-ray detection systems for various applications, including medical imaging, nuclear physics research, and homeland security.

Some gamma-ray detectors utilized in the development of this work include the EJ-309, the EJ-301, and the EJ-276G, all organic scintillators from Eljen Technology in Texas, US. The EJ-309 and the EJ-301 are liquid scintillators, while the EJ-276G is a plastic scintillator. These detectors are capable of detecting and discriminating between gamma rays and fast neutrons. They are known for their high light output and fast response time and are widely used in radiation detection applications such as gamma-ray spectroscopy, neutron detection, and general-purpose radiation monitoring across various fields including nuclear medicine, environmental monitoring, and scientific research.

Additionally, this study utilized two commonly used inorganic scintillators, NaI:Tl and $LaBr_3$:Ce, which are known for their excellent energy resolution in gamma-ray spectroscopy. The NaI:Tl detector consists of a sodium iodide crystal doped with thallium, whereas the $LaBr_3$:Ce detector is made of lanthanum bromide crystal doped with cerium. Both detectors provide good light output, energy resolution, and fast decay time. However, the $LaBr_3$:Ce detector outperforms the NaI detector in terms of light output, as well as offering significantly better energy resolution and time resolution. These detectors are employed in various fields and applications, especially where high-resolution detection and precise identification of gamma-ray energies are essential [23].

3.1.2 Interaction of neutrons

Neutrons, similar to gamma rays, lack electric charge, so they interact with matter differently compared to charged particles. Instead of interacting with atomic electrons, neutrons primarily interact with atomic nuclei, driven by the nuclear force. This interaction occurs when a neutron passes close to a nucleus, typically within a distance of about 10^{-13} cm (the radius of a nucleus), resulting in a low probability of interaction and allowing neutrons to travel long distances in matter without immediate interaction. This property makes neutrons challenging to detect using conventional methods. However, when interactions do occur, they mainly involve the nuclei of absorbing materials, leading to changes in neutron energy or trajectory.

In contrast to gamma-rays, neutron interactions often yield heavily charged particles as secondary radiations. These particles originate from neutron-induced nuclear reactions or energized nuclei of the absorbing material. Detection typically involves converting incident neutrons into secondary charged particles. The likelihood of interaction, expressed in terms of barns (cm^2), represents the probability of interaction per unit path length. It depends strictly on the type of target nuclei and varies significantly with neutron energy [23, 24], which can be categorized as shown in Table 3.1 [25].

Table 3.1: Neutron Energy Ranges and Classifications

Neutron Energy	Energy Range
0.0 – 0.025 eV	Cold (slow) neutrons
0.025 eV	Thermal neutrons (at 20°C)
0.025 – 0.4 eV	Epithermal neutrons
0.4 – 0.5 eV	Cadmium neutrons
0.5 – 10 eV	Epicadmium neutrons
10 – 300 eV	Resonance neutrons
300 eV – 1 MeV	Intermediate neutrons
1 – 20 MeV	Fast neutrons
> 20 MeV	Ultrafast neutrons

Neutron beams are generated through different nuclear reactions, and unlike charged particles, it is not possible to accelerate neutrons, but it is possible to reduce the energy of high-energy neutrons by making them collide with atoms of different materials. The primary interaction modes of neutrons with matter are the following [26]:

- **Elastic Scattering:** Neutron elastic scattering is a fundamental interaction process in which an incoming neutron collides with a target nucleus and is deflected without any change in its kinetic energy. This means that both the neutron and the nucleus remain in their ground states after the interaction. This type of scattering is common at lower neutron energies and is represented as (n,n) in nuclear reactions. Materials known as moderators, such as water, paraffin, plastic, and graphite, are used to slow down neutrons through elastic scattering. The effectiveness of a moderator depends on the atomic mass number of the target material, with lower atomic mass numbers being more efficient moderators.

- **Inelastic Scattering:** Similar to elastic scattering, inelastic scattering involves a neutron striking a nucleus. However, in this case, the nucleus is left in an excited state, retaining energy from the interaction. This endothermic process is denoted as (n, n'). The excited nucleus subsequently emits gamma rays as it decays. When it does occur, it is most likely to involve high Z nuclei and high-energy neutrons. This interaction is utilized in the Neutron Interrogation technique employed in the ENTRANCE and the MULTISCAN 3D projects.

- **Capture Reactions:** In this process neutrons may be captured by atomic nuclei, leading to the formation of heavier isotopes and the emission of gamma rays. Known as neutron capture or radiative capture, this process finds applications in neutron detection and activation analysis. This exothermic interaction is represented by (n, γ), and it signifies an absorption reaction where the original neutron is absorbed.

- **Charged-Particle Reactions:** Neutrons may also undergo absorption reactions, leading to their disappearance. These reactions, such as (n, α) and (n, p), can be either exothermic or endothermic.

- **Neutron-Producing Reactions:** Reactions like (n, 2n) and (n, 3n) occur with energetic neutrons, extracting one or two neutrons from the struck nucleus. These endothermic reactions are crucial, particularly in reactors containing heavy water or beryllium, due to the loosely bound neutrons in these materials.

- **Fission:** Neutrons possessing sufficient energy can trigger nuclear fission in certain isotopes, such as uranium-235 and plutonium-239. This reaction releases additional neutrons and a substantial amount of energy, making it pivotal for nuclear reactors and weapons.

Neutron detection

Neutron detection relies on indirect methods due to the neutral charge of neutrons. Elastic scattering and nuclear reactions are the primary mechanisms employed in neutron detectors.

- **Elastic scattering:** This method is effective for detectors containing light nuclei, such as hydrogen or helium, making it suitable for fast neutron detection. Fast neutrons interact through elastic scattering with these light nuclei, causing the recoiling nuclei to ionize gas or semiconductor materials. This ionization generates free charges, which is then collected, and produces an electrical signal proportional to the neutron's energy. On the other hand, rich-in-hydrogen scintillator materials, such as organic liquids or plastic scintillators, the energy transferred to the recoiling nuclei excites the atoms or molecules. This excitation leads to the emission of light photons, which are then detected by photomultipliers or photodiodes. The intensity of the emitted light is proportional to the energy of the recoiling nucleus. The energy spectrum for monoenergetic neutrons appears as a continuous distribution due to the range of possible recoil angles during elastic scattering.
- **Nuclear reactions:** Slow and thermal neutrons are detected through nuclear reactions in which the nuclei of the detector capture the neutrons and produce detectable gamma-rays or other charged particles. Commonly used reactions for such detection include: ^3He(n,p)^3H, ^6Li(n,t)^4He, ^{10}B(n,α)^7Li and the fission of uranium.

Detectors utilizing recoil or reaction mechanisms can employ solid, liquid, or gas-filled detection media. While the choice of reactions is limited, the variety of detecting media offers numerous options. These detectors encompass a range of types, such as plastic scintillation detectors (e.g., EJ-200), liquid scintillators (e.g., EJ-309, EJ-301, or benzene), gas-filled detectors (e.g., He-3, BF_3 or boron coated proportional counters), inorganic scintillators (e.g., lithium iodide), and activation detectors (utilizing thin foils of materials like indium or gold for neutron activation, detecting subsequent gamma-ray emissions) [27].

Neutron detection typically provides limited energy information, often indicating only the presence of neutrons, but reconstruction of neutron energy spectra may be achieved indirectly through various techniques, such as using multiple absorber samples, measuring the Time of Flight (ToF) of neutrons [23, 24], analyzing the proton recoil spectrum and the detector's response function (e.g., pulse height spectra for different monoenergetic neutrons within the energy range of interest), or by applying unfolding methods, where the neutron energy spectrum is determined from the pulse height spectrum of the recoil proton.

3.2 Pulse shape discrimination in organic scintillators

As explained previously in Subsection 3.1.1, some of the detectors utilized in this work include the EJ-309, EJ-301, and EJ-276G, all of which are organic scintillators capable of detecting and discriminating between gamma rays and fast neutrons. This discrimination is achieved through Pulse Shape Discrimination (PSD), which leverages the different decay times of the scintillation light components. Organic scintillators emit most of their light from a prompt fluorescence process with a decay time of a few nanoseconds, while the remaining light comes from delayed fluorescence with a longer decay time of several hundred nanoseconds. The relative contributions of these light components depend on the nature of the exciting particles. By analyzing these differences, it is possible to distinguish between neutrons, gamma rays, heavy charged particles, and other types of radiation. This technique is known as Pulse Shape Discrimination (PSD). [23].

Fast neutrons are detected using organic scintillators through elastic collisions with the hydrogen nuclei, which result in the emission of protons that ionize the material. In contrast, photons are detected by electrons generated via the Compton effect. As a result, gamma-ray detection produces less intense delayed fluorescence compared to fast neutron detection. Consequently, gamma rays register faster pulses, while fast neutrons register slower pulses.

To differentiate between the types of events recorded, the double gate integration method is employed to perform pulse shape discrimination. This method involves calculating the pulse shape parameter (PSD), defined as:

$$\mathrm{PSD} = \frac{Q_{\text{long}} - Q_{\text{short}}}{Q_{\text{long}}} = \frac{Q_{\text{tail}}}{Q_{\text{total}}}$$

where Q_{short} is the integral over a short time window, including the fast rise time region and part of the fastest decay component of the pulse, and Q_{long} is the integral over a long gate, encompassing the majority of the pulse. In a 2D-PSD plot, which is a 2D histogram of the PSD values against Q_{long}, it is possible to differentiate between the two types of particles, as shown in Figure 3.1.

To evaluate the performance of a detector in discriminating between two types of particles, the Figure of Merit (FoM) parameter is calculated. This involves creating a 1D histogram of the PSD values, where two mean peaks corresponding to neutron and gamma-ray events are observed. The FoM is defined as:

$$\mathrm{FoM} = \frac{\Delta}{\delta_n + \delta_\gamma}$$

where Δ is the difference between the mean values of the neutron and gamma-ray distributions, and $\delta_n + \delta_\gamma$ is the sum of the Full Width at Half Maximum (FWHM) of the gamma-ray and neutron peaks [28]. All the events inside the red zone in the 2D-PSD plot of Figure 3.1 were plotted in a PSD plot, resulting in a FoM value of 1.427.

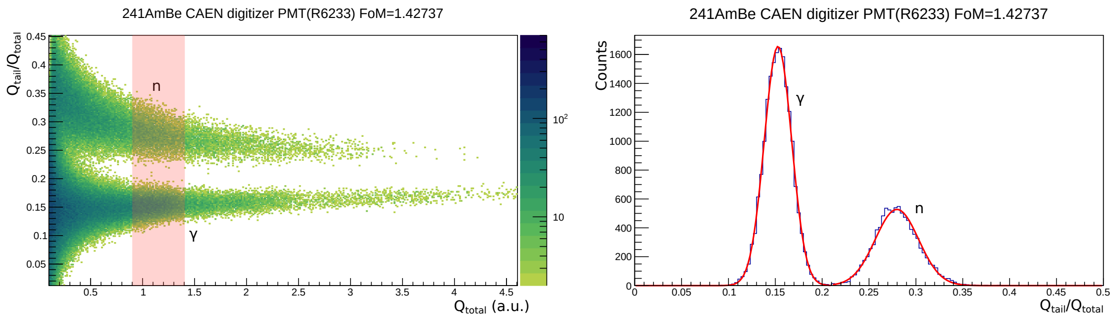

Figure 3.1: 2D-PSD and PSD plots corresponding to a measurement using a ^{241}AmBe source with a EJ-276 3"x5" organic detector. Figures taken from: [28]

3.3 Interrogation techniques for the inspection of freight containers

This section provides a detailed explanation of two interrogation techniques utilized in the ENTRANCE and the MULTISCAN 3D projects. These techniques are among the most studied and researched in the current work.

3.3.1 Neutron Interrogation technique

The ENTRANCE and MULTISCAN 3D projects utilize the Rapidly Relocatable Tagged Neutron Inspection System (RRTNIS) as a secondary method when organic materials in suspicious zones of containers cannot be identified by the primary X-ray scanner. This system provides detailed information on the chemical composition of the materials, aiding in precise threat identification, such as explosives, narcotics, and illicit contraband, which may have similar appearances on X-ray radiography, because of their similar densities and atomic numbers.

The RRTNIS employs the Associated Particle Technique (APT), which combines inelastic neutron scattering with associated particle Time-of-Flight (TOF) spectroscopy. In this technique, fast neutrons interact with the nuclei in the inspected zone through inelastic scattering, causing the nuclei to emit gamma rays. These gamma rays are then detected and identified through gamma spectroscopy using inorganic scintillators. The energy of these gamma-rays serves as a "footprint" for the type of nuclei irradiated, allowing for the identification of elemental materials present. Additionally, the system can determine compound ratios between carbon, nitrogen, and oxygen, aiding in organic threat identification or benign material classification. In Figure 3.2, the inelastic neutron scattering cross-section of some of the isotopes of interest is shown as a function of the incident neutron energy. It is evident that the probability of interaction with metal materials is typically at least one order of magnitude higher compared to organic materials, as seen with lead, iron, and copper. However, this does not interfere with the measurement of organic materials. The photopeaks detected for each isotope have distinct energy levels, enabling clear differentiation through gamma spectroscopy.

Additionally, the use of a high neutron flux results in high statistical quality of the gamma-ray spectra.

Specifically, in the ENTRANCE project, mono-energetic fast neutrons of 14 MeV (in agreement with what is shown in Figure 3.2) are generated using a tagged neutron beam produced through the fusion reaction $^{2}\mathrm{H}+^{3}\mathrm{H}\longrightarrow \mathrm{n}+\alpha$. This is achieved with a neutron generator manufactured by SODERN [29], which has a maximum operational rate of 10^{8} n/s. However, the nominal rate is 5×10^{7} n/s, and in this work, it was used at a rate of 2×10^{7} n/s, with deuterium accelerated to 70 keV. Due to the nearly simultaneous emission of the alpha particle and neutron, a position-sensitive YAP:Ce inorganic scintillator integrated into the neutron generator tube enables precise targeting of the neutrons within the inspected area. This scintillator serves as the starting point, and the stopping point occurs when a gamma ray is detected. These gamma rays are detected by twenty parallelepiped-shaped NaI:Tl detectors, each measuring 12.7x25.4x12.7 cm^{3}, and with an energy resolution between 6% and 8.5% at 662 keV. By combining information regarding the direction of the neutron and its traveled distance, equivalent to the time elapsed between the neutron's creation and the gamma-ray detection, the gamma spectrum of any elementary volume (voxel) in the container can be reconstructed. Subsequently, the spectrum is unfolded into a linear combination of elementary gamma spectra (database). This process allows the determination of the component concentration of each element [30–32].

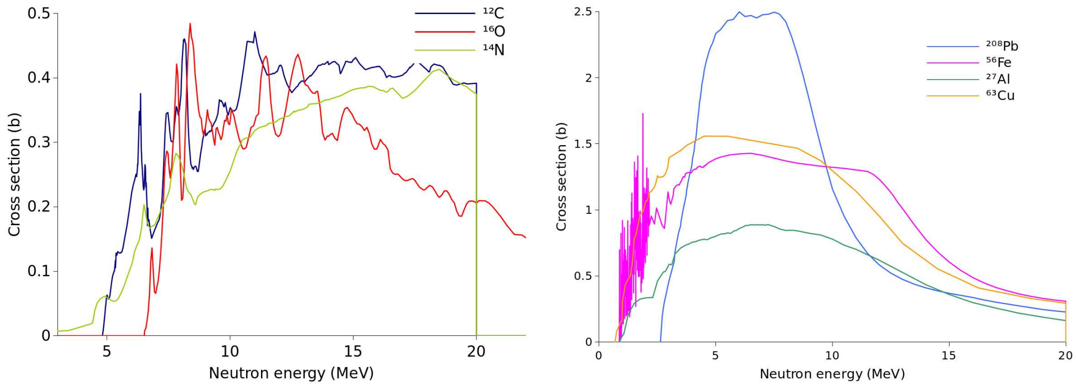

Figure 3.2: Inelastic neutron scattering cross section of ^{12}C, ^{16}O, ^{14}N, ^{208}Pb, ^{56}Fe, ^{27}Al and ^{63}Cu nuclei in function of the incident neutron energy. Data taken from: [33]

The database comprises elementary gamma spectra, which are neutron-induced signatures measured during the RRTNIS calibration phase using pure element targets. Examples include graphite for carbon, liquid nitrogen for nitrogen, and water for oxygen (as fast neutrons do not produce gamma rays in hydrogen). Pure metals such as iron, lead, copper, aluminum, and zinc were also utilized.

In Figure 3.3, gamma spectra from neutron inelastic scattering of pure elements are presented. The figure includes both experimental results and those obtained from Monte Carlo simulations, as taken from [34]. Notable peaks characterizing these elements include the 4.4 MeV peak for carbon, 6.13 MeV for oxygen, 5.1 MeV for nitrogen, 0.84 MeV for iron, and 2.6 MeV for lead. Compounds were used when pure element materials were not readily available, such as chlorine, fluorine, phosphorus, and potassium. Consequently, having the gamma spectrum of each element present in an elementary volume (voxel) enables the retrieval of weights for each measured element, providing information on the target's composition.

To ensure safety from radiation, the neutron generator is enclosed by a polyethylene shield. The shield has an aperture cone of 35° through which the neutrons are focused into the inspected zone. A layout of the entire setup can be seen in Figure 3.4. An iron frame holds the twenty NaI:Tl detectors and a lead shield that reduces the count rate associated with gamma rays produced in the polyethylene shield. These gamma rays are produced due to neutron capture on hydrogen nuclei or inelastic scattering on carbon nuclei [30].

The geometry details of the experimental setup can be found in Subsections 4.2.1 and 5.2. However, for the MULTISCAN project, the specifications of the RRTNIS setup have yet to be determined. The project is currently in earlier stages compared to the ENTRANCE project, which first aims to demonstrate the production of neutrons, X-rays, and gamma-rays through laser-driven accelerators.

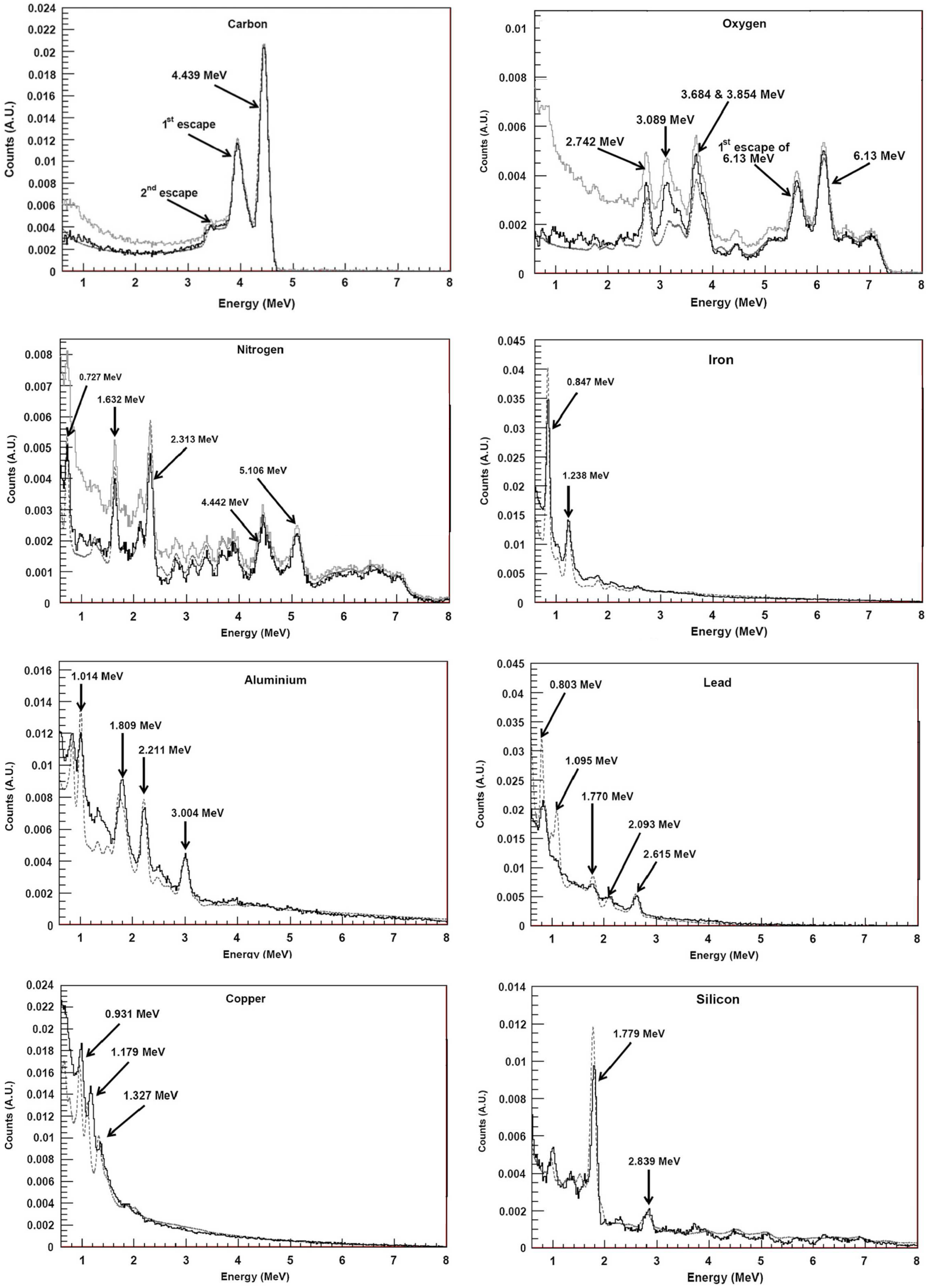

Figure 3.3: Gross experimental spectrum of the different materials (carbon, oxygen, nitrogen, iron, aluminum, lead, copper and silicon) under interrogation (grey line), net spectrum after subtraction of the background (black line), and calculated gamma-ray spectrum using Monte Carlo simulations (dotted line). Plots taken from [34].

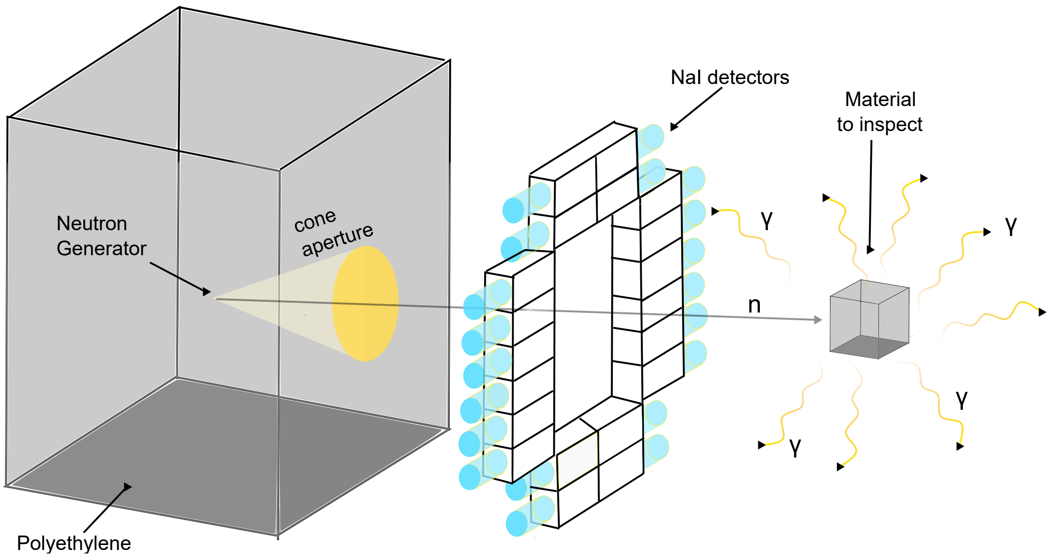

Figure 3.4: Layout of the ENTRANCE TNIS

3.3.2 Photofission technique

Nuclear fission occurs when a heavy nucleus passes through a high deformation state where there is a competition between the surface tension and the Coulomb repulsion, which leads to the split of the nucleus into two fragments. This phenomenon occurs when the nucleus enters a high deformation state, transitioning from its ground state to a saddle point where Coulomb repulsion surpasses surface tension, facilitating larger deformation. Subsequently, at the scission point, the nucleus separates into two fragments known as fission fragments. Fission can be either spontaneous or induced, with induced fission triggered by various means such as gamma-ray excitation or neutron capture [24].

During fission, excess neutrons, including prompt and delayed neutrons, are emitted. Prompt neutrons are released instantly, while delayed neutrons follow shortly after, typically within seconds. The number of prompt neutrons emitted varies depending on the nature of the fragments and incident particle energy [24]. The reaction in which the fission of an atomic nucleus is induced by a high-energy photon is known as photofission, and the most adapted measurement technique to check the presence of SNM is called Active Photon Interrogation (API) and is based on the photofission reaction on actinides, i.e., uranium and plutonium isotopes.

Special Nuclear Material (SNM), comprising uranium and plutonium isotopes, poses significant security concerns, potentially being exploited for nuclear weapons. To mitigate the risk of illicit trafficking of SNM in Europe, effective inspection methods are essential. While X-ray scanning is commonly used for container inspection, its efficacy in detecting SNM signatures is limited. Therefore, a second-line technology based on photofission reactions offers a promising non-destructive detection method.

The ENTRANCE and MULTISCAN 3D make use of photon interrogation systems leveraging linear electron accelerators, as a second-line technology. These systems irradiate suspect cargo container areas with high-energy photons, inducing photofission reactions on actinides, where two fission products are produced in each fission reaction. Initially, prompt fission particles are emitted, corresponding to the release of two to three prompt neutrons and approximately eight prompt gamma rays; these radiations are emitted within 10^{-15}s seconds from the moment of fission. Typically, these fission products are generated in unstable states with excess neutrons, leading them to emit an additional six to seven gamma rays and approximately 0.01 to 0.02 neutrons per fission as they transition to stable states [35], which corresponds to delayed particles. The detection of these delayed gamma-rays and neutrons forms the basis for identifying the presence of SNM, providing a well-established, reliable, and unique signature for the detection, identification, and quantification of nuclear materials. Currently, active interrogation techniques based on the measurement of high-energy gamma-rays or neutrons are considered the most effective approach to identify SNM [10].

One should also note that this method enables deep interrogation in the container thanks to the penetration capabilities of the high-energy photon beam. Both fissile and fertile actinides can undergo photofission, with an energy threshold of around 6 MeV for all actinides, a technical challenge taking into account that specifically in the ENTRANCE project the feasibility of the API method is performed using a 7 MeV mobile X-ray scanner [36, 37]. Notably, at 7 MeV, the cross-section of the photofission reaction for isotopes such as ^{233}U, ^{235}U, ^{238}U, and ^{232}Th is around 20 mb [38].

In the ENTRANCE project, the detection of these delayed particles is achieved through the utilization of two independent photofission portals. Each portal is equipped with a 1-meter-long EJ-200 plastic scintillator for gamma-ray detection, and a neutron detection block comprising five Helium-3 filled tube gas proportional counters (pictures of the portals can be seen in Figure 3.5). These tubes, measuring 1 meter in length and 1.2 cm in radius, are embedded within high-density polyethylene and encased by a cadmium layer. The cadmium serves as an absorber for thermal neutrons, safeguarding the Helium-3 detector from sources other than the fission of Special Nuclear Material (SNM). Moreover, polyethylene is employed to thermalize the fast neutrons emitted before they reach the Helium-3 detector, thereby enhancing its sensitivity [37].

The neutron detection on the proportional counters occurs when a neutron is captured by a Helium-3 nucleus, it releases approximately 764 keV of kinetic energy, which is absorbed by the gas, ionizing it and creating ion pairs. Under the effect of high voltage, electrons are collected on the anode, while positive ions are collected on a cathode and then the resulting signal is transmitted to the electronics rack via coaxial cables. Conversely, the EJ-200 plastic scintillator serves for the detection of gamma-rays. When photons interact with the plastic material, scintillation occurs, emitting light that is collected by photomultipliers.

This work aims to replace the two existing independent photofission portals with two innovative detection systems. The first system is the ZnS/LiBO/PDMS thermal neutron detector, which offers a novel, flexible, and highly effective solution for thermal neutron detection. The second system is a compact gamma-ray detection unit, featuring an organic scintillator coupled with a SiPM array. Details of this study are developed and presented in Chapter 7.

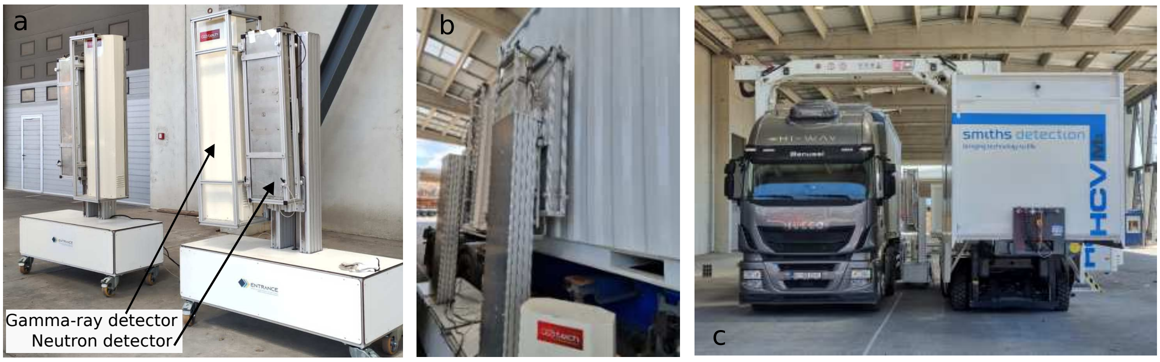

Figure 3.5: Pictures of the photofission portals of the ENTRANCE project a), and photofission experimental setup deployed at the Škrljevo terminal, Rijeka, Croatia (May 2023) b) and c).

3.4 Laser-plasma accelerator

The MULTISCAN 3D project explores the potential of laser-plasma accelerators (LPAs) in creating an all-in-one first- and second-line inspection system for containers, using X-rays and neutrons. Plasma-based accelerators, driven by lasers offer high accelerating electric fields, about a thousand times greater than traditional accelerators, enabling compact structures. LPAs have the advantage of achieving higher accelerating gradients compared to radiofrequency accelerators, making them more compact and cost-effective [39]. The innovative laser-based plasma radiation technology in the project involves using high peak power laser pulses focused in a gas jet, creating a plasma wave with electric fields of up to hundreds of GeV/m. This technology accelerates electrons to relativistic energies in short distances, producing electron bunches that interact with a high-Z target to generate X-rays through the Bremsstrahlung mechanism [12], X-rays essential for the 3D X-ray tomography required for the container inspection.

In parallel, the project explores the photofission technique, considering the use of a high-energy photon source produced through a laser-driven Inverse Compton Scattering beam. This innovative approach involves allowing electrons with relativistic energies to undergo Inverse Compton Scattering with photons backscattered in a reflective material. The resulting photons, after increasing their energy through the ICS interaction [40], are redirected into the initial beam direction. Simultaneously, magnetic fields deviate the electron bunches outside the beam direction. The tunability of photon energy is achieved by adjusting the distance between the target and the point where the ICS interaction occurs.

Conversely, in the neutron interrogation technique within the MULTISCAN 3D project, the laser-plasma accelerator induces nuclear reactions that generate neutrons. The detailed procedure for this neutron generation is explained in the subsequent Subsection 3.4.1.

3.4.1 Laser-driven neutron sources

By leveraging the advantages of laser-driven accelerators, which enable the acceleration of particles to high energies over short distances while maintaining compact and cost-effective equipment, it becomes possible to innovate and transform current container inspection procedures at border checkpoints. Laser-driven neutron sources can play a crucial role in this transformation. These sources accelerate high-energy particles over short distances, inducing reactions that result in the emission of neutrons. They are distinguished by their ability to generate neutron beams with high brilliance, directionality, and tunable energy spectra, making them ideal for neutron interrogation techniques. Additionally, the pulsed nature of the beam allows for ultra-short burst durations, facilitating Time-of-Flight (ToF) measurements, which are essential for neutron interrogation techniques.

In the MULTISCAN 3D project, the proposed mechanism for generating high neutron fluxes involves nuclear fusion reactions, specifically through a method known as beam-target fusion. This approach entails deploying high-energy ions, such as deuterons, in a pitcher-catcher scenario. The first target, known as the "pitcher", is irradiated by the laser, acting as the source of projectile light ions. Fusion reactions are triggered in the second target, referred to as the "catcher," initiated by the projectile ions from the first target [41].

Currently, most neutron production using ultraintense lasers is achieved through either the acceleration of light ion species (such as hydrogen isotopes) or the generation of gamma-rays to induce nuclear reactions. Most laser-based neutron sources rely on nuclear reactions involving protons and deuterium, including d(d,n)^{3}He, ^{7}Li(d,n)^{8}Be, ^{7}Li(p,n)^{7}Be, etc [42].

In this context, this work explores a proof of concept experiment to assess the feasibility of neutron interrogation techniques, utilizing material such as beryllium-9 (^9Be) as the second target, where the following reaction takes place: ^{9}Be(d,n)^{10}B. Currently, the mono-energetic fast neutron beam of 14 MeV used in the ENTRANCE project originates from the fusion reaction ^{2}H+^{3}H$\longrightarrow$n+α. This DT reaction with high flux can be achieved with low-energy acceleration; in this case, only 70 keV is used for the acceleration of deuterium (see Figure 3.7). However, given the capability of laser-based accelerators to reach high energies with compact devices, an interesting task is to obtain neutrons from the reaction ^{9}Be(d,n)^{10}B, which offers the advantage of producing a continuous neutron spectrum rather than a mono-energetic beam. This continuous neutron spectrum allows for the excitation of interrogated materials with various neutron energies, thereby accessing diverse excitation states of carbon, nitrogen, or oxygen, and consequently detecting gamma rays with varying energies. Moreover, choosing these reaction eliminates the need to handle tritium, a radioactive isotope that requires stringent safety protocols to manage radiation exposure risks. The total neutron yield for the fusion reactions in terms of the incident particle energy can be seen in Figure 3.7.

The ^{9}Be(d,n)^{10}B reaction is an exothermic reaction with a Q value of +4.361 MeV [43], at low accelerating energies it produces generally monoenergetic neutrons at 4 MeV and a high-energy it produces a high neutron energy spectrum in all emission angles, as shown in Figure 3.6. However, the cross-section for the reaction increases less strongly with energy than for the DT reaction, and accelerating energies up to 1 MeV are needed to approach comparable neutron yields, as seen in Figure 3.7.

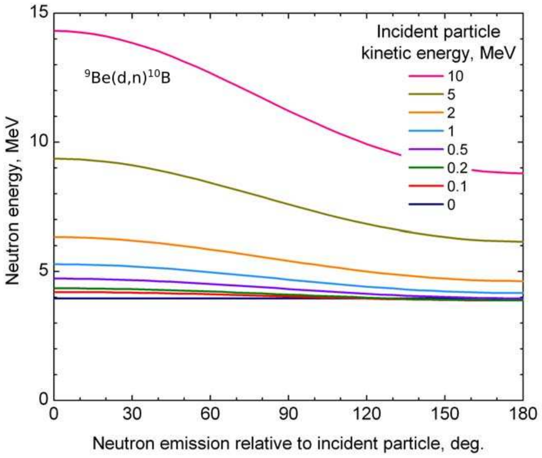

Figure 3.6: Theoretical energy of neutrons from the ^{9}Be(d,n)^{10}B fusion reaction at different emission angles for varying incident particle kinetic energies. Plot taken from: [43]

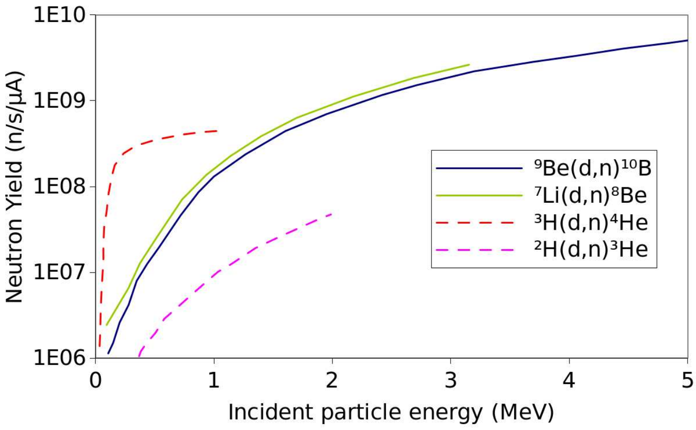

Figure 3.7: Total neutron yield curves for some fusion reactions in function of the incident particle energy. Data taken from: [43]

3.5 Simulation using the Monte Carlo method

The Monte Carlo Method is a computational algorithm designed to tackle problems characterized by probability distributions, utilizing repeated random samplings. It involves a large number of iterations before yielding a predicted outcome. Widely applied across various domains such as finance, engineering, supply chain, and science, it proves particularly beneficial for systems with numerous degrees of freedom.

Presently, the Monte Carlo method stands as the premier approach for simulating radiation transport through matter. This technique simulates the trajectory of particles through random steps, interrupted by interactions with the material, resulting in changes in direction, energy loss, and the generation of secondary particles. The probability of these interaction mechanisms is determined by cross-sections, necessitating a comprehensive description of all relevant physical processes and particle types involved. For instance, in the case of photons with energies spanning keV to MeV, primary interaction mechanisms include the photoelectric effect, Compton scattering, and pair production.

The Monte Carlo method readily lends itself to the simulation of systems with intricate geometries and diverse material compositions, enabling the creation of simulations that closely mimic real-world experimental setups. Typically, assembling a radiation configuration involves defining the radiation source, irradiated samples, and detection systems, and specifying the processes involved [44].

Numerous simulation codes are dedicated to modeling radiation transport, among which GEANT4, PENELOPE, MCNPX, EGS4, and FLUKA are prominent. These codes employ stochastic models based on probability density functions to sequentially model individual events of random variables, tracking all interactions each particle undergoes, from inception to termination.

3.5.1 Geant4

In this work, it was employed the GEANT4 code (version 10.7) to conduct various simulations essential for the development of the ENTRANCE and MULTISCAN projects. GEANT4, implemented in C++, is a renowned tool designed to simulate the transport of radiation through matter. It encompasses all aspects of simulation, including the system's geometry, involved materials, fundamental particles, primary particle generation, particle tracking through materials and external electromagnetic fields, physics processes, detector response, event data generation, and event and track storage. Additionally, it provides visualization capabilities for the detector and particle trajectories. The physical and theoretical models within GEANT4 are based on experimental data [45].

For the development of this work, simulations served multiple purposes, such as optimizing setup geometry, studying occurring interactions, estimating possible spectra or results, understanding background radiation, and predicting neutron spectra generated from specific reactions (as discussed in Subsection 3.4.1), calculating dose maps for safety and restricted zones for some of the interrogation techniques of the projects, and for comparing experimental and simulated results.

Several classes within GEANT4 are utilized for constructing the simulations:

- The logic and physical volumes are defined in the G4VUserDetectorConstruction class, where parameters such as density, position, composition, sizes, and shapes of the volumes comprising the physical setup are specified.
- The G4VUserPrimaryGeneratorAction class defines the incident beam or source characteristics in terms of energy, events, and shape.
- Particle and interaction mechanisms are defined in the G4UserPhysicsList class, where different libraries can be employed depending on the particle interactions of interest. For instance, G4EmLivermorePhysics is implemented for photon simulation, while G4HadronPhysicsQGSP_BIC_HP is used for neutron simulation.
- Additional classes are employed to extract important information. For example, the G4UserSteppingAction class records event information at each step, while the G4UserTrackingAction class tracks particles at specific moments and stores the relevant information. These two classes enable access to the deposited energy of each particle in the detector using step→GetTotalEnergyDeposit(), also the Time of Flight (ToF) spectra can be reconstructed using the GetGlobalTime class (step→GetPreStepPoint()→GetGlobalTime()).
- Using the G4UserSteppingAction class, any event interacting with the designated scoring volume (such as the detector volume) can be monitored. By requesting the track ID and parent ID, all secondary particles generated by primary particles can be captured effectively. Consequently, the energy deposited by each secondary particle can be calculated, and the cumulative sum of these energies corresponds to the energy deposited by the primary particle.
- Subsequently, with the implementation of the G4UserEventAction and G4UserRunAction classes, energy or time spectra can be reconstructed.

Chapter 4

Simulation of the RRTNIS system in the ENTRANCE project

This chapter presents a simulation study of the Rapidly Relocatable Tagged Neutron Inspection System (RRTNIS) within the ENTRANCE project. Simulation performed using the Monte Carlo method with the Geant4 v10.7 toolkit, the experimental setup's geometry is replicated in the simulation. This setup includes a polyethylene box housing a neutron beam and large-size NaI:Tl detectors mounted on an iron frame with lead shielding. The simulations were conducted to analyze factors such as optimization of setup geometry, time of flight determination, energy deposition, and back-scattered neutron effects. Results showed qualitative agreement of the ToF spectrum with experimental data, and optimization of the setup geometry confirms the effectiveness of the already defined experimental configuration.

4.1 Motivation

The simulation study detailed in this chapter is a crucial step for the optimization and experimental validation of the RRTNIS within the ENTRANCE project. This study was performed using the Monte Carlo method with the Geant4 v10.7 toolkit. Notably, it represents the first simulation conducted with the most realistic geometry of the TNIS setup. Unlike previous simulations, such as those in [15], this work includes all components, such as the detectors, polyethylene box, detector frame, and floor, all with realistic dimensions. This comprehensive modeling allows for an accurate simulation of the system's performance, enabling the analysis of various parameters of the TNIS in a realistic scenario.

A key focus of this simulation is the determination of the Time of Flight (ToF) spectra, which provides a deeper understanding of the contributions from each object in the inspection area. This understanding is essential for optimizing the setup's geometry to minimize background noise and maximize detection efficiency. By simulating different configurations and analyzing their impacts, the design and operational capabilities of the RRTNIS can be optimized. Moreover, a comparison of the simulated data with the experimental data helps to confirm the accuracy and reliability of the experimental setup and results.

Additionally, this simulation study enhances our understanding of various interactions within the experimental setup. For instance, it provides insights into the interactions between neutrons and different materials, identifies all potential gamma-ray emissions from each element under inspection, and offers strategies to mitigate the effects of back-scattered neutrons that can interfere with measurements.

4.2 Simulation Methodology and Results

4.2.1 Geometry of the Experimental Setup in the Simulation

Following the configuration of the RRTNIS system in the ENTRANCE project, the geometry of the experimental setup was precisely replicated in the simulation. For a deeper insight into the operation and geometry of the RRTNIS, please see Subsection 2.1 and Subsection 3.3.1. The simulation was performed using the Monte Carlo method with the Geant4 toolkit v10.7 and with specific classes detailed in Subsection 3.5.1.

In each simulation, $3x10^7$ neutrons were generated, where each event comes from an isotropic neutron beam with an energy of 14 MeV centered inside a polyethylene box measuring 130x154x120 cm^3. The polyethylene box contained a cavity housing the neutron beam, while a cone along the x-axis focused the neutrons inside an angle of 34.94°. Positioned at 94 cm from the beam origin along the x-axis, twenty large NaI:Tl detectors (12.7x25.4x12.7 cm^3) were mounted on an iron frame (1.5 cm thick) with a 5 cm thick lead shield to absorb those gamma rays emitted due to neutron capture on hydrogen or inelastic scattering on carbon.

The target, with dimensions of 17x28x35 cm^3 was situated 150 cm from the beam origin. For testing purposes, the material type of the target was varied in each simulation, and other configurations of the geometry were explored, e.g. the distances between the polyethylene box, the detectors, and the target. Additionally, a concrete floor (100 cm thickness) was placed under the setup, with a separation of 132 cm between the floor and the beam in the y-direction. Figure 4.1 provides different views of the setup in the simulation. For a clearer understanding of the geometry setup, refer to the schematic view in Figure 4.2.

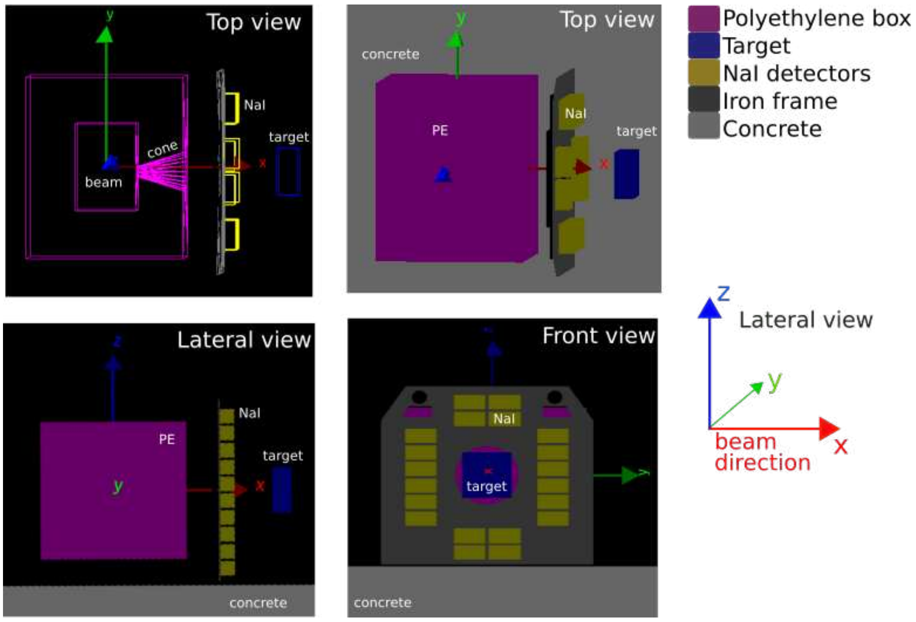

Figure 4.1: Pictures of the RRTNIS setup in the simulation, viewed from the top, front, and side perspectives

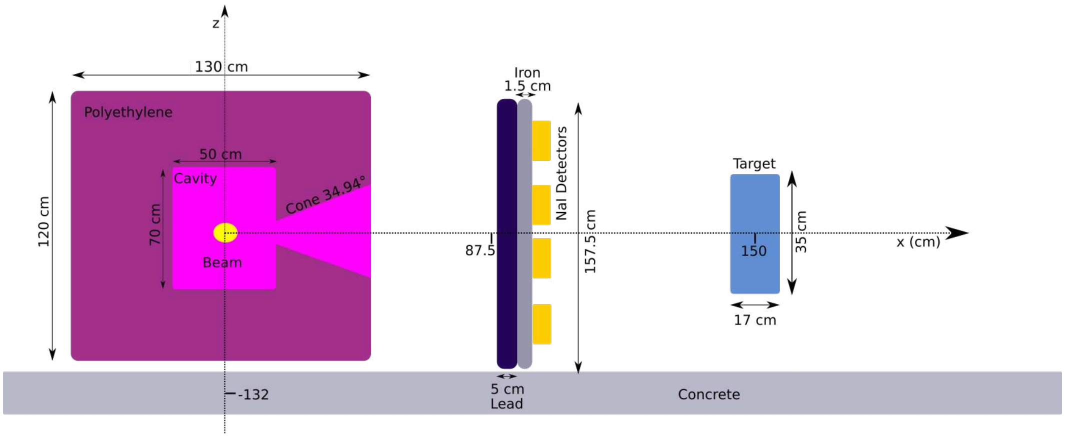

Figure 4.2: Schematic view of the RRTNIS experimental setup, seen from the side perspective.

4.2.2 Time of Flight determination in the simulation

An important parameter considered in the simulation was the Time of Flight (ToF) of the gamma-rays reaching the detectors. Taking into account that with the determination of the ToF of the detected events, it is possible to localize the position of the object of interest inside the container. This time encompasses the moment when the fast neutrons are created, their interaction through inelastic scattering with the volume under inspection, and concludes when a gamma ray reaches one of the detectors.

In the simulation, the ToF of gamma-rays reaching the detectors was determined using the GetGlobalTime class (step→ GetPreStepPoint()→ GetGlobalTime()). This time spans from the initialization of the neutron to the gamma-ray's interaction with the detector. Since all gamma rays reaching the detectors are tracked from their creation, their origin volume can be determined using the action aTrack→ GetOriginTouchable()→ GetVolume()→ GetLogicalVolume(). Consequently, the ToF can be plotted as a function of the gamma-ray's origin volume, illustrating the correlated background, with a direct correlation between ToF and volume distance, as can be seen in Figure 4.3, where it displays the ToF spectrum of gamma-rays reaching the detectors for various material targets, including carbon, iron, lead, liquid nitrogen, water, and a cocaine simulant ($C_{17}H_{22}ClNO_4$), with a selection based on their origin volume. Simulations were conducted with $3\text{x}10^7$ events, 14 MeV neutrons, and a ToF window of 80 ns.

It is essential to recognize that the background comprises two distinct components: a random component and a correlated component. In experimental scenarios, the random background is estimated by analyzing the average number of counts at a specific energy level for non-physical (negative) distances, as illustrated in Figure 5.9. Conversely, the correlated background results from tagged neutron interactions with the surrounding materials. To address this, experimental measurements taken without the target are used to subtract these correlated events, ensuring that only those originating from the target of interest are included. As shown in Figure 4.3, when dealing with metal targets, the correlated background has minimal impact on the measurements of events associated with the target.

Gamma rays originating from the target exhibit a Time of Flight (ToF) of approximately 30 ns (as seen in Figure 4.3), corresponding to the time for neutrons to reach the target. This is calculated since the velocity of a 14 MeV neutron is 5 cm/ns, and the travel distance is 150 cm, which corresponds to the distance between the target and the origin of the neutrons: $t = \frac{d}{v} = \frac{150[cm]}{5[cm/ns]} = 30[ns]$. The gamma-ray flight time between the target and the detector is negligible due to the speed of light, which is approximately 30 cm/ns. Given a distance of around 60 cm, the flight time is approximately 2 ns.

The remaining events, which correspond to gamma rays generated in the polyethylene box and on the detector frames, have a time of flight (ToF) that precisely matches the time it takes for neutrons to interact with these objects. The events highlighted in pink represent gamma rays originating from the target, and their occurrence is influenced by the inelastic neutron scattering cross-section of the various nuclei present in the target. As illustrated in Figure 3.2, the number of gamma-rays emitted from metal materials is greater due to their higher cross-section compared to organic materials, often by at least one order of magnitude. Additionally, the density of the material affects the quantity of these events.

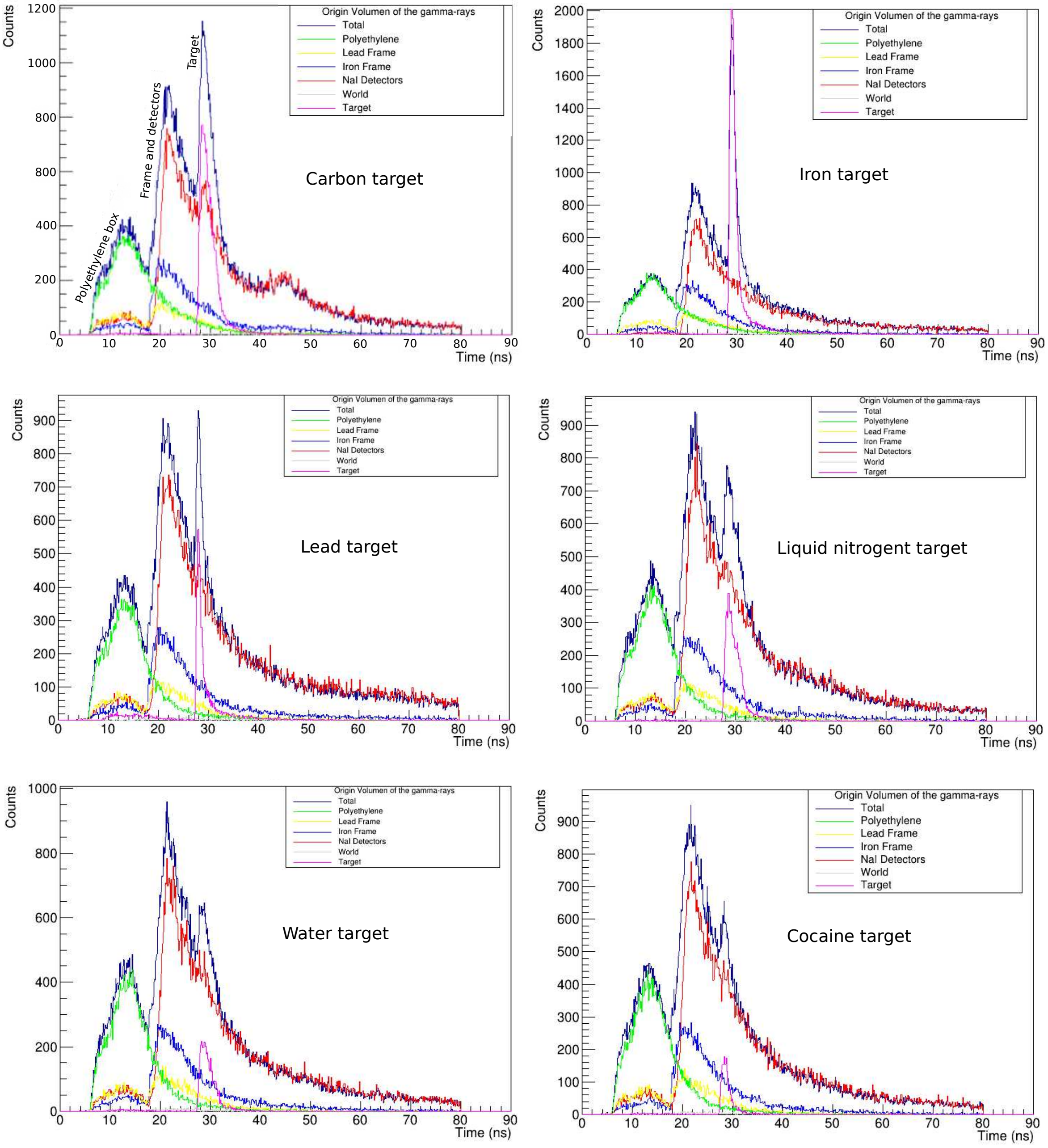

Figure 4.3: ToF spectra of the gamma-rays that reach the detectors, with a selection based on their origin volume. Simulation performed with 3x10^7 events, with neutrons of 14 MeV and a ToF window of 80 ns, for different target compositions (carbon, iron, lead, liquid nitrogen, water, and, a simulant of cocaine)

It is important to note that in experimental scenarios, the finite time resolution of the acquisition system is primarily determined by the detectors and their photomultiplier tubes (PMTs), which in conjunction introduce a time Full Width at Half Maximum (FWHM) of several nanoseconds. This finite resolution causes peaks and variations in the ToF spectra to appear less sharp (see Figure 5.9 on the right for an example).

Figure 4.4 shows the number of gamma-rays as a function of their volume of origin, using the carbon target and the whole ToF spectrum. It is notorious that the polyethylene, the iron frame, and the detectors, make a big contribution to the correlated background. For the same simulation, in Figure 4.5 it can be seen how many gamma rays arrive at each detector, in the same figure it is shown a scheme. As expected, detectors 5 and 6 receive fewer counts, meanwhile detectors 1 and 2 which are in the same position but in the lower part of the frame, receive more counts than 5 and 6, due to the proximity with the concrete floor.

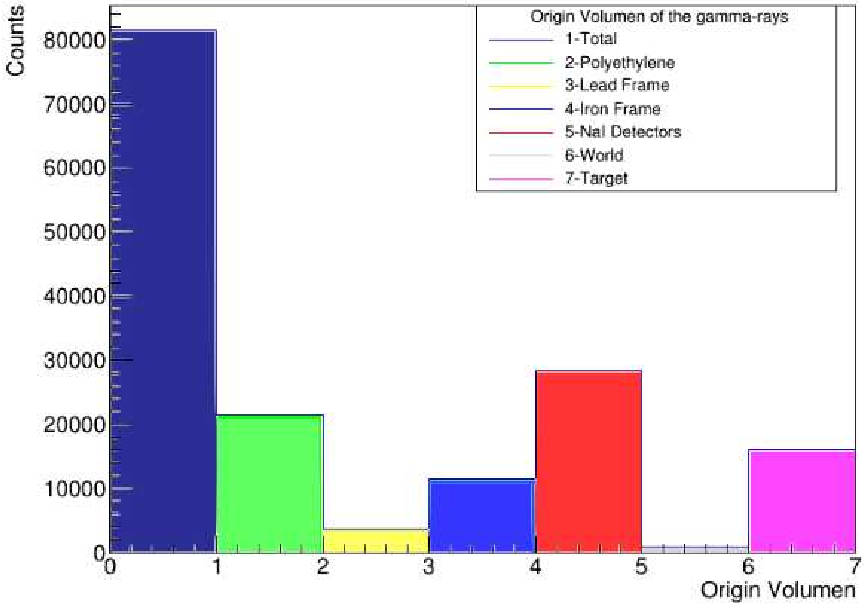

Figure 4.4: Histogram illustrating the count of gamma-rays reaching the detectors based on their origin volume, utilizing the carbon target. The simulation was conducted with 3x10^7 events, employing neutrons of 14 MeV and a carbon target.

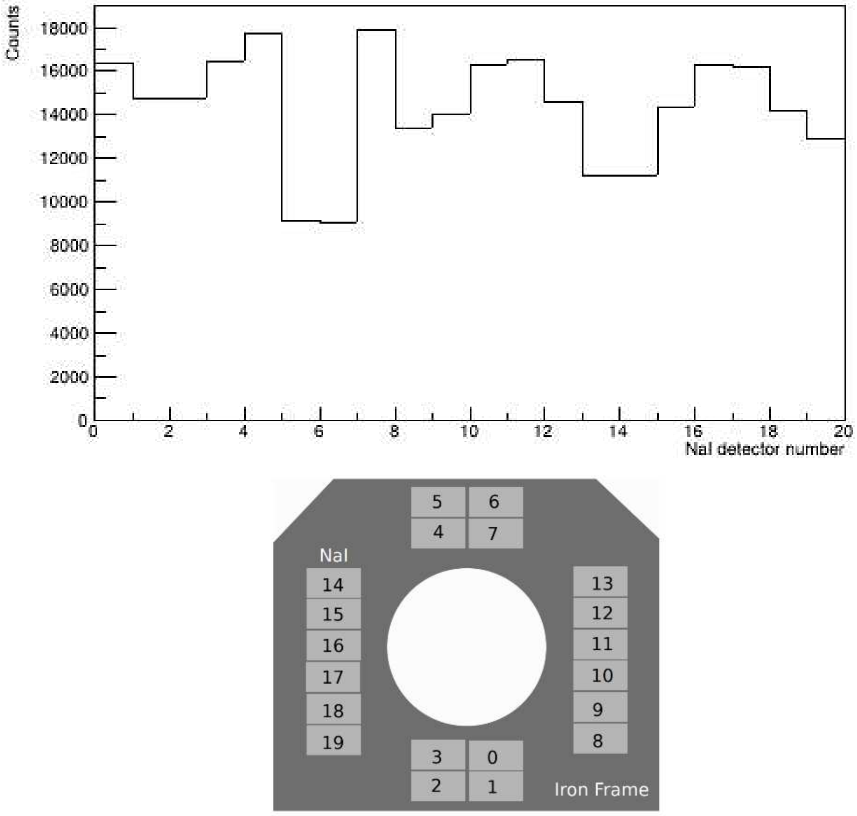

Figure 4.5: Histogram displaying the count of gamma-rays detected in each detector (left figure). Schematic representation of the NaI detector array, with each detector labeled (right figure). The simulation was conducted with $3\text{x}10^7$ events, employing neutrons of 14 MeV and a carbon target.

4.2.3 Investigation of Back-Scattered Neutrons

In the simulation of the carbon target (refer to Figure 4.3), a distinct peak is observed between 40 and 60 ns, indicating the origin of gamma rays within the detector volumes. This observation raises the suspicion of back-scattered neutrons exciting the nuclei of the detectors. Additionally, by tracking the particles in the simulation, this phenomenon was further confirmed, revealing instances of back-scattering of neutrons with the target. To explore this phenomenon, a study of back-scattered neutrons was conducted.

It is important to note that the back-scattering cross-section for 14 MeV fast neutrons on a carbon target (approximately 5 mb/sr) is at least an order of magnitude higher compared to that of an iron target [46].

The study involved conducting a simulation in which a sensitive volume with a half-sphere geometry was placed between the detectors and the target, as shown in Figure 4.6. This volume was configured to detect neutrons that were back-scattered from the target, traveled to the detectors, and interacted with the detector through inelastic scattering. The resulting energy spectra for those neutrons that crossed the half-sphere are presented in Figure 4.7, where a higher rate of back-scattered neutrons is observed for the carbon target. The two peaks observed for each target correspond to the resultant energy of the neutrons when they undergo inelastic scattering with the nuclei of ^{12}C and ^{56}Fe, respectively. The energy peaks observed depend on the excited state of the nucleus (whether it is an iron or carbon nucleus) after the inelastic interaction occurs.

Notably, the intensities of the peaks decrease as the energy decreases for carbon, but this trend is not observed for iron. This difference can be explained by specific nuclear transitions that are more likely to occur at certain energies, as well as the probability of neutron interactions with the detector, which varies with the energy of the bask-scattered neutron.

For instance, in the case of iron, the peak corresponding to the lower excited state has an interaction cross-section of approximately 70 mb, which is one order of magnitude higher than that of the higher excited state ($\sim$ 1 mb). This explains why the neutron peak at higher energy is more intense. On the other hand, for carbon, the lower excited state has an interaction cross-section of approximately 200 mb, while the higher excited state has a cross-section of about 19 mb, again showing one order of magnitude difference. However, in this case, the neutron peak at lower energy is more intense. This could be attributed to the fact that those neutrons with a lower energy of around 7 MeV are more likely to interact with the detectors (data on interaction cross-sections is taken from [33]). Additionally, there is a peak near 14 MeV for both targets, corresponding to elastic scattering interactions between the neutrons and the targets.

The findings of this investigation regarding back-scattered neutrons are essential for understanding the time-of-flight (ToF) spectra obtained in experimental situations when a carbon target is used.

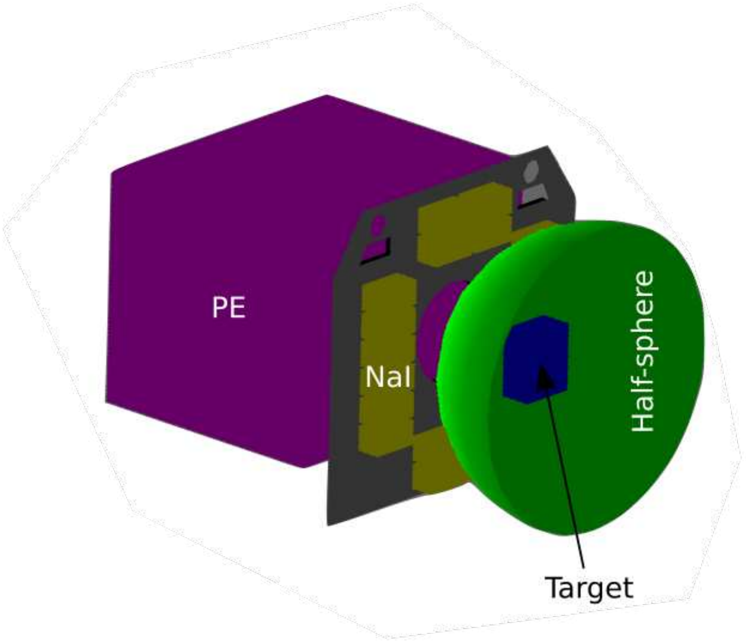

Figure 4.6: Picture of the RRTNIS setup in the simulation, featuring the half-sphere positioned between the target and the detectors for the back-scattering study.

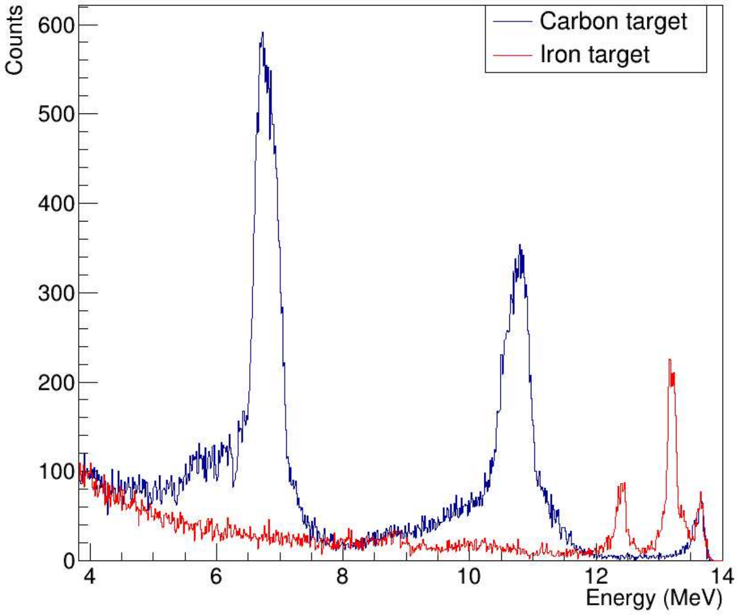

Figure 4.7: Energy spectrum of the neutrons back-scattered on the target, for two types of target material (carbon and iron).

4.2.4 Determination of the energy deposition

In the simulation, the energy deposition of each gamma-ray in the detector is obtained by tracking the particle and all the secondary particles that the gamma ray can create inside the detector. This tracking is possible thanks to the GMSteppingAction class, where any gamma ray that touches the scoring volume, which is the detector's volume, is tracked. The track ID and the parent ID are requested since these footprints permit to capture of all the secondary particles created by the primary particle (initial gamma ray). Then, it is possible to determine the energy deposited for each secondary particle (step→GetTotalEnergyDeposit()), and the sum of all of them gives us the total energy deposited by the primary gamma-ray.

Figure 4.9 illustrates the total energy spectra obtained in the simulations using different material targets: carbon, iron, lead, liquid nitrogen, water, and a simulant of cocaine ($C_{17}H_{22}ClNO_4$), for the events with a Time of Flight (ToF) between 0 and 80 ns. In the plots, the energy spectra of gamma-rays originating from the target are depicted, corresponding to the de-excitation of nuclei within the target following inelastic scattering induced by fast neutrons. It is important to note that in the simulated spectra is not taken into account the energy resolution of the detectors, in comparison with experimental spectra as seen in Figure 5.10. Typically, in experimental scenarios, the reference gamma peaks used for element identification are the 4.43 MeV for ^{12}C, 0.847 MeV for ^{56}Fe, 2.6 MeV for ^{208}Pb, 5.106 MeV for ^{14}N, and 6.13 MeV for ^{16}O.

When there is no restriction on the ToF in the energy spectrum, more energy peaks are observed (see Figure 4.8). These energy peaks represent all possible reactions that can occur, including the excitation of polyethylene, detectors, the iron frame, and the carbon target. However, all these gamma rays counted have a time of flight (ToF) greater than 80 ns, which is not of interest. Therefore, when the ToF is restricted to the range of 0 to 80 ns, some energy peaks that are not relevant disappear.

Additionally, it is important to note that in our model, we do not account for the random background. In experimental scenarios, a significant contribution to this random background comes from gamma rays with an energy of 2.23 MeV. These gamma rays are emitted during the de-excitation of hydrogen contained in polyethylene when neutrons are thermalized inside the PE box, followed by thermal neutron capture on the hydrogen nuclei.

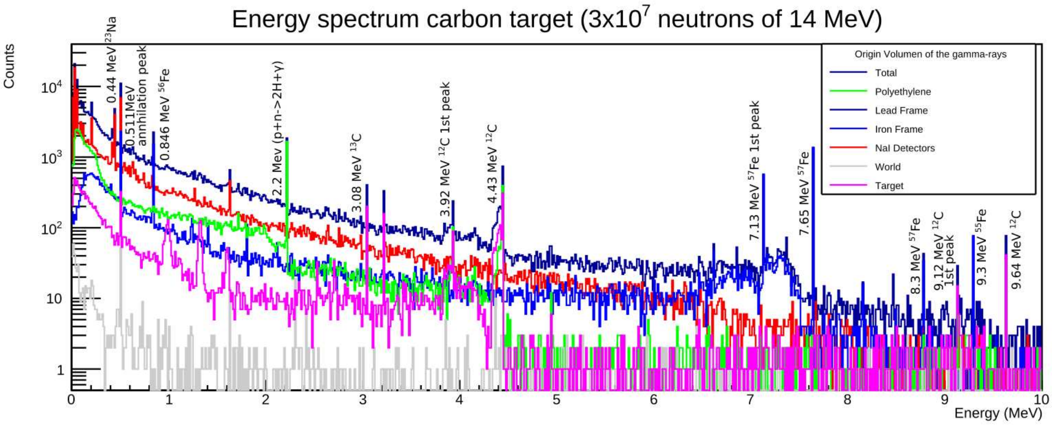

Figure 4.8: Simulated gamma-ray energy spectrum using a carbon target, in function of origin volume. Simulation conducted with 3x10^7 events, using neutrons with an energy of 14 MeV, without Time of Flight (ToF) restriction.

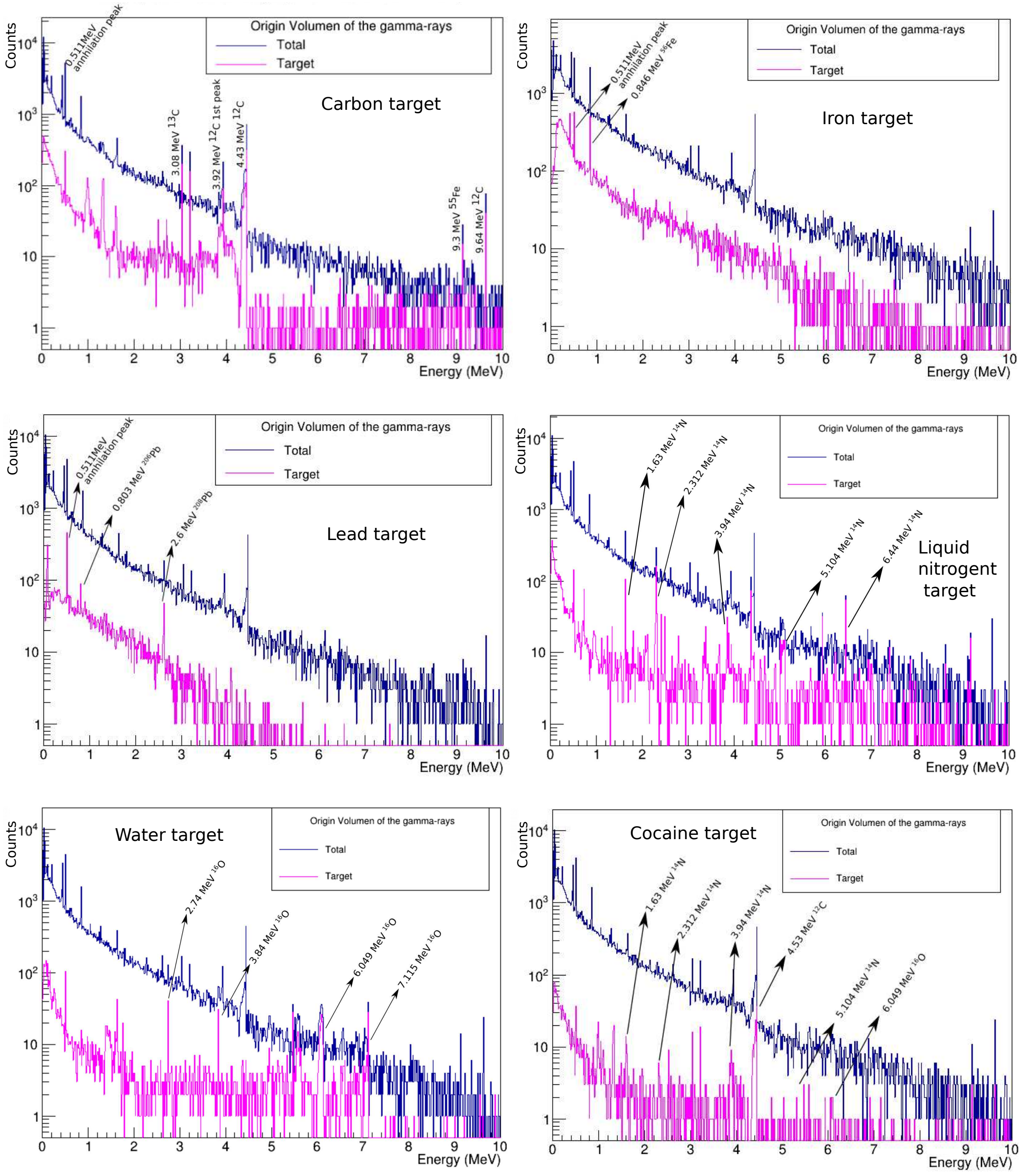

Figure 4.9: Simulated gamma-ray energy spectra, using various target compositions, including carbon, iron, lead, liquid nitrogen, water, and a simulant of cocaine. Simulation conducted with 3x10^7 events, using neutrons with an energy of 14 MeV and a Time of Flight (ToF) window of 80 ns.

4.2.5 Optimization of the setup geometry

The initial configuration of the TNIS system in the C-BORD project featured an aperture angle of 20° and a distance of approximately 58.5 cm between the detector frame and the polyethylene (PE) box [22, 30]. Based on prior experience and background knowledge, a new configuration was proposed for the ENTRANCE project. This new setup featured an aperture angle of 34.94° to increase the beam size, and the frame was moved 36 cm closer to the PE box, reducing the distance between the PE box and the frame to 22.5 cm. This adjustment aimed to ensure that the larger tagged neutron beam passing through the conical hole did not collide with the edges of the circular aperture in the iron frame diameter. Despite this new geometry being defined, it was not optimized or verified through simulations. Thus, in this work, we proceed to verify the improvement of this change.

To determine the optimal distance between the PE box, frame, and target (as illustrated in Figure 4.2), three simulations were conducted, each altering the distances between these components. The first simulation involved shifting the frame 52.5 cm farther from the PE box, which approximated the initial C-BORD configuration of the TNIS. The second simulation mirrored the current proposed experimental setup in the ENTRANCE project, with a 22.5 cm distance between the frame and the PE box. In the third simulation, the frame was completely attached to the PE box. All simulations were conducted using a carbon target. A scheme illustrating the three positions of the frame with respect to the PE box can be seen in Figure 4.10.

Figure 4.11 displays the Time of Flight (ToF) spectra for these configurations.When the frame is shifted 52.5 cm away from the PE box (blue line), the correlated background increases significantly, with a notable bump caused by back-scattered neutrons nearly reaching the target peak. Moreover, if a time resolution (with a FWHM of a few ns) is applied to the detectors, as in experimental scenarios, the bump and the target peak overlap. On the other hand, when the frame is placed 22.5 cm away from the PE box (red line), the background decreases, but the optimal position is achieved when the frame is completely attached to the PE box (pink line). This configuration results in the least background noise and the best separation between events from the target and the frame.

Even though it would be ideal to attach the frame directly to the PE box for optimal performance, practical constraints make this setup challenging. The frame is supported by legs that prevent it from being placed closer to the PE box. Despite this, a 22.5 cm gap between them is a reasonable compromise and still provides better results compared to the original C-BORD project setup.

In conclusion, the pre-established configuration with a 22.5 cm distance between the frame and the PE box is confirmed as the optimal geometry. This setup ensures a clear separation between the main peaks corresponding to the PE box, frame, and target, minimizing interference from the correlated background with the target peak. This separation is crucial for accurately identifying the inspected material. Future improvements could involve exploring alternative ways to support the frame without hindering its proximity to the PE box, thereby further enhancing measurement accuracy.

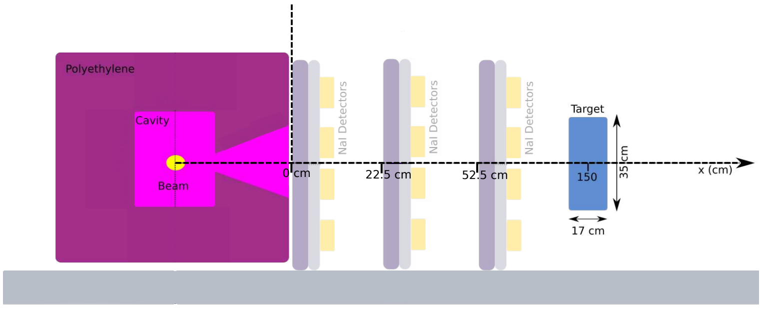

Figure 4.10: Schematic view of the RRTNIS experimental setup, illustrating the three different positions of the frame in relation to the PE box.

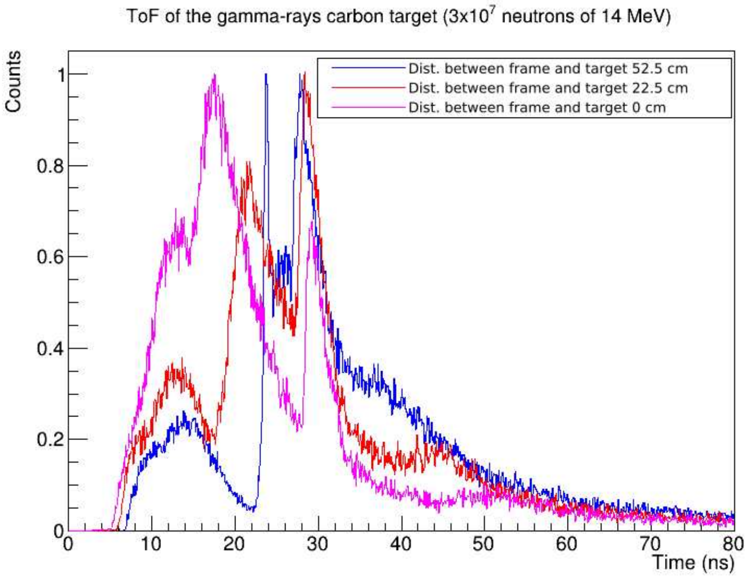

Figure 4.11: ToF spectra of the gamma-rays that reach the detector. Simulation performed with 3x10^7 events, with neutrons of 14 MeV and a ToF window of 80 ns, for a carbon target, and with different distances between the polyethylene box and the frame, 52.5 cm (blue line), 22.5 cm (red line), and 0 cm (pink line), respectively.

4.2.6 Comparison of ToF Spectra Between Experimental and Simulation Results

A comparative analysis of the Time-of-Flight (ToF) spectra between experimental and simulation results was performed. The simulation setup was designed to closely replicate the experimental conditions, incorporating both a carbon target scenario and a no-target scenario. Figure 4.12 presents the comparison, illustrating normalized counts as a function of ToF for both the experimental and simulated cases, with and without the carbon target. The ToF spectra from the experimental data were shifted along the horizontal axis to align with the simulated spectra, where the origin (0 ns) in the simulation corresponds to the moment when neutrons are emitted. To further improve the realism of the simulation data, a time resolution of FWHM = 2 ns was applied, and a background offset was introduced to account for random noise observed in the experimental measurements.

As shown in Figure 4.12, the prominent peaks in both the experimental and simulated spectra correspond to events coming from the PE box, the frame detector, and the target and back-scattered neutron peaks, the latter two appearing when the carbon target is present. Additionally, a transmission wall peak is observed between 100 and 120 ns in both experimental spectra. This peak corresponds to the wall located in front of the beam during measurements, taking into account that the measurements were performed inside the laboratory, this wall was not modeled in the simulation geometry. Notably, when the carbon target is present, the number of gamma rays originating from the transmission wall decreases. Because part of tagged neutrons are back-scattered by the target, preventing them from reaching the transmission wall. These back-scattered events appear as a distinct bump labeled 'Back-Scattered neutrons' in the spectrum of the carbon target.

From a qualitative perspective, it is encouraging to observe that the time separation between the frame, target, and back-scattered neutron peaks in both experimental and simulated spectra is very similar, with comparable distances, indicating consistency in the distance determined by the ToF measurements. However, the relative intensities of these peaks differ between the experimental and simulated results. This discrepancy may be attributed to an inaccurate representation of neutron interactions within the simulation.

In the simulation spectrum, the PE box peak appears closer to the frame peak compared to the experimental spectrum. Specifically, in the simulation, the beam was modeled as originating from the center of the PE box. The observed difference might be due to the actual position of the beam relative to the PE box in the experimental scenario, where the beam may not be perfectly centered within the cavity of the box.

In the experimental spectrum, the first peak likely represents the wall of the neutron generator, which was not included in the simulation. The second peak corresponds to the PE box. The PE box peak is due to 2.223 MeV gamma rays, which are emitted when thermal neutrons are captured by hydrogen nuclei in the PE box. The smaller relative intensity of the PE box peak in the experimental data is likely due to fewer interactions with tagged neutrons. This reduction occurs because the neutrons' emission cone is more closely aligned with the aperture of the PE box. Additionally, the simulation does not account for the neutron generator's box and the small angle required to produce a horizontal tagged neutron beam.

While the simulated and experimental spectra do not exhibit identical intensity proportions or exact time separations for all peaks, the qualitative resemblance between the two is a significant accomplishment. This is especially notable given that this is the first attempt at simulating the most realistic geometry of the TNIS setup and generating a ToF spectrum.

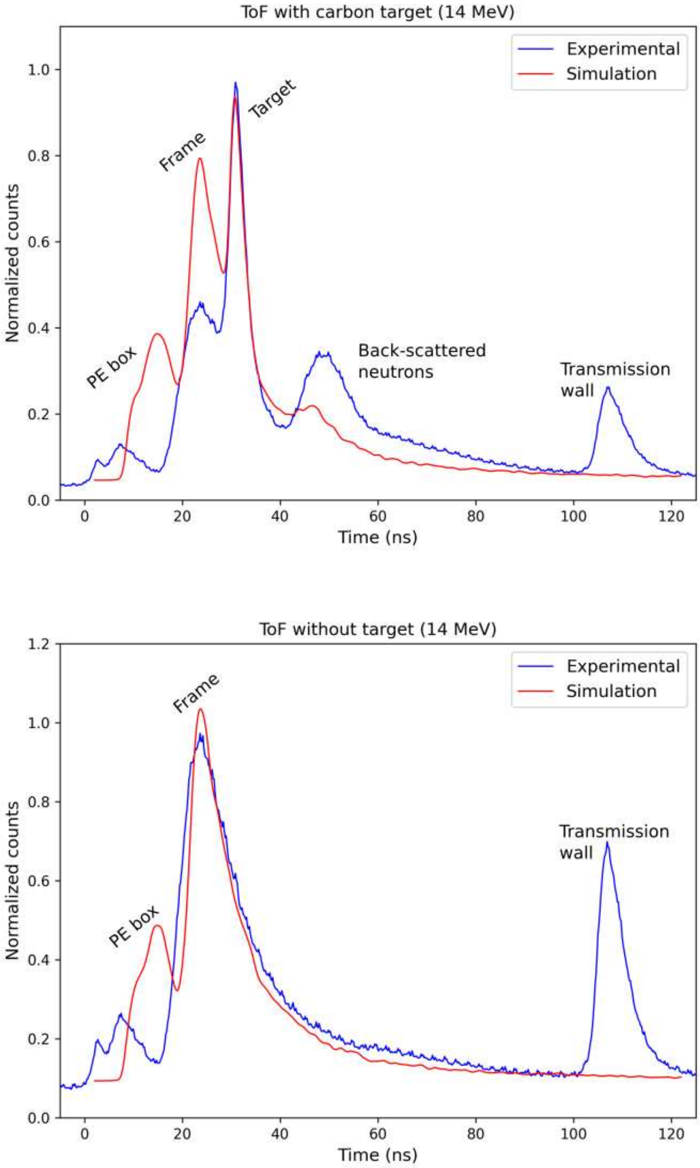

Figure 4.12: ToF comparison spectra between the experiment and the simulation, with a carbon target and without any target. Simulation performed with 3x10^7 events, with neutrons of 14 MeV, using a carbon target.

4.3 Summary

This chapter presented a comprehensive simulation study of the Rapidly Relocatable Tagged Neutron Inspection System (RRTNIS) within the ENTRANCE project, using the Monte Carlo method with the Geant4 v10.7 toolkit. The simulation accurately replicated the experimental setup's geometry, which included a polyethylene box housing the neutron beam and NaI detectors mounted on an iron frame with lead shielding. The study aimed to optimize the setup geometry, determine the Time of Flight (ToF), analyze energy deposition, investigate back-scattered neutron effects, and finally compare the ToF spectra between experimental and simulation results.

The ToF determination provided a deeper understanding of the contributions from each component within the inspection area, while the energy deposition analysis revealed specific gamma-ray peaks essential for element identification across different target materials. By restricting the ToF window, the simulations effectively filtered out unwanted background events, allowing clearer identification of gamma-ray peaks originating from the target.

The investigation into back-scattered neutrons demonstrated their significant contribution to the correlated background, particularly when using a carbon target. This insight is crucial for interpreting ToF spectra and improving the accuracy of material identification in experimental scenarios. The optimization of the setup geometry showed that the best configuration would be to have the polyethylene box attached to the detector frame. However, practical constraints, such as the legs supporting the frame, prevent this setup in a real experimental scenario. Therefore, the already defined distance of 22.5 cm between the polyethylene box and the frame represents a good compromise, minimizing background noise and ensuring a clear separation between events from the target and the frame.

The comparison of Time-of-Flight (ToF) spectra between experimental and simulation results demonstrated qualitative agreement; however, differences in peak intensities and slight mismatches in the time separations of certain peaks were observed. These discrepancies likely arise from limitations in accurately modeling realistic neutron interactions. Despite these inconsistencies, the overall similarity between the experimental and simulated ToF spectra represents a significant achievement, marking the first successful attempt to simulate the ToF spectrum of the TNIS setup.

Chapter 5

ENTRANCE field test

This chapter details the field tests conducted with the RRTNIS system of the ENTRANCE project at the Port of Rijeka, Croatia, in May 2023. The objective was to evaluate the RRTNIS system's performance in detecting hazardous materials. The field tests involved analyzing 18 mock-up and 18 commercial containers, the mock-up containers were designed to simulate various organic materials, including drugs and explosives, while the commercial containers contained a range of diverse items. Results from selected measurements are detailed in this chapter and are accompanied by plots generated using the end-user software. This software facilitated the acquisition, analysis, and material identification of the data. The chapter also includes explanations of the algorithms and data processing techniques employed by the software. From the measurements performed it was successfully identified explosive simulants, chemical warfare agents, benign materials, and cocaine, thus demonstrating the effectiveness of the RRTNIS system in identifying hazardous materials. The chapter also provides a detailed explanation of the experimental setup and data acquisition unit, as well as covering dose rate mapping and the safety measures implemented during the field tests.

5.1 Introduction

The ENTRANCE Field Tests were conducted over three weeks in May 2023 at the port of Rijeka, Croatia. These tests were made possible through the active involvement and support of Croatia Customs, the Ministry of Interior, the Ruder Boskovic Institute, and all partners involved in the ENTRANCE project. This collaboration provided an opportunity to rigorously test and evaluate various Non-Intrusive Inspection technologies being developed within the project. Realistic targets, including guns, explosives, drugs, contraband, and live radioactive sources, were concealed in containers to ensure that the technologies were thoroughly evaluated in challenging, real-life scenarios. [11].

Specifically, for the assessment of the RRTNIS system, 18 mock-up containers and

18 commercial containers were tested in the campaign. The mock-up containers simulated by the customers of the port were loaded with various organic materials such as drugs (simulants and real), explosives (simulants and real), Teflon, sugar, salt (NaCl), sodium sulfide (NaS), fertilizer, flour, and tobacco. In contrast, the commercial containers were declared to be loaded with diverse items including PET material, electronic devices, bananas, tobacco, electronic cigarettes, wood, refrigerators, tubes, pineapples, household electronics, tea, plastic, screws, cartons, and shoes. This chapter presents some of the results obtained during the field tests with the TNIS system, highlighting the technique's efficiency in identifying hazardous materials. Additionally, it explains the analysis of the measurement data and the results displayed in end-user software.

Figure 5.1 shows a map of the ENTRANCE technologies located at the Rijeka port. Red arrows indicate the course of the inspected trucks. Initially, trucks underwent first-line inspection with an X-ray scan. If suspicious zones were detected, an alert was sent to the TNIS personnel to proceed with a second-line inspection using the TNIS. The truck driver was then asked to move the truck a couple of meters and position it in front of the TNIS. The driver was instructed to park the truck with the suspect zone in front of the beam aperture, guided by the TNIS personnel. The lifter was then moved to position the beam correctly in front of the zone along the vertical axis (as seen in Figure 5.8), and the measurement was performed.

For a comprehensive understanding of the RRTNIS functioning, refer to the detailed explanation in Subsection 3.3.1. My group and I were responsible for the mounting and dismounting of the TNIS system at the Rijeka port. Additionally, we participated in all measurement campaigns, analyzed the results, and prepared the final inspection reports required for submission to the EU Commission.

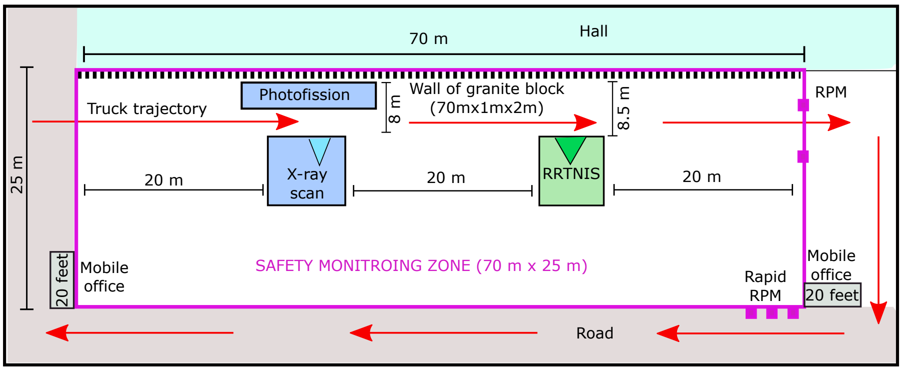

Figure 5.1: Map showing the ENTRANCE's technologies located at the Rijeka port

5.2 Detailed experimental setup of the RRTNIS

The RRTNIS system in the ENTRANCE project comprises 20 NaI:Tl detectors, each measuring 12.7 x 25.4 x 12.7 cm^3, with an energy resolution ranging between 6% and 8.5% at 662 keV. These detectors originated from the FP6 EURITRACK project [16].

During the recent C-BORD project [22], some of the original Photonis XP4512B photomultiplier tubes were replaced with Hamamatsu R11833-100HA PMTs featuring an active voltage divider [47]. Notably, improvements were made to the system's geometry compared to the C-BORD project [22], in order to reduce the background. These include widening the cone aperture in the polyethylene (PE) radiological shield to 34° (from 20° in C-BORD) and relocating the detector holder and lead plates closer to the neutron generator (80 cm away). An illustration of the schematic setup is shown in Figure 5.2, where the neutron generator is encased in a polyethylene shield for radiation protection. The figure also depicts the total aperture angle of 34°, the detector holder, and some of the detectors, with the view from above. For further details on the upgrading and construction of the TNIS, refer to [16, 30, 48, 49].

The main components of the TNIS in the ENTRANCE project include the neutron generator, surrounded by polyethylene shielding, gamma-ray detectors positioned in front of the generator, detectors held by a 1.5 cm thick iron frame, and a 5 cm thick lead shield to reduce the gamma background produced by the neutron generator inside the polyethylene shield (occurring through inelastic scattering and radiactive capture reactions in C and H nuclei, respectively). For the field test, the setup is housed in a 10 ft external case containing all necessary electronic equipment for data acquisition and PMT power supply (data acquisition unit explained in detail in Subsection 5.2.1). Additionally, a lifter enables the RRTNIS to be elevated up to 4 meters high for operational flexibility. More detailed information about the experimental setup can be found in Subsections 3.3.1 and 4.2.1.

Figure 5.3a shows the TNIS experimental setup in the laboratory, while Figures 5.3b-d show pictures from the field test, illustrating the TNIS inside the external case and on the lifter. Additionally, it is seen in front of a container, positioned before inspecting the container. Moreover, Figure 5.3d shows the air conditioning unit installed in the external case to manage high temperatures during measurements.

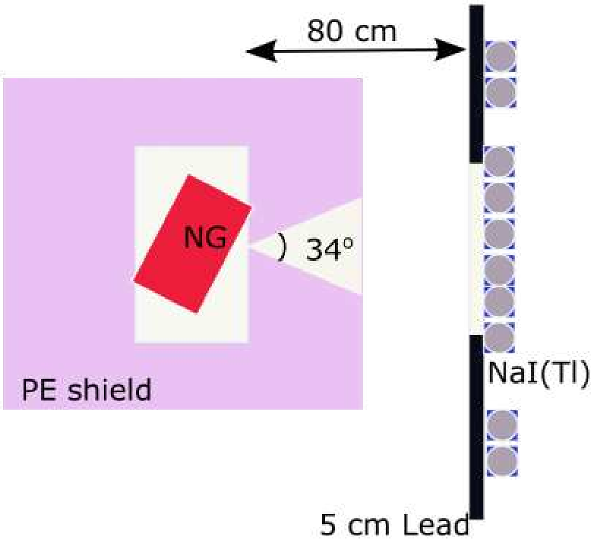

Figure 5.2: Layout of the ENTRANCE TNIS

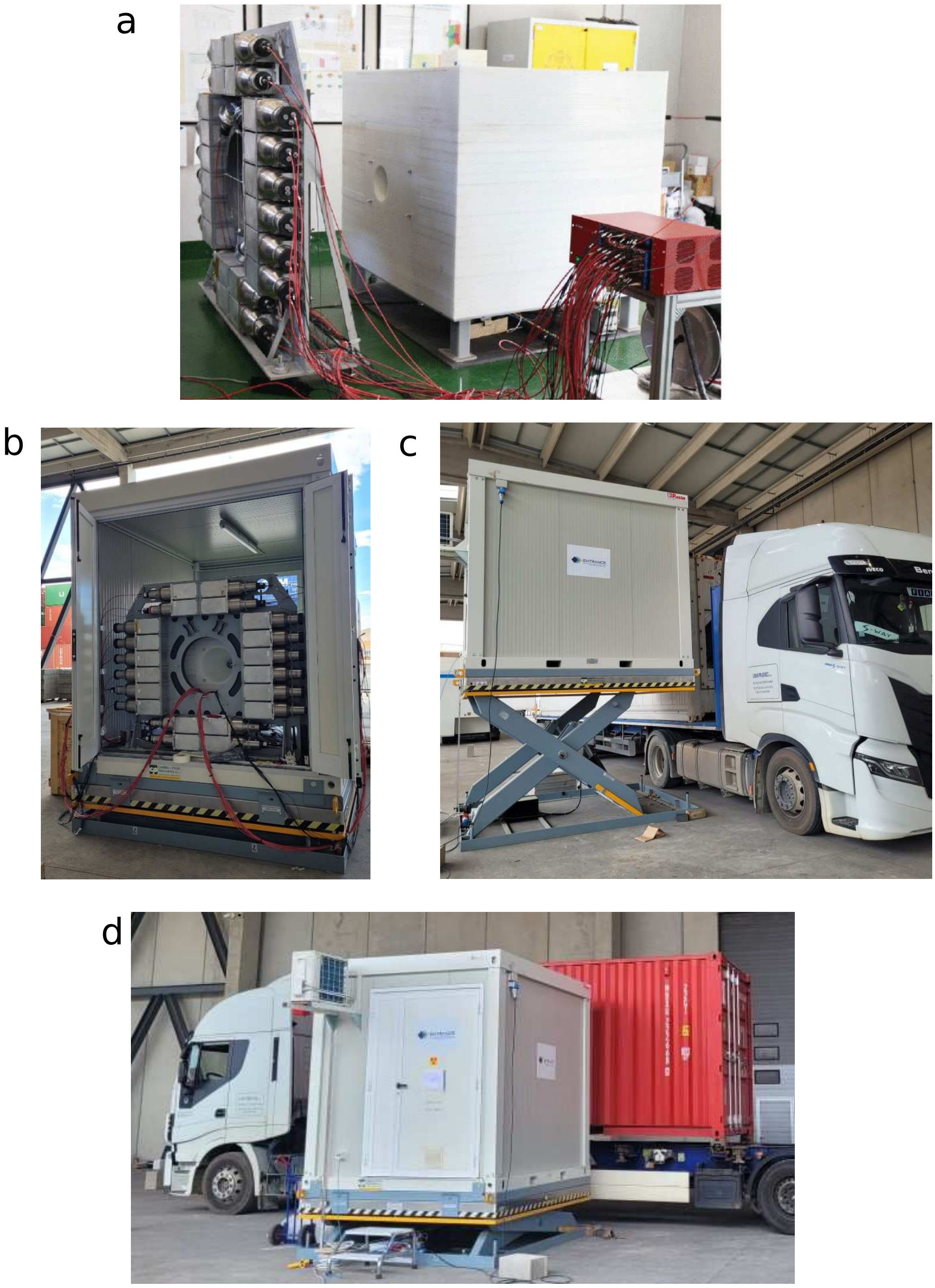

Figure 5.3: Configuration of the RRTNIS System: (a) RRTNIS at the Laboratory, (b)-(d) RRTNIS inside the external case and positioned on the lifter at different heights for container irradiation at the Rijeka Port

5.2.1 Data acquisition unit

The nuclear signal processing electronics system consists of two CAEN V1730 VME digitizers, five CAEN V6533 VME high voltage supplies, one CAEN V2718 VME-PCI optical link bridge, and optical fiber connections utilizing the CAEN CONET2 protocol for fast data acquisition. The system is controlled by a computer, running the open-source data acquisition software ABCD (Acquisition and Broadcast of Collected Data) [50, 51], developed as part of the C-BORD project.

The data acquisition system is configured to treat the digitizers as independent modules without synchronization. Each digitizer internally validates acquired signals only if a coincidence is detected between the alpha signals (X, Y, and SUM signals from the YAP:Ce detector, where SUM is proportional to the sum of the integrals of X and Y) and at least one of the gamma-ray detectors. Non-validated signals are discarded. Figure 5.4 details the connection scheme. The X, Y, and SUM signals from the YAP:Ce detector are also used to create the alpha XY map, a 2D plot ("X direction" versus "Y direction") that shows the interaction position of the alpha particles in the scintillator [52].

Under these settings and with a neutron emission rate of 7×10^7 s^{-1}, the system records approximately 4×10^5 events per second per digitizer across all channels. The DAQ system is capable of sustaining rates up to 4×10^5 events per second under similar conditions, with a 1% dead time [50, 51]. During neutron inspection, about 700 MB of data is generated per minute. This data is stored in binary format, containing channel, timestamp, and energy details for each detected event [52]. Subsequent data analysis is carried out offline using the end-user software outlined in section 5.4.

It is important to notice that from the expert-user software, it is possible to also make a selection of the event using the data obtained from the YAP:Ce detector, where a particular direction of the neutron beam can be selected, by defining an ROI on the alpha XY map. Nevertheless, this selection inside the end-user software is not possible.

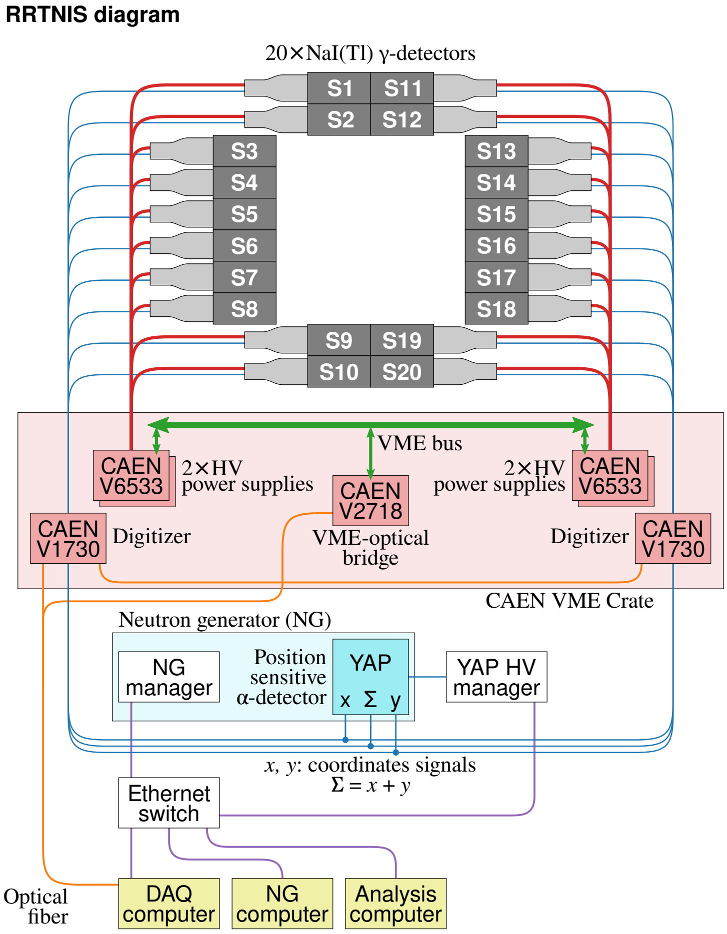

Figure 5.4: Schematic representation of the connections between the components of the RRTNIS detection module. Figure taken from: [52] and modified.

5.3 Dose Rate Map

This section presents the results of dose rate mapping for neutron and gamma-ray radiation using the geometry depicted in Figure 5.2. This setup includes a beam aperture of 34°, and the detector holder with lead plates positioned 80 cm from the neutron generator. The dose maps were calculated using the Monte Carlo method with the Geant4 toolkit v10.7. The geometry of the experimental setup was replicated in the simulation as explained in Subsection 4.2.1. The dose rate maps are presented at a height of 1.5 m above the ground level and were performed with two different neutron fluxes.

- Maximum Neutron Flux (1x10^8 n/s): This flux represents the maximum neutron output of the neutron generator, essential for authorization requests during field tests.
- Working Neutron Flux (2x10^7 n/s): This flux was used during measurements conducted at the Rijeka port, balancing statistical reliability with minimal induced background levels.

Figure 5.1 shows a map of the ENTRANCE's technologies located at the Rijeka port. In this map, a wall is located in front of the incident beam of the RRTNIS system at a distance of 8.5 m, providing sufficient space for placing the container between the RRTNIS and the wall. This wall serves as shielding to prevent radiation from traveling further while the containers are being irradiated with the TNIS. In the simulation for the dose map calculation, this wall was added, located 8.5 m away from the neutron generator, with a thickness of 1 m. The floor was also included, and both structures were modeled using concrete material.

Figures 5.5 and 5.6 present the dose rate maps for the two neutron fluxes (1x10^8 n/s and 2x10^7 n/s) under the Rijeka field test conditions, with a minimum dose rate set to 1 μSv/h and a maximum limit set to 10 μSv/h. Based on these results, during the irradiation process performed by the RRTNIS at the Rijeka port, a safety monitoring zone of 30 m x 25 m was established for the RRTNIS. However, since the X-ray scan was next to the RRTNIS, as seen in Figure 5.1, a total safety zone of 70 m x 25 m was established for the operation of both technologies. Entry into this zone was prohibited while the beam was active for either technology. Once the beam was turned off, personnel were allowed to enter, as non activation of the materials had occurred. It is important to note that measurements with various dosimeters were conducted after irradiation to verify that non activation had occurred and to ensure a safe environment.

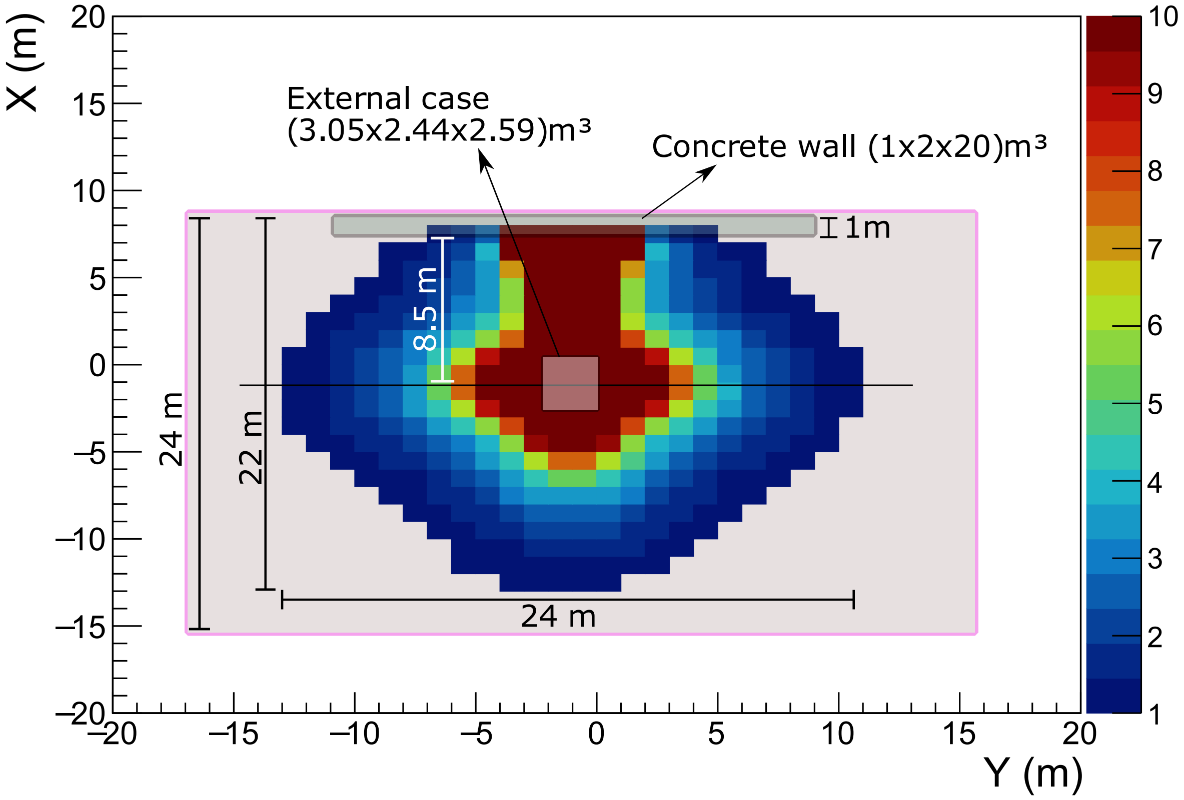

Figure 5.5: Dose rate map in the field test site of Rijeka port with a neutron flux of 1x10^8 n/s.

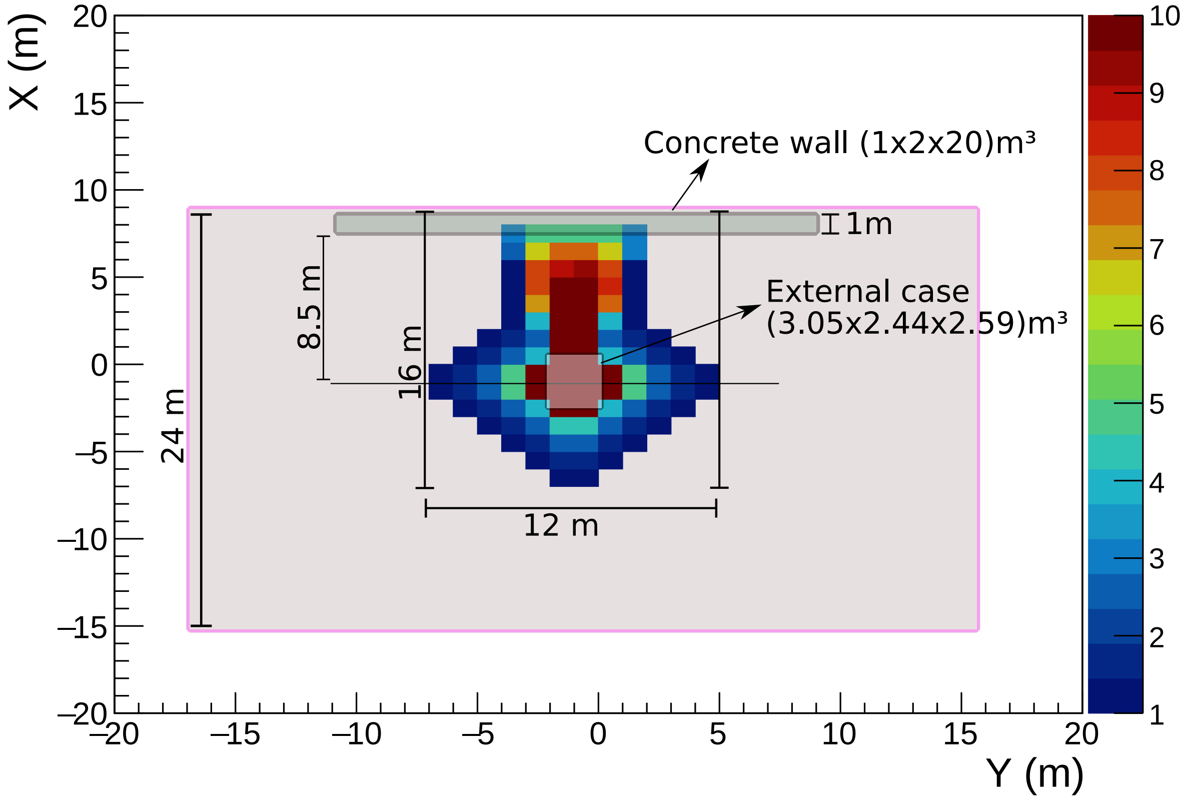

Figure 5.6: Dose rate map in the field test site of Rijeka port with the working neutron flux of 2x10^7 n/s.

5.4 Data analysis software

Gamma rays detected by the 20 NaI:Tl detectors, in conjunction with alpha particles detected by the YAP:Ce detector, are digitized for further analysis. Using this data, along with specific algorithms and analytical techniques, it is possible to identify what is inside the containers, an analysis that will be discussed in detail in this section.

Notably, for the Rijeka field tests, an end-user software was developed and tested at the Rijeka port. The tests demonstrated that the software is both stable and user-friendly, enabling port operators to perform simple measurements of containers and obtain clear results about the materials inside, without needing expert knowledge for data analysis. This software was developed by the CAEN company [53] in collaboration with a research group from CEA PARIS-SACLAY [54]. The data analysis is carried out by algorithms within the expert mode software, upon which the end-user software is based.

The data analysis process for each measurement involves several steps. First, energy and distance calibration are performed, taking into account that the Time of Flight (ToF) measurement corresponds to the distance at which neutron inelastic scattering occurred. Following this, a background processing is applied to the data, followed by a deconvolution method. Finally, a material classification is carried out, including the identification of organic materials [48]. Each of these steps will be illustrated with plots obtained from the end-user software. For this explanation, we will use a measurement conducted at the Rijeka port, specifically a container (mock-up 16) filled with various materials, including a nitrogen-free explosive simulant (TATP - $C_9H_{18}O_6$) hidden inside. It is important to note that the number given to each mock-up or commercial container represents the labeling used during the measurement campaign.

- Positioning and Irradiation: The first-line NII inspection system of the ENTRANCE project involves scanning the container with a mobile X-ray scanner without disrupting it (as detailed in Subsection 2.1). If the initial scan reveals a suspicious zone containing organic material that cannot be cleared by the First-line X-ray scanner, the RRTNIS (Neutron Inspection System) is activated. The X-ray images from the mobile scanner are transmitted to the RRTNIS via ENARTIS, a server that facilitates communication and data transfer between the ENTRANCE technology systems. In the end-user software, these X-ray images are displayed, with the suspicious zones marked by yellow circles, and in blue, the current suspicious zone analyzed by the TNIS, as shown in Figure 5.7, which depicts the X-ray image of mock-up 16.

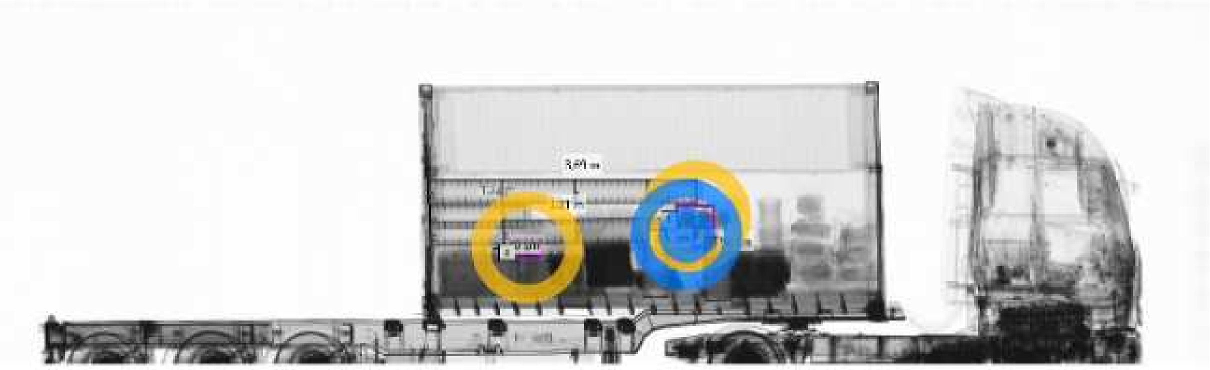

Figure 5.7: X-ray image of mock-up 16 at the Rijeka port, as displayed in the end-user software of the RRTNIS, with the suspicious zones marked by yellow circles.

With the location of the suspicious zone identified, the container is positioned so that this zone is directly in front of the RRTNIS beam. Positioning involves first instructing the truck driver to move the truck to the specified distance, as shown in Figure 5.8a, and then adjusting the TNIS vertically using a lifter, as seen in Figure 5.8b until it reaches the correct position. For this inspection, the beam was centered 2.7 meters above the ground and 3.1 meters from the back of the container, corresponding to the blue circle in Figure 5.7.

Figure 5.8: Pictures from the Rijeka port illustrating the positioning of the container in front of the beam before irradiation and inspection with the TNIS.

Once positioning is complete, all personnel in the restricted zone are instructed to evacuate. Irradiation then begins with a neutron flux of 2x10^7 n/s for approximately 15 minutes. The beam is active, and data acquisition is managed entirely through the end-user software. Upon completion of the measurement, the data is processed by the end-user software through a series of steps.

- Calibrations:

  The data analysis begins with the calibration of the detectors, including both energy and distance calibration. These calibrations are performed automatically within the end-user software. The energy calibration involves a linear adjustment of all detectors based on the total spectrum and several characteristic peaks, which may vary depending on the detectors or runs. Calibration steps include pre-calibration, primary and secondary calibrations, and a final calibration check. Notably, during the secondary calibration, the photo-peaks of iron (0.847 MeV), hydrogen (2.223 MeV), and carbon (4.439 MeV) are utilized, corresponding to elements present in the setup.

  The Time of Flight (ToF), defined as the time between the emission of the neutron and the detection of the gamma ray, is used to determine the distance of the object. Therefore, distance calibration involves a linear correction based on the first major peak in the ToF spectrum, corresponding to the iron plate that holds the detectors (as seen in Figure 5.9b). Additionally, within this peak, there are events originating from the wall of the external case that cannot be distinguished from those associated with the detector holder, due to the small distance between these objects (approximately 15 cm), which corresponds to a time difference of about 3 ns. Given the detectors' time resolution (FWHM = 2 ns), these events cannot be differentiated.

Initial plots in the end-user software show the gamma-ray energy and distance spectra after calibration, as depicted in Figure 5.9. These spectra represent the total sum of all events detected by the 20 NaI:Tl detectors. Figure 5.9b displays the distance spectrum with two prominent peaks, corresponding to gamma rays resulting from neutron inelastic scattering on the RRTNIS structure and the container. Figure 5.10a shows the distance spectrum with a range starting from 0 cm, while Figure 5.10b presents the gamma-ray energy spectrum as a function of distance. Two main peaks around 100 cm indicate the suspected location of the explosive material. Figure 5.10c illustrates the gamma-ray energy spectrum for the selected region, highlighting the photo-peak at 4.4 MeV for carbon, 6.13 MeV for oxygen, and 0.847 MeV for iron.

It's worth noting that the expert-user software allows for event selection based on data from the YAP:Ce detector, enabling the specification of neutron beam direction via a defined Region of Interest (ROI) on the alpha XY map. In contrast, this capability is unavailable in the end-user software.

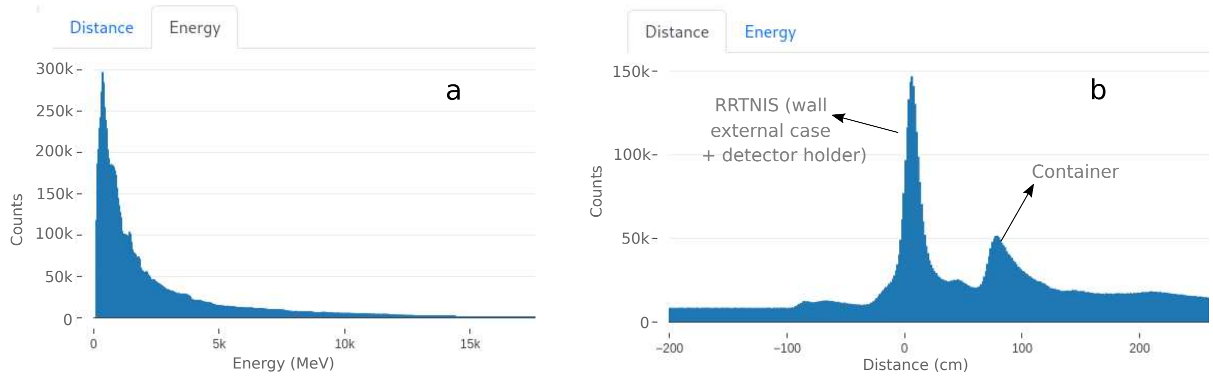

Figure 5.9: Gamma-ray energy and distance spectra of mock-up 16.

- Background Processing:

  The background consists of two components: a random component and a correlated component. The random background is estimated based on the average number of counts at a given energy for non-physical (negative) distances. This background arises from the fortuitous detection of a gamma ray (or sometimes a neutron) that is not correlated with the alpha particle that initiated the current coincidence window. In contrast, the correlated background arises from tagged neutron interactions with surrounding materials. Both random and correlated background are included in the pure element spectra library, they are not removed, allowing them to be adjusted during deconvolution in the same manner as the pure elements. The energy distribution of the random background is uniform across different energies, whereas the energy distribution of the correlated background varies.

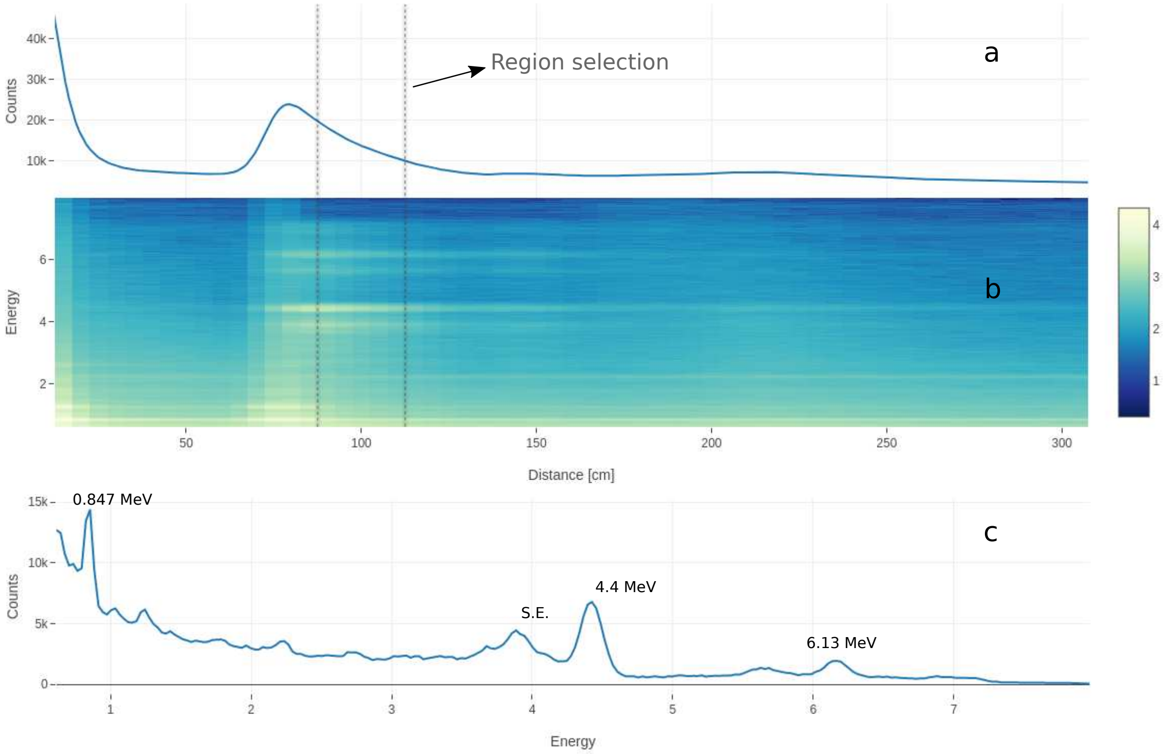

Figure 5.10: Distance spectrum of mock-up 16 (a), gamma-ray energy spectrum as a function of distance (a), and gamma-ray energy spectrum for the region selected (c) in (a) and (b).

- <u>Deconvolution Method:</u>

  The deconvolution process employs the Non-Negative Least Squares (NNLS) algorithm, utilizing a database of 20 pure element spectra (aluminum, carbon, calcium, chlorine, chromium, copper, fluorine, iron, potassium, magnesium, manganese, nitrogen, sodium, nickel, oxygen, phosphorus, lead, sulfur, silicon, and zinc) as well as background spectra. This method estimates the contribution of each element by unfolding the measured spectrum. NNLS constructs a model with non-negative coefficients to determine the composition of each spectrum in a single computation. Synthetic spectra are generated using a Poisson distribution based on the measured spectrum. Each measured spectrum produces 500 synthetic spectra, which are analyzed using NNLS to yield 500 compositions per spectrum. These compositions provide distributions of probable element proportions, which are fitted with Gaussian curves. The mean of these curves represents the most likely proportion, while the standard deviation indicates uncertainty.

After deconvolution, the end-user software provides plots, such as those in Figure 5.11, which illustrate the identified elemental count fractions in percentage in function of the distance (a qualitative result). The plots indicate that the area suspected of containing explosive material shows a high concentration of carbon and oxygen, and a very small portion of nitrogen, but this last one could be due to an overestimation by the deconvolution method of the nitrogen content, considering that the explosive material under analysis (TATP) has no nitrogen content.

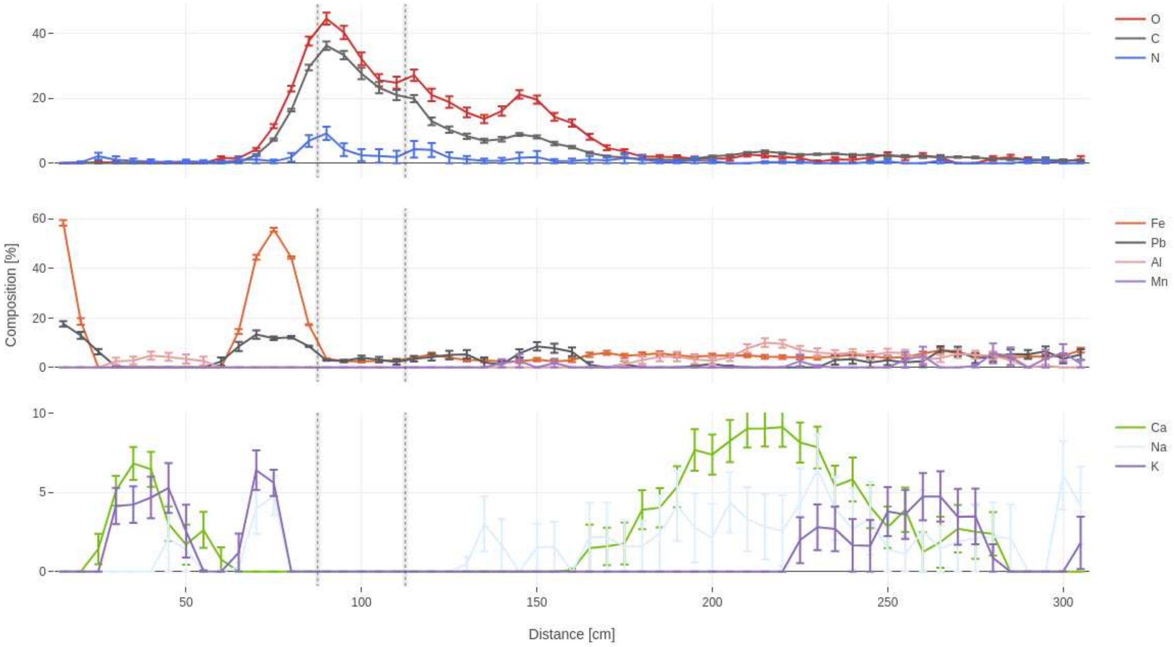

Figure 5.11: Count proportions attributed to each element of the measurement performed with mock-up 16 as a function of distance.

- Material Classification:

  Based on the elemental count fractions, materials are classified into the following categories:

  - Organic: carbon (C), nitrogen (N), oxygen (O)
  - Metallic: aluminum (Al), iron (Fe), chromium (Cr), copper (Cu), nickel (Ni), lead (Pb), zinc (Zn)
  - Ceramic: silicon (Si)
  - Chemical: calcium (Ca), chlorine (Cl), fluorine (F), potassium (K), magnesium (Mg), manganese (Mn), sodium (Na), phosphorus (P), sulfur (S)
  - Other: random and correlated backgrounds

The probability that the inspected target belongs to a given category is calculated by the ratio of the weights of the pure elements within that category to the total sum of weights.

Material classification in the end-user software is illustrated with radar plots, as shown in Figure 5.12. Figure 5.12a provides an intuitive representation of the elemental count fractions in the selected zone, while Figure 5.12b shows the material classification abundance. The plots indicate that the selected zone predominantly consists of organic material, as evidenced by the high abundance of carbon and oxygen. The classification shows minimal presence of metals, ceramics, or chemicals.

- Organic Material Classification:

  The primary objective of the RRTNIS system is to identify illegal organic materials such as drugs, explosives, and illicit tobacco. To effectively distinguish these from benign substances like wood, paper, and cotton, it is crucial to analyze their relative proportions of carbon, oxygen, and nitrogen.

  During the unfolding process, the system provides count fractions which, by themselves, do not directly reveal the chemical proportions of carbon, nitrogen, and oxygen. To address this, conversion factors are applied to translate these count fractions into chemical ratios (N/C and O/C), using carbon as the reference element. The corrected fractions, are computed from the formulas:

$$C = \frac{c}{CNO}$$

$$N = \frac{n}{\text{(N/C) conversion factor} \cdot CNO}$$

$$O = \frac{o}{\text{(O/C) conversion factor} \cdot CNO}$$

  where,

  - c, n, and o are the unfolded count fractions for carbon, nitrogen, and oxygen.
  - (O/C) conversion factor = 1.94 and (N/C) conversion factor = 1.56. The correction factors compensate for the photon attenuation and neutron spectral changes caused by the cargo itself [55].
  - $CNO = c + \frac{n}{\text{(N/C) conversion factor}\cdot CNO} + \frac{o}{\text{(O/C) conversion factor}\cdot CNO}$

  Then, the chemical ratios (N/C and O/C) are visualized using a barycenter triangle diagram, similar to the Dalitz plot used in particle physics. This triangle diagram plots the N/C and O/C ratios for common explosives, illicit drugs, and benign materials, delineating distinct regions for these categories, as illustrated in Figure 5.13. The plot clearly demarcates areas where explosives (red points), drugs (blue points), and benign materials (green points) are likely to be found within the triangle.

The classification of new data points is achieved through the k-nearest neighbors (k-NN) algorithm [56], a widely used and straightforward machine learning classifier. The k-NN algorithm assigns a class to the new data point based on the majority class of its k nearest neighbors, ensuring accurate classification as an explosive, drug, or benign material.

The results are presented in the end-user software, beginning with a radar plot that shows the proportions of explosive, benign, or drug material in the selected region, as seen in Figure 5.12c. For mock-up 16, the system effectively identified the explosive material. Additionally, the Dalitz triangle plot (Figure 5.13) provides a more specific identification of the explosive type [48]. The plot includes common explosives, illicit drugs, and benign materials, with mock-up 16's measurement aligning closely with the TATP area. The list on the left side of Figure 5.13 highlights potential organic materials that closely match the composition of the examined material, specifically wood and cotton, which have a similar elemental composition compared to TATP.

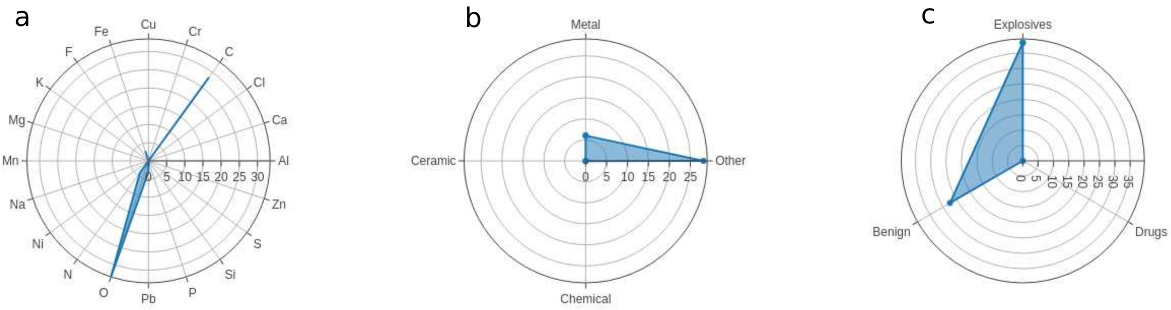

Figure 5.12: Radar plots for mock-up 16 showing: (a) elemental composition, (b) material composition, and (c) the type of organic material composition in the previously selected zone in Figure 5.10.

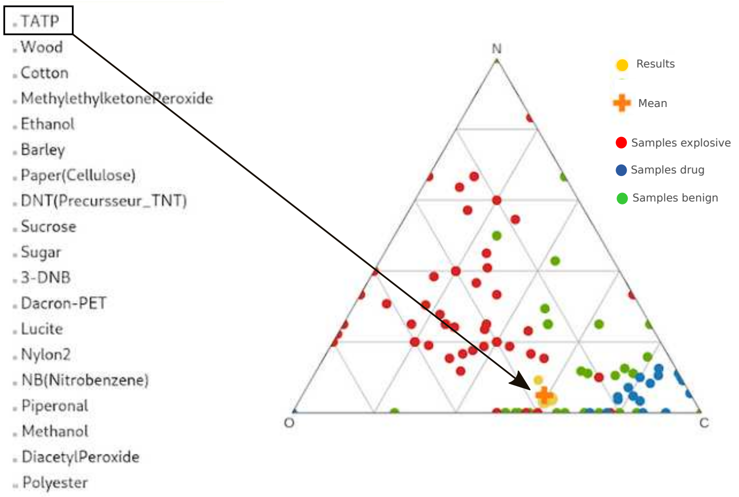

Figure 5.13: Dalitz triangle plot for mock-up 16 showing the composition of organic materials.

- <u>Material Profiles:</u>

  Another useful plot provided by the end-user software shows the different material types in percentage in function of the distance, as seen in Figure 5.14. This plot clearly displays the metal material comprising the wall of the TNIS's external case and the container wall. Beyond the container wall, it reveals the materials inside the container according to their depth, enabling the clear identification of explosive material. This plot is highly valuable for operators, as it allows them to visualize the material composition relative to depth. Operators can then select specific regions of interest, where further analysis is performed, resulting in the plots shown previously Figures 5.10, 5.11, 5.12, and 5.13, based on their selections.

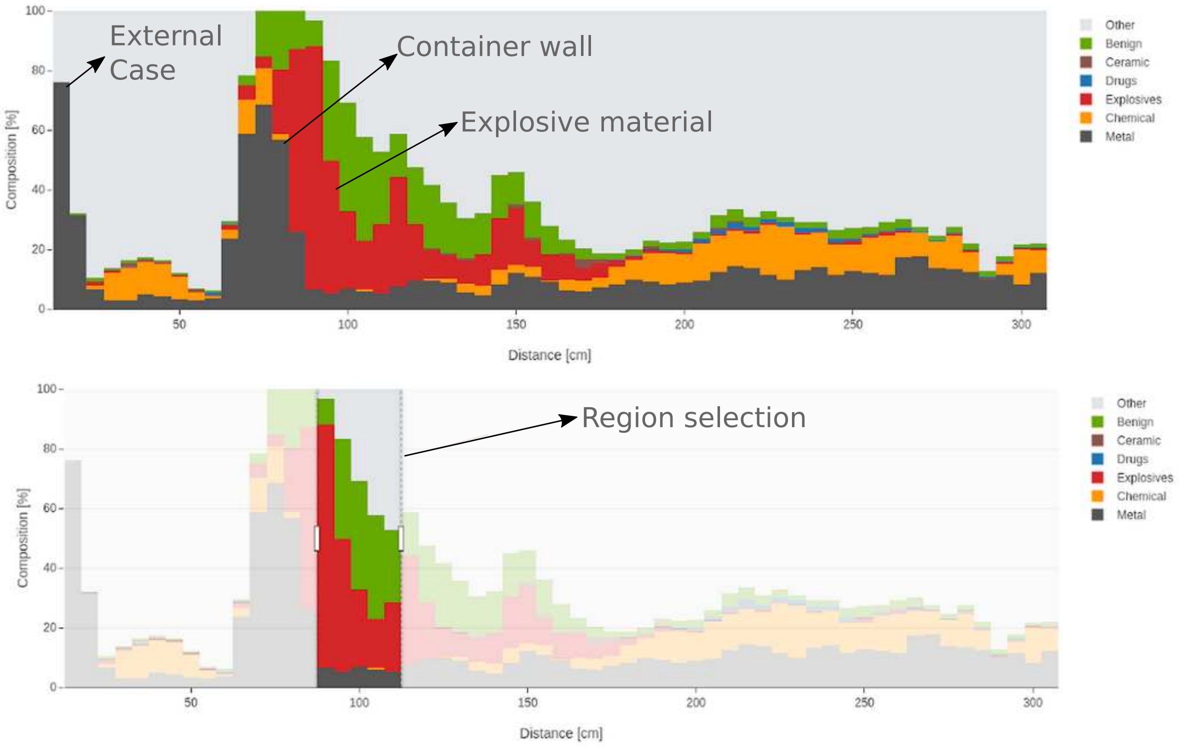

Figure 5.14: Material profile as a function of distance for mock-up 16.

5.5 Results and analysis

This subsection presents the results obtained from the Rijeka field test using the RRT-NIS system. The results include data from 3 of the 18 mock-up containers inspected and 2 of the 18 commercial containers. For each measurement, selected plots provided by the end-user software are presented, highlighting key findings.

5.5.1 Mock-ups Containers

1. Mock-up 4 filled with sulfur, sodium and chlorine chemicals:

   To test the system's capability of identifying chemical warfare agents, a container was filled with 3 bags of sulfur (1 kg each) and 3 bags of NaCl (5 kg each), elements potentially present in chemical warfare. The results are shown in Figure 5.15, where the material profile recognizes the chemical compounds. After selecting the events around 80 cm, the elemental composition plot identifies chlorine, sulfur, and sodium in that region. Additionally, phosphorus is identified, likely due to a deconvolution error, as the gamma-ray spectra of phosphorus and sulfur used for the deconvolution are quite similar, as can be seen in Figure 5.16. Both spectra have two main peaks with similar energies around 2230 MeV and 1266 MeV. To avoid such misunderstandings in future work, it is necessary to differentiate these spectra more effectively, possibly by prioritizing other gamma-ray peaks with different energies. Despite this error, the chemical warfare simulant was identified, as seen in the radar composition plots (Figure 5.15c).

a) Material Profile

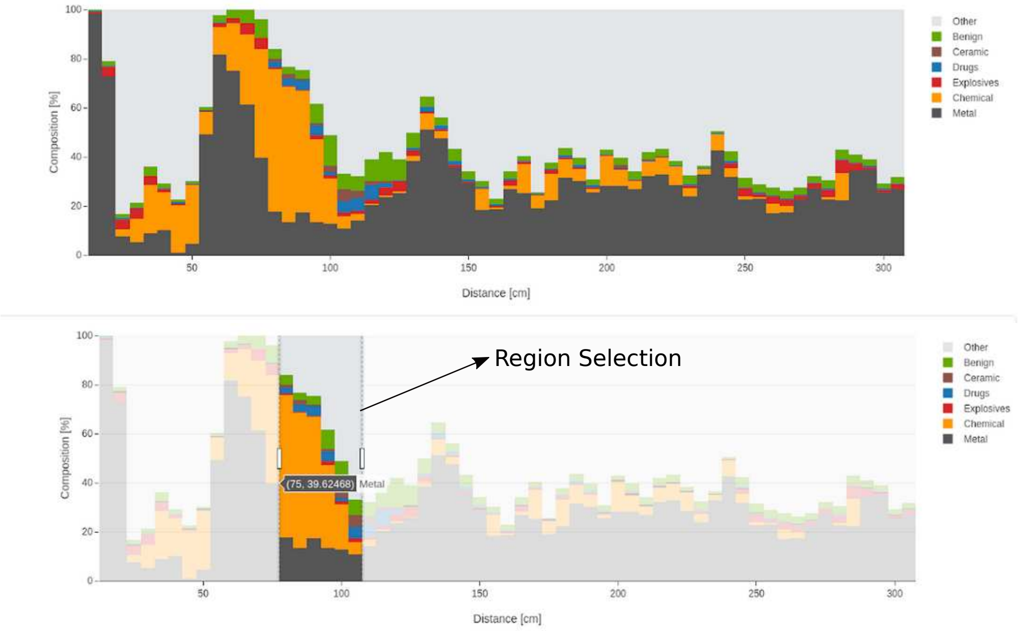

b) Elemental composition

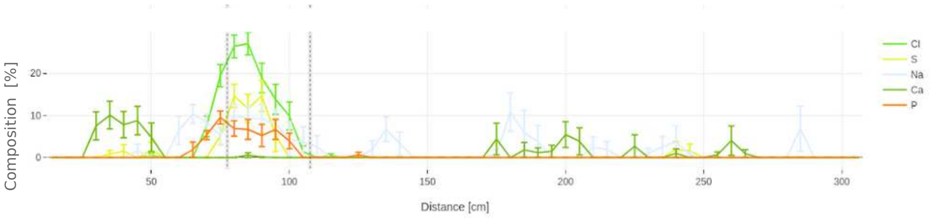

c) Radar composition Plots

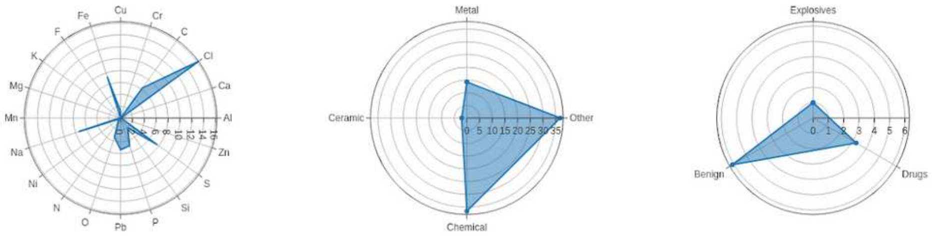

Figure 5.15: Material profile (a), count proportions attributed to each element (b), and radar composition (c) plots of Mock-up 4, filled with chemical warfare simulants

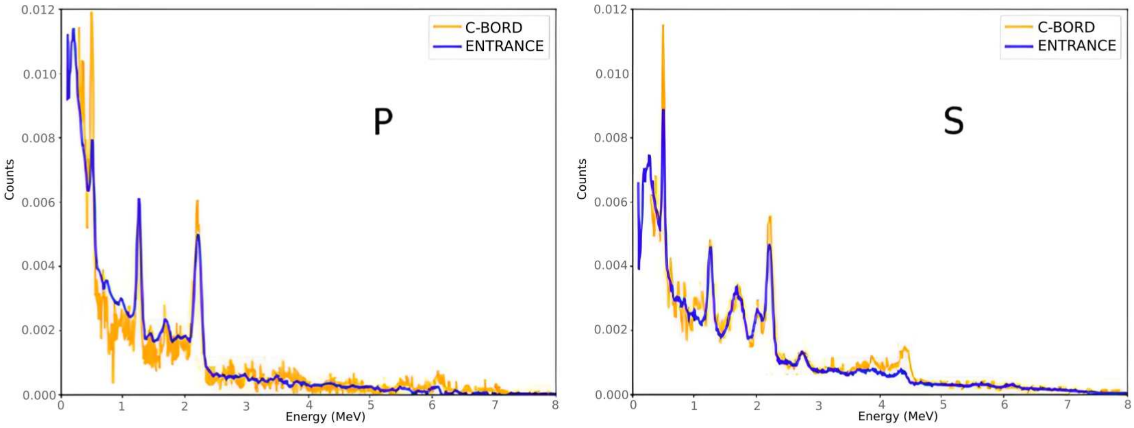

Figure 5.16: Experimental gamma-ray spectra of phosphorus and sulfur measured in the C-BORD project (in orange) and the ENTRANCE project (in blue). Plots taken from: [30].

2. Mock-up 5 filled with real explosives (TNT+PENTRIT):

   Real explosives containing nitrogen (4 kg of TNT $C_7H_5N_3O_6$ and 1 kg of Pentrite $C_5H_8N_4O_{12}$) were hidden inside the container at an unknown location, which was later localized inside the container with the X-ray scanning. The suspected area was later irradiated with the TNIS system and the end-user software generated the results shown in Figure 5.17. The material profile clearly identifies the walls of the external case and the container. Beyond the container wall, a suspect explosive material is localized around 100 cm, as shown in Figure 5.17a. A selection is made around this region, and further plots are generated based on this selection. The spectrum unfolding reproduces the data well, indicating a material with elemental composition of oxygen, carbon, and nitrogen (Figure 5.17b), with nitrogen content being a clear sign of explosive material. The radar composition plot (Figure 5.17c) again shows the elemental composition of oxygen, carbon, nitrogen and iron, iron corresponding to the wall of the container as can be seen in Figure 5.17b. The deconvolution identifies the organic material as corresponding to an explosive material. Finally, the triangle composition plot confirms the material is located in the area associated with explosives, specifically identifying TNT in the result list. The yellow circles seen in the triangles labeled as "results" in the legend correspond to the uncertainty areas of the obtained result.

a) Material Profile

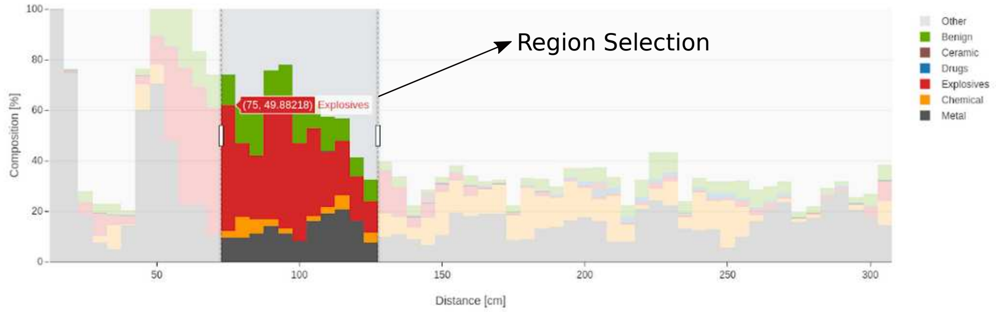

b) Elemental composition

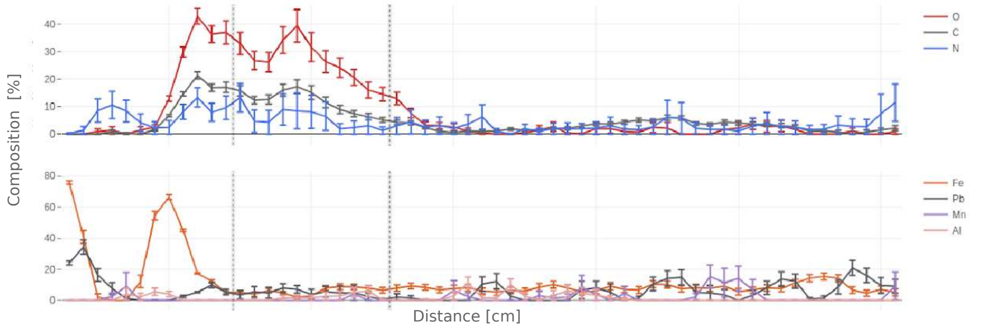

c) Radar composition Plots

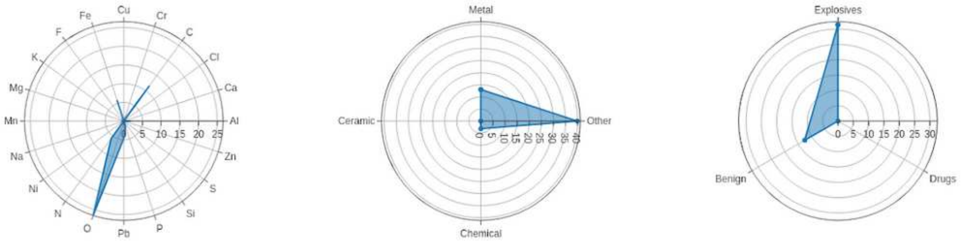

d) Triangle composition

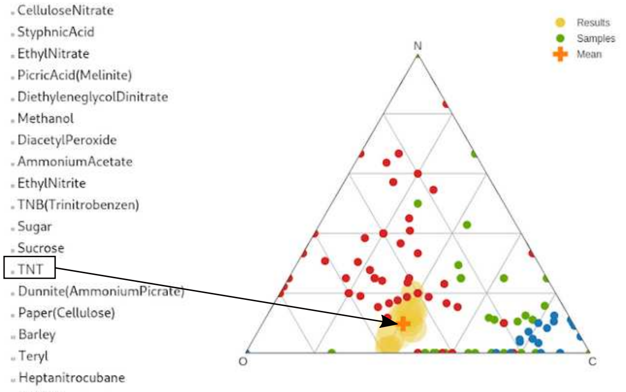

Figure 5.17: Material profile (a), count proportions attributed to each element (b), radar composition (c), and triangle composition (d) plots of Mock-up 5, with real explosive content (TNT + PENTRIT)

3. Mock-up 17 filled with illicit drug simulant (cocaine):

   A simulant of cocaine ($C_{17}H_{21}NO_4$) was hidden inside a mock-up container. The material profile indicated that the drug simulant was located just beyond the container wall (see Figure 5.18). A selection was performed around 100 cm, and the elements identified in the radar plot included oxygen, nitrogen, and carbon. Additionally, a significant amount of iron was detected, possibly indicating the presence of metal components near the drug material.

   In the radar plot used for organic material classification, the substance was mistakenly classified as benign. This error likely arose from the triangle composition plot (see Figure 5.18c), where the result and its uncertainty overlapped both the benign material region (green points) and the drug material region (blue points). The misclassification may have been caused by the similarity in composition between some benign materials, such as Nylon or Kevlar, and illicit drugs. These materials are rich in carbon and have a similarly low nitrogen fraction, placing them close together in the triangle plot.

   Although the list of potential organic materials included cocaine as a possible match, it's important to remember that decision-making relies on more than just this analysis. Other factors, such as intelligence reports, X-ray scans, and additional data, also play a key role. The RRTNIS results are just one part of the larger decision-making process.

a) Material Profile

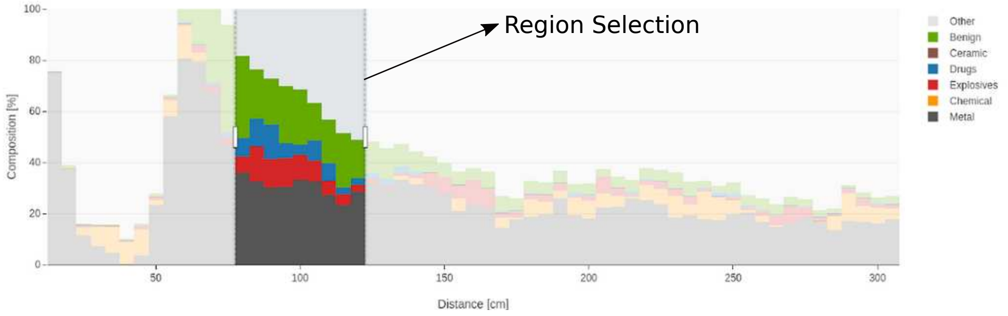

b) Radar composition Plots

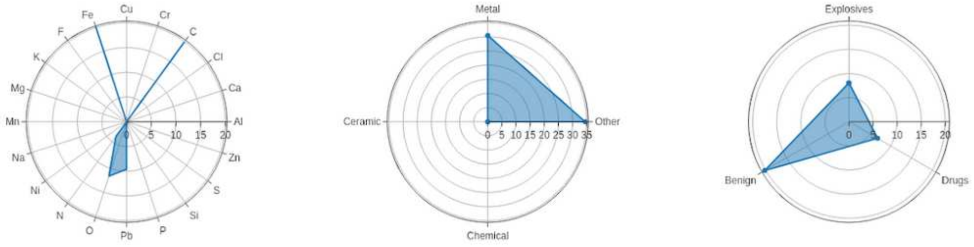

c) Triangle composition

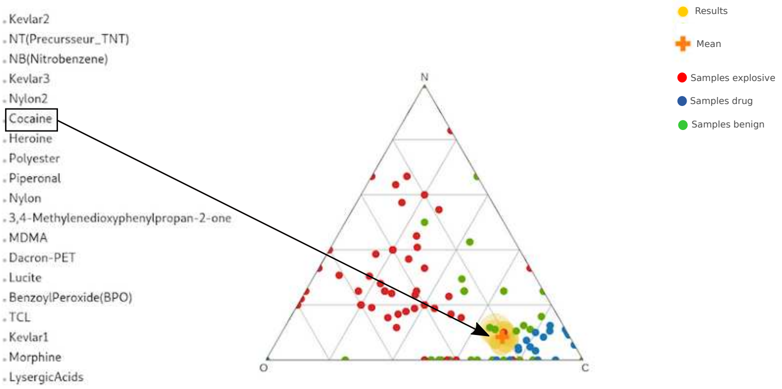

Figure 5.18: Material profile (a), radar composition (b), and triangle composition (c) plots of Mock-up 17, with illicit drug simulant

5.5.2 Commercial Containers

Various commercial containers declared as food cargo were analyzed at the Rijeka port using the TNIS system. The analysis included three containers loaded with bananas, one with pineapples, and another with tea leaves.

1. Commercial Container 15 with Pineapple Cargo:

   The results for the pineapple container are shown in Figure 5.19. The material profile indicates a predominance of benign material. The elemental composition plot reveals a high oxygen content, consistent with the high water content in pineapples, approximately 85%. Consequently, the triangle composition plot identifies the pineapple cargo as water.

a) Material Profile

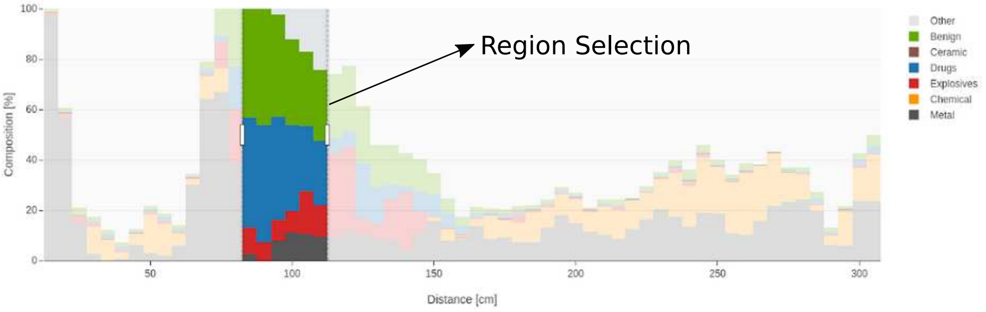

b) Elemental composition

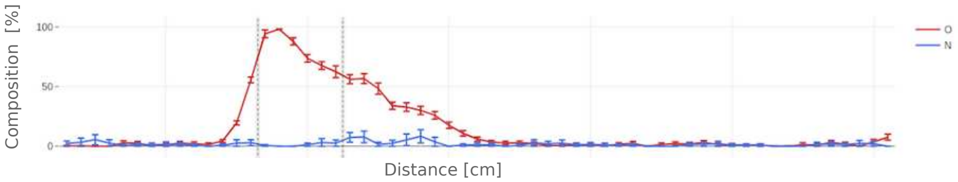

c) Triangle composition

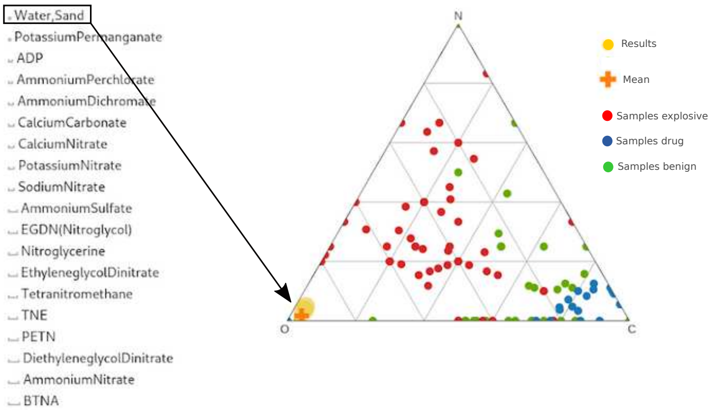

Figure 5.19: Material profile (a), count proportions attributed to each element (b), and triangle composition (c) plots of Commercial Container 15 with pineapple cargo

2. Commercial Container 17 Loaded with Iron Tubes:

   A commercial container declared to contain iron tubes was inspected. The results of the analysis are illustrated in Figure 5.20. The material profile clearly indicates a high metal content. The gamma-ray energy spectrum shows two photopeaks corresponding to iron, as shown in Figure 3.3. The elemental composition and radar plots reveal a significant presence of iron and lead, classifying the material as metal. The lead could be due to an alloy in the iron tubes. The TNIS system effectively identifies metal materials, leveraging the higher neutron inelastic cross-section of metals with 14 MeV neutrons, as explained in Subsection 3.3.1.

a) Material Profile

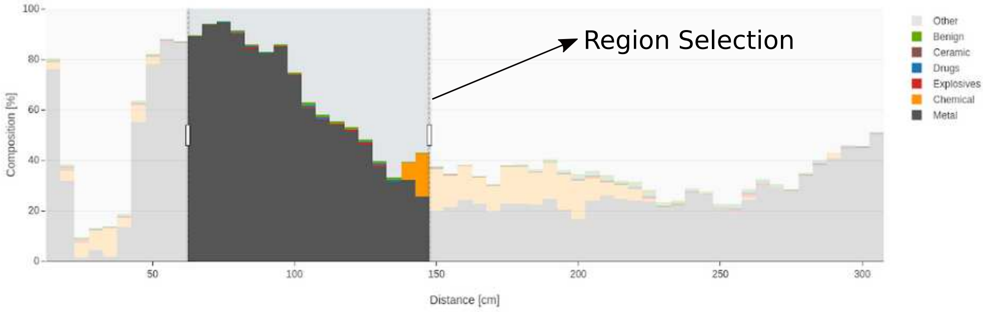

b) Gamma energy spectrum

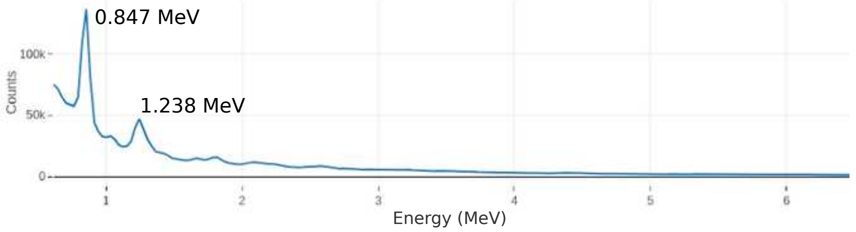

c) Elemental composition

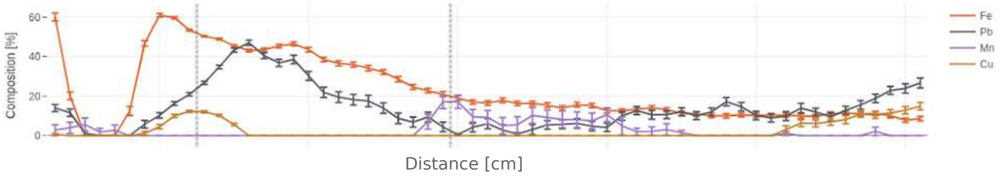

d) Radar composition Plots

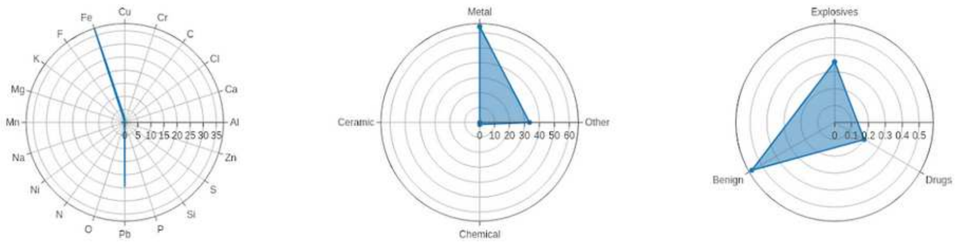

Figure 5.20: Material profile (a), gamma-ray energy spectrum (b), count proportions attributed to each element (c), and radar composition (d) plots of Commercial Container 17, loaded with iron tubes

5.6 Summary

This chapter detailed the field tests conducted using the RRTNIS system of the ENTRANCE project at the Port of Rijeka, Croatia, in May 2023. The objective was to assess the performance of the RRTNIS system in detecting hazardous materials. Over three weeks, 18 mock-up containers and 18 commercial containers were analyzed. The mock-up containers simulated various organic materials such as drugs (both simulants and real), explosives (both simulants and real), Teflon, sugar, salt (NaCl), sodium sulfide (NaS), fertilizer, flour, and tobacco. The commercial containers held diverse items, including PET material, electronic devices, bananas, tobacco, electronic cigarettes, wood, refrigerators, tubes, pineapples, household electronics, tea, plastic, screws, cartons, and shoes.

The identification of explosive materials showed promising results, but it's important to note that in a real blind test scenario, detection may have been more challenging. On the other hand, the success rate for cocaine identification was not optimal; moreover, some false alarm cases were identified. Misclassifications were primarily attributed to the overestimation of nitrogen content, with some benign materials being incorrectly identified as drugs for the same reason. The dominance of iron in the energy spectrum complicates the identification of organic materials. One potential solution is to use a higher energy threshold in the unfolding process to reduce contributions from iron and other background elements, thereby improving the detection of key elements like carbon, nitrogen, and oxygen.

Additionally, sulfur was sometimes misidentified as phosphorus due to similar gamma-ray spectra. This issue could be resolved by differentiating between the spectra more effectively, possibly by prioritizing other gamma-ray peaks with different energies. Further improvements in the algorithms, such as incorporating compound spectra instead of pure elements, could enhance material identification. For example, users could select the possible declared material before performing the analysis, and compound spectra, as glass or fertilizer could be used for unfolding, instead of elemental spectra.

Moreover, the k-nearest neighbors (kNN) algorithm used in the triangle identification could be improved by incorporating more samples and data for each sample to better capture the behavior of each organic material. Despite these areas for improvement, the overall experimental setup demonstrated stable performance and reliability. The RRTNIS system, along with the associated software and analysis techniques, proved effective in a real-world port setting. Ongoing enhancements to the data analysis, algorithms, and processing methods are recommended to further improve the accuracy and efficiency of the system.

Chapter 6

MULTISCAN 3D: Proof of Concept and Testing

In this chapter, a proof of concept is presented to investigate the use of the $^{9}Be(d,n)^{10}B$ nuclear reaction as an alternative neutron source for the MULTISCAN 3D project's neutron interrogation technique. This research was motivated by the need to replace the tritium-based reaction used in the ENTRANCE project, thereby avoiding the handling of tritium, a radioactive isotope with significant safety and logistical concerns. Furthermore, the $^{9}Be(d,n)^{10}B$ reaction provides a continuous neutron spectrum, which could excite states in the target materials with different probabilities compared to the 14 MeV monoenergetic beam used in the ENTRANCE project. The experimental investigation was conducted at the Van de Graaff CN accelerator at the INFN (National Institute of Nuclear Physics) in Legnaro, using a 4.7 MeV deuteron beam with a 50 nA current. Simulations were also conducted to estimate and compare the experimental results. Initial findings indicate the feasibility of the $^{9}Be(d,n)^{10}B$ reaction for neutron interrogation, showing promising gamma-ray spectra from materials like graphite, aluminum, iron, and copper.

6.1 Motivation

The MULTISCAN 3D project, as described in Subsection 2.2, aims to develop a static high-energy computed tomography system for inspecting cargo containers using radiation generated through an innovative laser-plasma-based technique. Additionally, the project explores the potential of producing other types of radiation, such as neutrons, leveraging this laser-plasma technology. The goal is to create comprehensive first- and second-line inspection systems for customs, incorporating 3D X-ray tomography, neutron and photofission interrogation techniques, and narrow gamma-ray beams based on Nuclear Resonance Fluorescence (NRF) [13].

As described in Subsection 3.4.1, the MULTISCAN 3D project generates high neutron fluxes using beam-target nuclear fusion. In this method, high-energy ions (such as deuterons) are employed in a "pitcher-catcher" setup: the first target, or "pitcher," is irradiated by a laser to produce light ions, which then travel to the second target, or "catcher," where they trigger fusion reactions [41].

The reaction used in the ENTRANCE project originates from the fusion reaction ^{2}H+^{3}H$\longrightarrow$n+α, which produces a monoenergetic beam of 14 MeV. This DT reaction can achieve high flux with low-energy acceleration; in this case, only 70 keV is used to accelerate deuterium (see Figure 3.7). Despite this reaction has shown optimal results for this specific application, the handling of tritium presents significant challenges. Therefore, alternative reactions can be explored to avoid the handling of tritium. Furthermore, given the advantages of laser-based accelerators in reaching high energies with compact devices, other nuclear reactions can be investigated, particularly for the MULTISCAN 3D project, which requires a compact and portable device. For instance, some of the most common reactions used for laser-based neutron sources, excluding the DT reaction, include D(D,n)^{3}He, ^{9}Be(d,n)^{10}B, ^{7}Li(d,n)^{8}Be, etc [42]. The total neutron yield curve for some of these reactions can be seen in Figure 3.7. From the reactions depicted in Figure 3.7, the neutron yield from the lithium and beryllium targets is significantly higher compared to the DD or DT reactions when the deuteron energy exceeds 1.5 MeV, an energy that can be achieved over a short distance using laser-based accelerators.

Both reactions using beryllium and lithium targets could be valuable for neutron interrogation techniques, as they emit a continuous neutron spectrum ranging from approximately 0 to 20 MeV. This spectrum enables the excitation of interrogated materials across various neutron energies, allowing access to a different range of excitation states or intensity ratios compared to a 14 MeV monoenergetic beam. This aspect could be an interesting area for further study to determine whether these differences enhance the interrogation capabilities of the system.

In particular, this work explores a proof-of-concept experiment to assess the feasibility of neutron interrogation techniques for identifying organic or inorganic materials, using the ^{9}Be(d,n)^{10}B reaction at the Van de Graaff CN accelerator at the INFN in Legnaro. This facility offers several beamlines for accelerator-driven neutron production with precisely defined primary beam current, size, and energy. The aim is to study material identification using neutron interrogation techniques with the proposed nuclear reaction, producing neutron energy spectra similar to those that can be generated using laser-plasma technology. This proof-of-concept experiment will provide experimental validation for ongoing neutron laser source studies, suggesting the optimal neutron energy range and intensity, which will inform the choice of secondary target (beryllium) for the laser-based neutron source.

The experiment involves using the neutron flux produced by the previously mentioned reactions to induce neutron inelastic scattering reactions (n,n'γ) in various nuclei of interest. This includes nuclei of organic and inorganic materials, such as C, N, O, Fe, Al, Cu, etc. Given the energy spectrum of the produced neutrons, inelastic scattering reactions are likely to occur, resulting in gamma-ray emissions due to de-excitation. Material identification is achieved by measuring and analyzing the energy spectrum of these gamma rays, and in this way the elemental composition of the the interrogated material can be obtained.

Another important aspect of this research is that comprehensive measurements of (n,n'γ) reactions on stable materials for incident neutron energies ranging from a few MeV up to 20 MeV are beneficial, considering that neutron-in and gamma-ray-out data, particularly for thick samples, are limited and primarily involve only 14 MeV neutrons.

6.2 Preliminary Simulations

As explained in the Motivation (Section 6.1), nuclear reactions using beryllium or lithium targets could provide an alternative to the DT reaction, thus avoiding the handling of tritium. To explore this possibility, preliminary simulations were performed to compare the resulting gamma energy spectra. These simulations were conducted using Geant4 v10.7.

First, neutron energy spectra for the ^{9}Be(d,n)^{10}B and ^{7}Li(d,n)^{8}Be reactions were obtained by directing 1×10^{8} ions of deuterium onto the targets, with energies of 4.7 MeV for beryllium and 1 MeV for lithium. The lithium target at 1 MeV yielded three monoenergetic neutron peaks with energies and intensities of 4.4 MeV (48.42%), 12.3 MeV (41.05%), and 15.2 MeV (10.52%). For the beryllium target, a deuteron energy of 4.7 MeV was used, to produce a neutron spectrum reaching up to 9 MeV with an increased yield of neutrons in the 5–8 MeV range, compared to lower deuteron energies, as shown in Figure 6.1. At these energies, elements of interest for interrogation, as shown in Figure 3.2, exhibit higher cross-sections for inelastic neutron scattering interactions.

The simulations also considered deuteron energies up to a maximum of 5 MeV, reflecting the highest acceleration energy achievable with the CN accelerator.

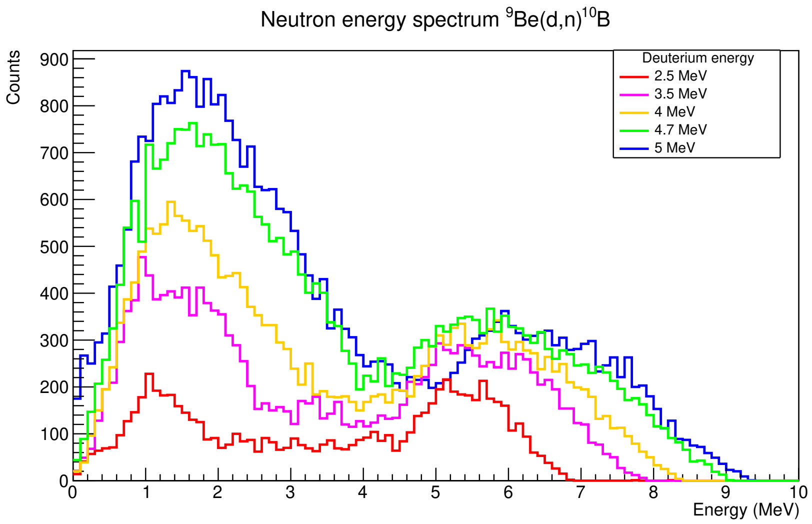

Figure 6.1: Simulated neutron energy spectra coming from the ^{9}Be(d,n)^{10}B reaction, with different deuteron energy

The subsequent simulations involved impacting 1×10^8 neutrons corresponding to the two neutron energy spectra determined for the lithium and beryllium targets, as well as a monoenergetic beam of 14 MeV corresponding to the DT reaction, against cubic targets of carbon (graphite), oxygen (water), nitrogen (liquid nitrogen), lead, copper, iron and aluminium, each with a volume of 1 cm^3. The gamma rays emitted after the interaction of the neutrons with the materials were recorded, and the results can be seen in Figures 6.2 and 6.3.

From the obtained results in Figure 6.2, the DT reaction shows the highest number of counts in the main peaks for each target: 4.4 MeV for the carbon target, 1.63 MeV, 2.3 MeV, 4.42 MeV and 6.44 MeV for the nitrogen target, and 6.049 MeV and 7.115 MeV for the oxygen target. The lithium target also exhibits a significant number of counts, showing at least more than half the counts obtained with the DT reaction. It is noteworthy that for deuteron energies above 2 MeV, the neutron yield from the lithium reaction tends to increase relative to the DT reaction, as shown in Figure 3.7. Thus, with a deuteron energy of 2 MeV, a higher neutron rate is obtained and in consequence, a greater number of counts compared to the DT reaction can be achieved.

In the case of the oxygen target, a prominent peak at 2.2 MeV is observed when using the beryllium reaction. This peak corresponds to the excitation of hydrogen when a thermal neutron is captured in the water target. This phenomenon is more frequently observed with the beryllium reaction because the lower neutron energies can be thermalized more rapidly and easily within the water target, leading to capture by hydrogen nuclei. Moreover, as shown in Figure 6.2, the intensity ratios of the gamma-ray peaks vary for each nuclear reaction under study, which is expected since the probability of exciting a given state changes with neutron energy. Thus, even though the count rate is lower with the lithium and beryllium targets compared to the DT reaction, it could be interesting in the future to investigate whether these differences in the intensity ratios of the gamma-ray peak could be beneficial for element identification.

The beryllium reaction demonstrated approximately 1/5 of the counts obtained with the DT reaction for the carbon, nitrogen, and oxygen targets. However, for metal elements, the performance differs, as shown in Figure 6.3. The neutron spectra produced by the lithium and beryllium reactions are more suitable for identifying metal elements, as expected from their cross sections (see Figure 3.2). For neutron energies around 5 and 8 MeV, the cross sections for metal elements are greater compared to a neutron energy of 14 MeV. This is reflected in the results in Figure 6.3, where most of the main gamma peaks for each target material have higher counts with the lithium and beryllium reaction than with the DT reaction, as for example, the 1.179 MeV peak for copper, the 1.014 and 2.211 MeV peaks for aluminum, the 2.6 MeV peak for lead and the 0.846 MeV for iron.

Despite the lithium target showed favorable results for both metal and non-metal elements, only the beryllium target was tested at the CN accelerator, as an appropriately thick lithium target was unavailable. Tests with a lithium target is planned for future experiments.

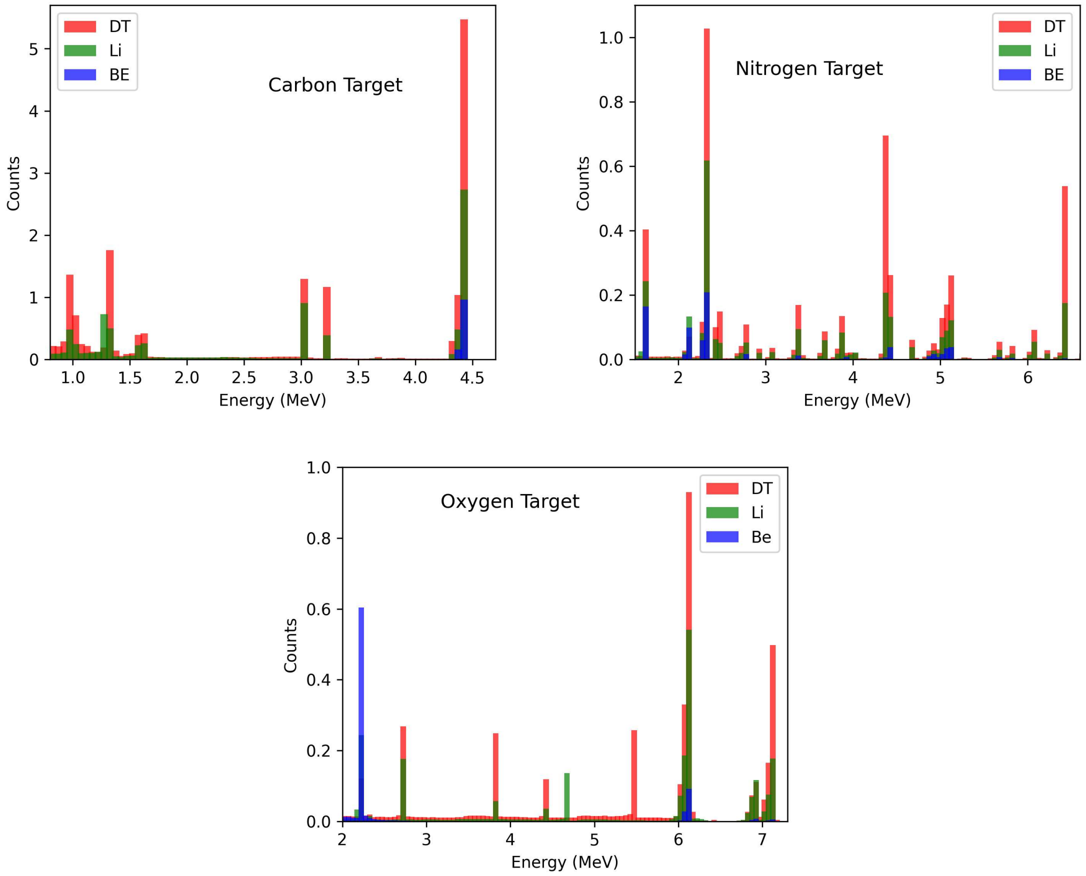

Figure 6.2: Simulated gamma spectra from a C, N and O target using neutron energy spectra from the ^{3}H(d,n)^{4}He, ^{9}Be(d,n)^{10}B, and ^{7}Li(d,n)^{8}Be reactions (1x10^{8} events)

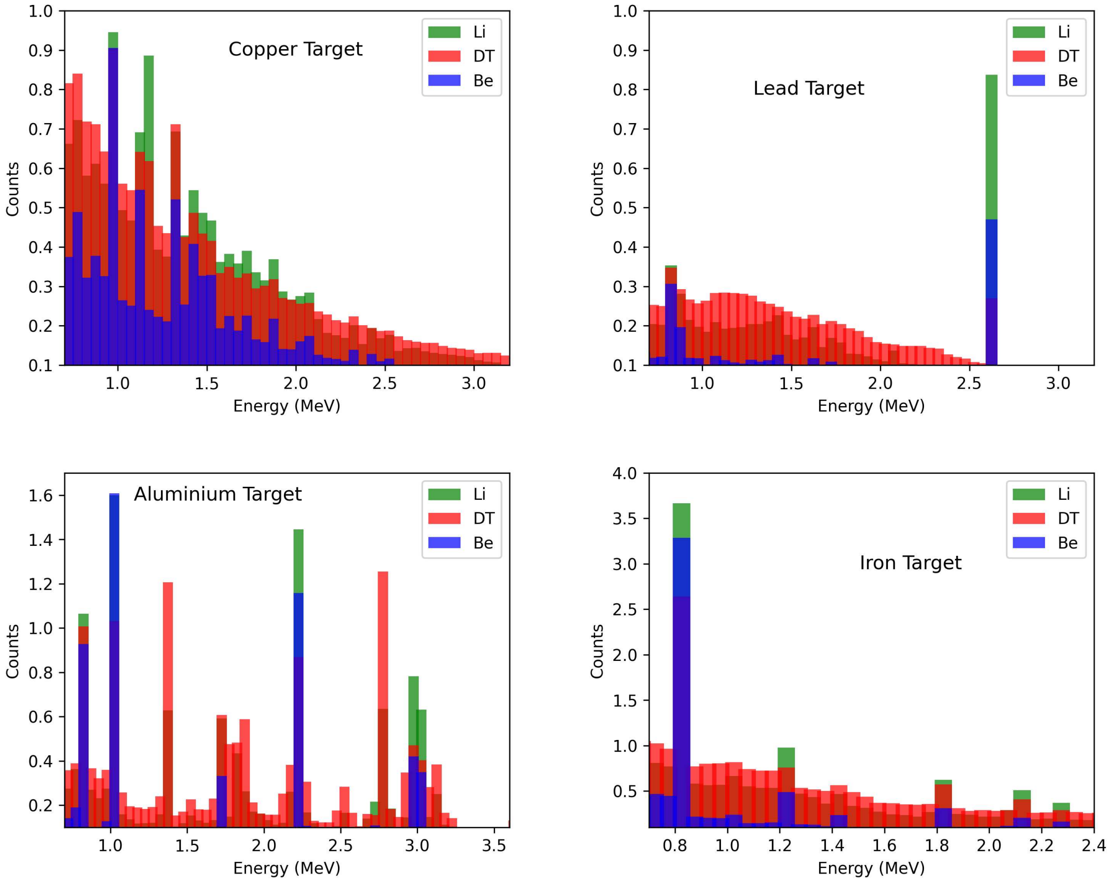

Figure 6.3: Simulated gamma spectra from a Cu, Al, Pb and Fe target using neutron energy spectra from the ^{3}H(d,n)^{4}He, ^{9}Be(d,n)^{10}B, and ^{7}Li(d,n)^{8}Be reactions (1x10^{8} events)

6.3 Simulation Resembling the Experiment at the CN

To make a realistic comparison between the simulations and the experimental results, a detailed simulation of the experimental configuration was implemented using the Geant4 v10.7 toolkit. In this case, the continuous neutron spectrum obtained from the ^{9}Be(d,n)^{10}B reaction with a deuterium energy of 4.7 MeV was used (see Figure 6.1). To replicate the conditions of the experimental setup, a 3" × 3" LaBr$_3$:Ce inorganic scintillator was constructed, and all gamma rays reaching this volume were recorded, thereby obtaining the gamma energy spectra from the different target materials. In each simulation, 1×10^{6} events were simulated. The interrogated materials had dimensions of 35 × 28 × 17 cm^{3} (whereas in the experimental setup, most of the materials measured approximately $30 \times 30 \times 20$ cm^{3}). The materials studied included lead, water, liquid nitrogen, aluminum, carbon, copper, and iron.

In Figures 6.4 and 6.5, the results show the simulated gamma energy spectra from the various target materials under study, detected with the LaBr$_3$:Ce detector, using the neutron energy spectra generated by 4.7 MeV deuterons. And as it was previously mentioned in some materials, the most prominent peaks in the gamma spectra differ from those obtained in simulations using a monoenergetic neutron beam of 14 MeV (as seen in Figure 4.9). This discrepancy arises from the new neutron energy spectrum used, which has distributed energies lower than 9 MeV, thus exciting states with different probabilities. For instance, in the case of nitrogen, the DT reaction indicated some of the main peaks at 6.44 MeV (as can be seen in Figures 4.9 and 6.2), while with the beryllium simulation, this peak does not appear; instead, one of the most prominent peaks is at 5.104 MeV. Additionally, in the monoenergetic beam case, the 2.312 MeV peak had a significantly higher intensity compared to the 1.63 MeV peak, but with the continuous spectrum, both peaks have nearly the same intensities, as expected in the intensity ratios seen in the nitrogen target in Figure 6.2.

As mentioned previously (Subsection 6.1), an interesting fact behind this proof of concept is to access these diverse excitation states with different probabilities compared to those observed at 14 MeV. It is important to note that in the spectra shown in Figures 6.4 and 6.5, the 2.2 MeV peak corresponding to the radioactive capture reactions on H nuclei is not observed due to a time-of-flight (ToF) window applied to the data.

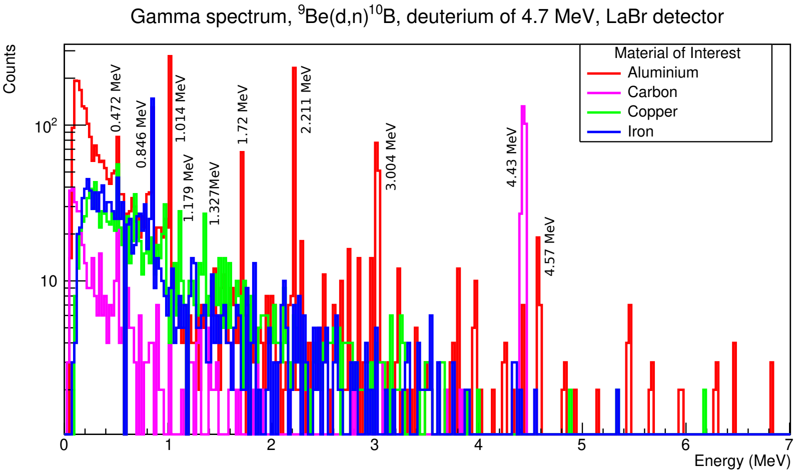

Figure 6.4: Simulated gamma energy spectra coming from different target materials, detected with the LaBr$_3$:Ce detector, using the neutron energy spectra from the ^{9}Be(d,n)^{10}B reaction, with 4.7 MeV of deuteron. Simulation performed with 1x10^{6} events.

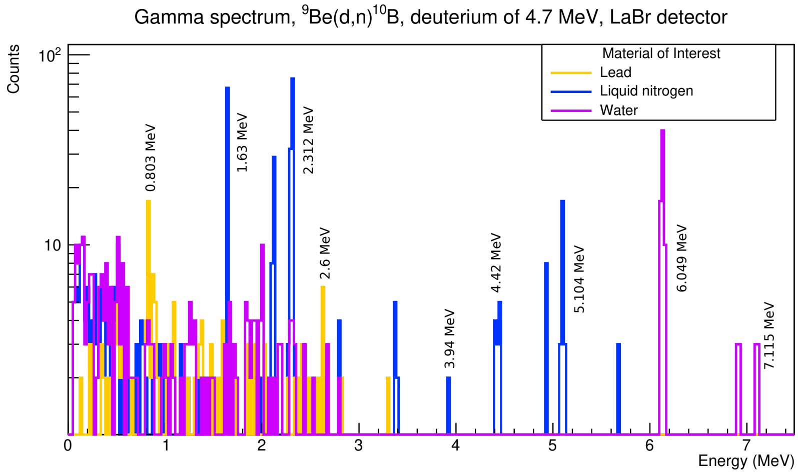

Figure 6.5: Simulated gamma energy spectra coming from different target materials, detected with a the LaBr$_3$:Ce detector, using the neutron energy spectra from the ^{9}Be(d,n)^{10}B reaction, with 4.7 MeV of deuteron. Simulation performed with 1x10^{6} events.

6.4 Experimental description

The experimental shift lasted 3 days at the 0° beam line of the CN accelerator, with a nanosecond pulsed (3 MHz) deuteron beam (^{2}H^{+}) with an energy of 4.7 MeV (considering that 5.5 MeV is the maximum possible energy that ions can reach in the CN accelerator) and a current of 50 nA. The experiment used a ^{9}Be target, where neutrons were emitted with energies of approximately 10 MeV, in the same direction as the deuteron beam. The pulsed beam is necessary to trigger the acquisition with the pick-up signal, allowing us to filter the data to be acquired online and to perform Time-of-Flight (ToF) spectra (see Subsection 3.3.1). From the ToF spectra, the yield of the gamma-ray emission can be assessed as a function of the neutron energy. This takes into account that the speed of the neutrons depends on their energies, so by measuring the travel time from a known distance, the energy can be determined (see Subsection 6.4.2).

Firstly, the experiment consists of performing characterization measurements of the neutron flux produced (in terms of energy and intensity). This is done with a liquid scintillator cell, 2”x2” EJ-301 from Eljen Technology-Texas US, which is a standard fast neutron detector. The detector is settled in coincidence with the pick-up of the accelerator to obtain the ToF, which then provides the neutron spectrum. The detector is placed where the sample is expected to be located (around 90 cm from the target), a distance optimized to balance good energy resolution from the Time-of-Flight spectrum and a good counting rate.

The second step involves exposing different mono-element and compound materials to the neutron field and measuring the gamma-ray emissions. Specifically, the samples under interrogation were copper, iron, aluminum, lead, melamine, water, and graphite.

For each sample, the measurement time ranged from 20 to 30 minutes, as estimated in Subsection 6.4.1. The gamma-rays were detected using a 3"x3" $LaBr_3$:Ce inorganic scintillator from Luxium Solutions, in coincidence with the pick-up as a starting point. The $LaBr_3$:Ce detector was placed laterally and shielded with 10 cm of polyethylene (PE), 10 cm of lead, and a blanket made of boron to capture the thermal neutrons produced in the process and prevent detector activation. For better comprehension, a schematic view and a picture of the experimental setup are provided in Figure 6.6 and Figure 6.7.

The detectors were powered using a CAEN power supply (V6533 model), controlled by a CAEN V1718 USB Controller. The output signals were digitized by a fast CAEN digitizer model V1730, which has a sampling rate of 500 MSamples/s and an ADC resolution of 14-bit. The digitizer was controlled by a CAEN A3818 PCI Express CONET2 Controller installed on the PC, using optical fiber connections and the CAEN CONET2 protocol. The installed firmware on the digitizer performs charge integration and timing analysis (Digital Constant Fraction Discriminator) of each acquired signal, allowing the construction of energy and time spectra associated with each detector. The ABCD (Acquisition and Broadcast of Collected Data) software was used to handle all aspects of the electronics and data acquisition [50,57]. Specifically, for the coincidence between the detectors and the pick-up, the WAAN library from ABCD was used to apply the DCFD, considering that the pick-up signal is a fast bipolar signal, which cannot be processed correctly using the coincidence mode of the CAEN digitizer.

It is important to note that beryllium dust can be toxic. However, in this case, where the target dimensions were approximately 1.5 cm x 1.5 cm with a thickness of 60 μm, the likelihood of target degradation or dust generation, even after irradiation, is extremely low. During installation, the accelerator personnel took minimal precautions, using only gloves to handle the target. Additional protective measures were not deemed necessary. Therefore, considering the proposal to house the target within a portable and compact laser-based accelerator, the risk of toxicity can be considered negligible.

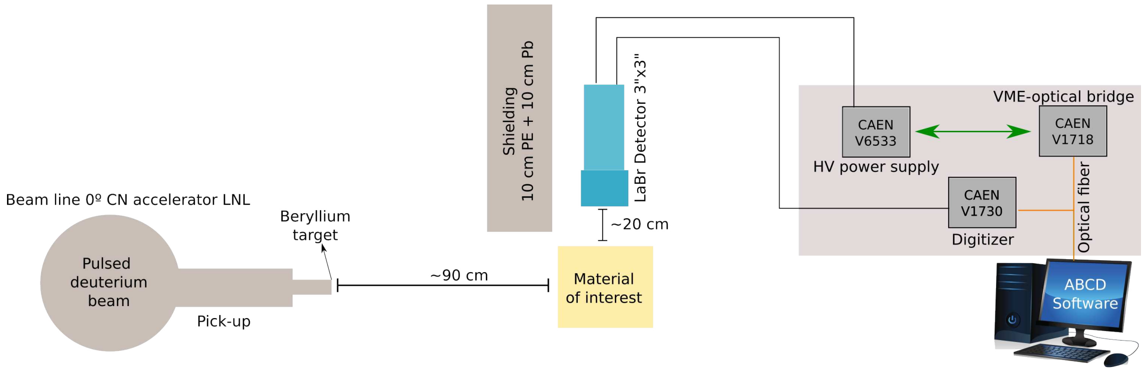

Figure 6.6: Schematic view of the experimental setup.

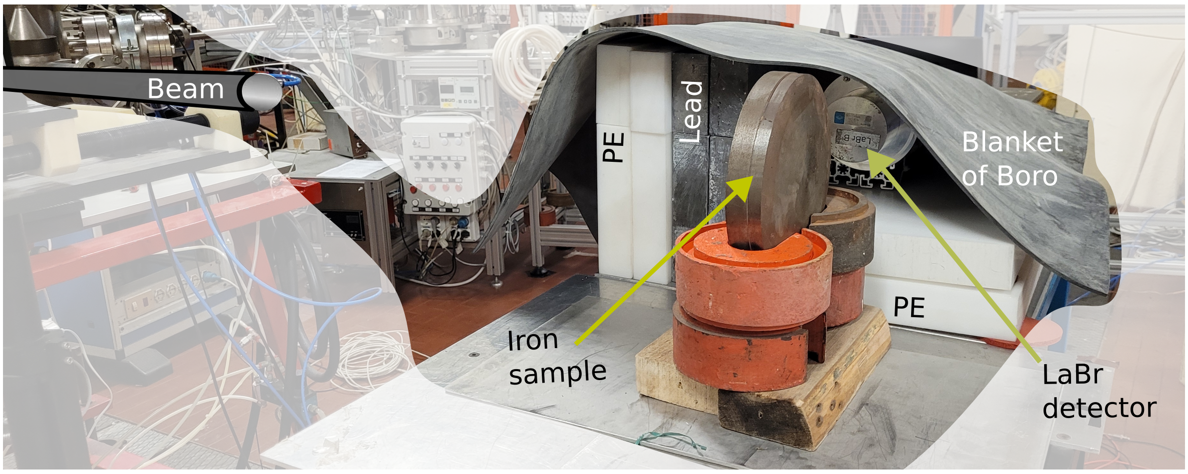

Figure 6.7: Picture of the experimental setup, with the iron sample.

6.4.1 Measurement time estimation

For each sample, the measurement time is between 20 minutes and 30 minutes. Taking into account the following calculation for the reaction: ^{9}Be(d,n)^{10}B, the neutron yield is almost: 5×10^{9} s^{-1} · μA^{-1} (see Figure 3.7). As the current is around 50 nA, the neutron emission rate will be equal to 2.5×10^{8} s^{-1}.

Assuming that the material of interest will be a block of graphite with dimensions equal to $10 \times 10 \times 10\,\text{cm}^3$ (one liter), and it will be placed at 90 cm from the target, the neutron flux that will reach the material will be:

$$\phi = \frac{S}{4\pi r^2} = 2.5 \times 10^3 \text{ s}^{-1}.\ \text{cm}^{-2}$$

where S is the neutron source rate and r is the distance.

Considering that the total number of atoms in the block is:

$$N = \frac{N_A \cdot \rho \cdot V}{A} \sim 10^{26} \text{ atoms of } {}^{12}\text{C}$$

and the neutron inelastic scattering cross-section on ^{12}C for neutrons with energy around 9 MeV is: $\sigma(n, n') \sim 0.3$ b. The reaction rate on the material will be:

$$R = \phi \cdot \sigma \cdot N \sim 7.5 \times 10^4\,\text{s}^{-1}$$

Finally, the expected counting rate will be approximately 750 cps (with our experimental setup, we predict that the gamma detector array will have a total detection efficiency of around 1%). Therefore, sufficient statistics can be achieved for measurement times between 20 minutes and 30 minutes.

6.4.2 Determination of Neutron Energy Spectra from the ToF Spectrum

The time-of-flight (ToF) technique is a widely used method to determine the energy of neutrons. Neutrons with different energies travel at different speeds, and by measuring the time it takes for neutrons to travel a known distance, their energy can be calculated using the following equation:

$$E = \frac{m}{2}\left(\frac{L}{t}\right)^2$$

where:

- E is the neutron energy (in electronvolts, eV)
- m is the neutron mass (1.675×10^{-27} kg)
- L is the distance between the neutron source and the detector (in meters, m)
- t is the time of flight (in seconds, s)

This equation is derived from the kinetic energy formula $E = \frac{1}{2}mv^2$, where v is the velocity of the neutron. By substituting $v = \frac{L}{t}$ (velocity as distance divided by time) into the kinetic energy formula, it is possible to obtain the equation above for neutron energy.

To make use of this equation, it is necessary to measure the ToF (t) of the neutron and the distance (L) between the neutron source and the detector. Once these values are known, it is possible to calculate the neutron energy (E) by plugging them into the equation.

It is worth noting that this equation assumes non-relativistic velocities of neutrons. This assumption is valid for most practical purposes in neutron spectroscopy, where neutron speeds are significantly lower than the speed of light.

6.5 Results and analysis

As a first step, as explained previously in Subsection 6.4, characterization measurements of the neutron flux produced in the accelerator were performed. This was done using an EJ-301 liquid scintillator cell, set up in coincidence with the pick-up of the accelerator, allowing for the calculation of the ToF spectrum. The liquid scintillator was positioned 90 cm from the beam target.

In Figure 6.8, the 2D-PSD plot obtained from this measurement is shown (see Subsection 3.2 for a detailed explanation of the PSD technique). Thanks to the pulse shape discrimination and the capabilities of the liquid scintillator, it is possible to distinguish in Figure 6.8 the events corresponding to neutrons from those corresponding to gamma-rays.

The ToF spectrum is then plotted, with neutron events highlighted in pink in Figure 6.8. These neutron events were previously selected within the red boundary in the 2D-PSD plot. From this ToF spectrum, corresponding specifically to the neutron events, the energy spectrum of the emitted neutrons is built by performing the calculations described in Subsection 6.4.2. The resulting energy spectrum is shown in Figure 6.9. The neutron energy spectrum is normalized to the neutron detection efficiency of the detector as a function of the neutron energies, with efficiency values obtained from [58].

The distribution of the energy spectra between the simulation and experimental results shows different behaviors, as seen in Figure 6.1 and Figure 6.9. In the higher energy range of neutrons (between 5 and 9 MeV), the experimental spectrum has a much lower intensity compared to the lower energy range. This discrepancy is likely because, in the experimental case, scattered neutrons are measured, contributing more to the lower energy range. In contrast, the simulations do not account for scattered neutrons, resulting in a higher detection rate of neutrons with higher energies.

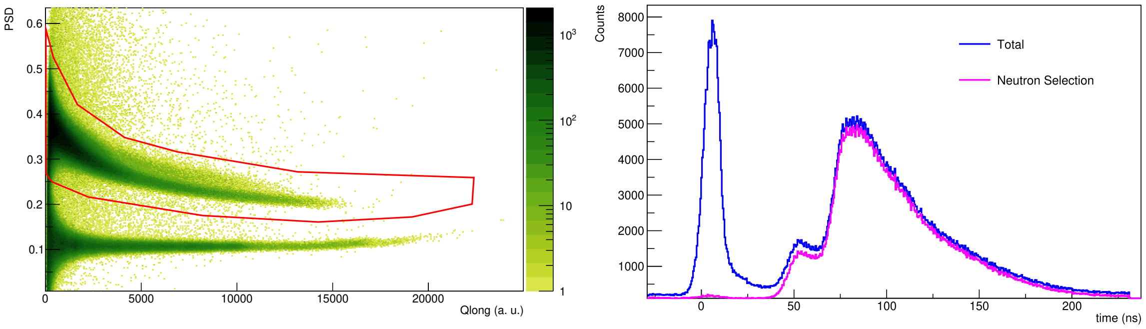

Figure 6.8: 2D-PSD plot (in red zone the fast neutron selection) and ToF spectrum using the EJ-301, corresponding to coincidence measurement using the ^{9}Be(d,n)^{10}B reaction at the CN accelerator, with 4.7 MeV of deuterium.

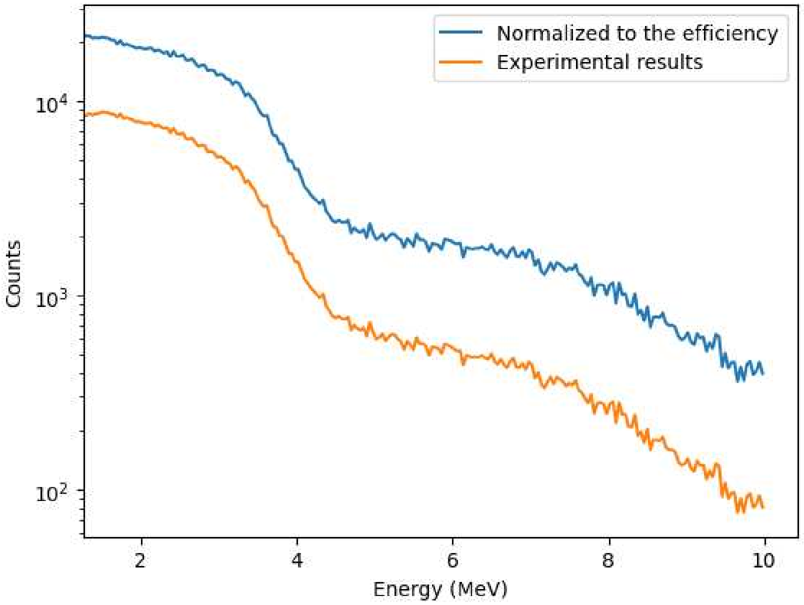

Figure 6.9: Energy spectrum obtained with the ^{9}Be(d,n)^{10}B reaction at the CN accelerator, with 4.7 MeV of deuterium, showing also the normalized spectrum with respect to the efficiency of the EJ-301 detector.

Moreover, the neutron rate at the emission point was determined experimentally by counting the number of neutrons detected with the liquid scintillator in "single mode" (total count rate, without a coincidence window). This value was then re-scaled to the distance from the beam origin. Assuming the neutrons are emitted isotropically over 2π steradians, the obtained value is $5\text{x}10^8$ s^{-1}, which is close to the theoretical value of $2.5\text{x}10^8$ s^{-1} calculated in Subsection 6.4.1. The discrepancy may be because we do not precisely know the solid angle of neutron emission; we are assuming a hemispherical isotropic emission. Additionally, the current report given by the technicians may not be entirely accurate, contributing to some uncertainty.

After characterizing the neutron flux, various measurements were performed by placing different types of materials (copper, iron, aluminum, lead, melamine, water, and graphite) in front of the neutron beam in order to apply the neutron interrogation technique, as explained in Subsection 6.4. The gamma-ray spectra obtained using the LaBr$_3$:Ce detector for some of the samples (graphite, aluminum, copper, and iron) can be seen in Figure 6.10. The spectra clearly show the 4.4 MeV characteristic peak of carbon in the graphite sample and its first escape peak at 3.9 MeV. The copper sample shows distinct characteristic peaks, notably the intense peak at 0.96 MeV, and less intense peaks at 1.11 MeV and 1.32 MeV, in contrast to what was seen in the simulation results (see Figure 6.4). This outcome is expected since, experimentally, fewer high-energy neutrons are emitted. Similarly, in the aluminum sample, the 1.104 MeV peak is more intense than in the simulation, while peaks higher than 1.5 MeV are less intense but still identifiable, such as the 1.72, 2.21, and 2.98 MeV photopeaks. Finally, the 0.84 MeV peak of iron is clearly identified.

However, the main peaks for the other three samples lead, melamine, and water could not be identified. This could be because lead's cross-section for inelastic neutron scattering becomes significant only above 4 MeV (see Figure 3.2), and the number of neutrons with energies higher than 4 MeV was very low. Similarly, the oxygen in water could not be identified because its cross-section becomes prominent only above 7.5 MeV. For melamine, even though nitrogen starts interacting with neutrons at energies lower than 5 MeV (see Figure 3.2), the peaks were likely not visible due to the small amount of melamine irradiated.

From the obtained results, it can be concluded that a very small proportion of neutrons with energies higher than 4 MeV were generated. This is evident from the gamma energy spectra, where all observed peaks (see Figure 6.10) have energies below 4 MeV, except for the graphite sample's intense peak at 4.4 MeV, which was likely due to the large amount of graphite used in the measurement.

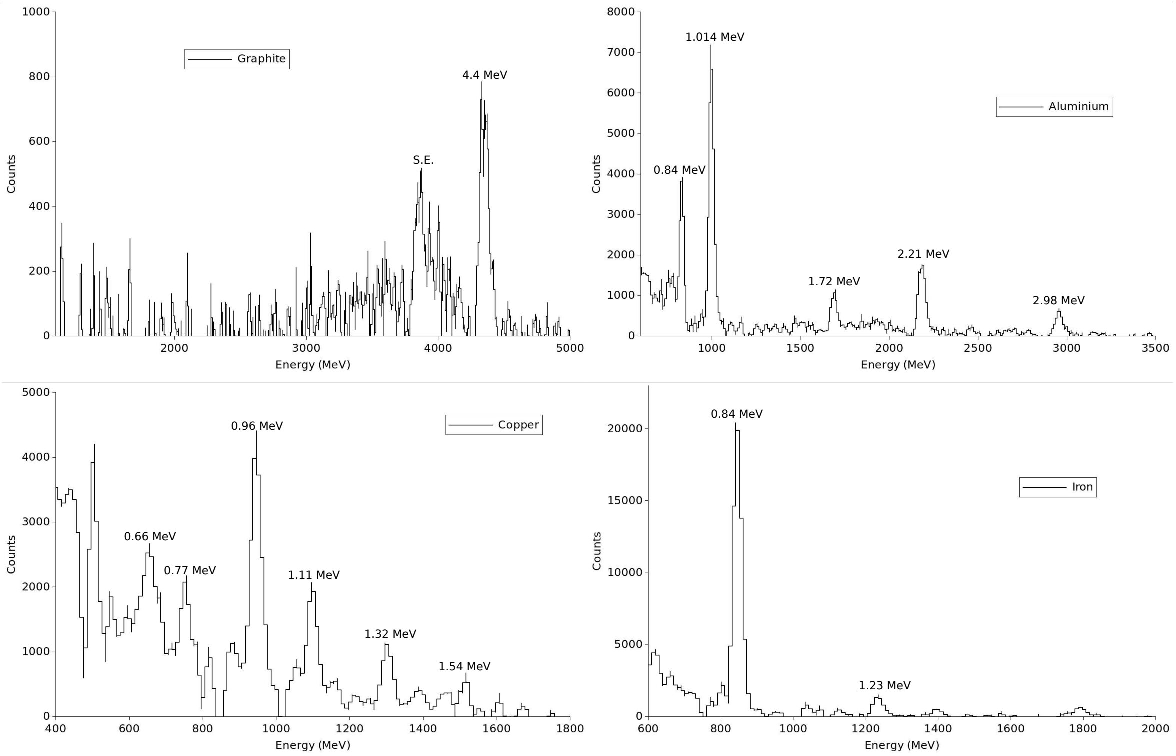

Figure 6.10: Gamma energy spectra coming from different materials interrogated (graphite, aluminum, copper and iron), detected with the $LaBr_3$:Ce detector, using the neutron energy spectra from the $^9Be(d,n)^{10}B$ reaction, with 4.7 MeV of deuteron.

6.6 Summary

This chapter presents a proof-of-concept experiment to investigate the feasibility of using the ^{9}Be(d,n)^{10}B nuclear reaction for generating the neutron source needed in the MULTISCAN 3D project for neutron interrogation techniques, as an alternative to the reaction currently employed in the ENTRANCE project. The motivation behind this research is to avoid the handling of tritium, a radioactive isotope associated with significant safety and logistical challenges. Moreover, using a laser-driven accelerator makes it possible to accelerate deuterons to high energies over very short distances, which is necessary for initiating the proposed beryllium reaction.

The experiment, was conducted over a three day shift using the 0° beam line of the CN accelerator, it involved producing neutron flux with a ^{9}Be target and a 4.7 MeV deuteron beam. Neutron energy and intensity were characterized using an EJ-301 liquid scintillator detector, and ToF measurements helped to determine the neutron energy spectra. Various materials, including copper, iron, aluminum, lead, melamine, water, and graphite, were exposed to the neutron beam, and their gamma-ray emissions were measured using a $LaBr_3$:Ce scintillator detector.

Experimental measurements were complemented by simulations to predict outcomes and validate results. Discrepancies between the experimental neutron energy spectra and simulations were identified, particularly in the higher energy range, likely due to unaccounted neutron scattering effects. Despite this, the neutron rate at the emission point was close to theoretical predictions. Gamma-ray spectra from the experimental setup successfully identified characteristic peaks for materials like graphite, copper, aluminum, and iron, at least validating the feasibility of the ^{9}Be(d,n)^{10}B reaction for neutron interrogation on metal materials.

From this initial test, we conclude that the tested nuclear reaction ^{9}Be(d,n)^{10}B could serve as an alternative to the DT reaction for the neutron source needed in the neutron interrogation technique of the MULTISCAN 3D project, in particular for interrogating inorganic materials. Further exploration of this reaction can be conducted by increasing the deuteron energy to up to 5.5 MeV, which is feasible at the CN accelerator. This adjustment would result in the generation of neutrons with higher energies. Additionally, to explore alternatives to the DT reaction, as mentioned earlier, it would be beneficial to conduct tests with a lithium target (^{7}Li(d,n)^{8}Be). As simulated in this work, this reaction produces higher neutron energies compared to the beryllium reaction, resulting in an increased probability of identifying both organic and inorganic materials.

It is also important to note that a challenging task in the future could be converting the measured ToF into a distance to localize the element being interrogated inside the container. While measuring the ToF (or the alpha-gamma coincidence time in the RRTNIS) is feasible, the difficulty lies in accurately translating this ToF into a distance. This process is straightforward with a monoenergetic neutron beam, where all emitted neutrons travel at the same velocity. However, in the reaction under study, a continuous neutron spectrum is emitted, resulting in a range of neutron velocities, making the conversion from ToF to distance a challenging task. This objective is beyond the scope of this proof-of-concept experiment, but it could be addressed in the future with specific analytical or experimental techniques. For example, it could be approached as done in the work by [59], which characterized continuous neutron spectrum fluxes (10 keV - 20 MeV and 10 meV - 1 MeV) for ToF measurements. This study was performed through Monte Carlo simulations using the MCNP5 code and characterized the neutron fluxes in terms of energy spectra and ToF spectra for 18 flight paths at different angles.

It is important to remark that the MULTISCAN 3D project also includes the objective of identifying special nuclear materials (SNM) using a thermal neutron beam. The use of a beryllium target could be beneficial in various aspects compared to the monoenergetic beam of 14 MeV. For instance, since the continuous neutron spectrum has lower energy compared to 14 MeV, the thermalization of the neutrons could be performed easier and faster. Moreover, as seen in Figure 3.7, when the deuteron energy exceeds 2 MeV, a higher neutron flux is observed for the lithium and beryllium targets compared to the DT reaction. This is particularly important, as a high neutron rate is needed for this type of interrogation.

Chapter 7

Characterization of two innovative detection systems for the photofission system

This study introduces an innovative detection system for identifying SNM (Special Nuclear Materials) in the ENTRANCE and MULTISCAN 3D projects. The proposed system features a flexible fully enriched Lithium Tetraborate ($^6Li_2{}^{10}B_4O_7$) *thermal neutron scintillator and a compact gamma-ray detection unit using an organic scintillator coupled to a SiPM array. The ZnS:Ag/LiBO/PDMS (polydimethylsiloxane) neutron detector demonstrated good thermal neutron efficiency (up to 57% with respect to the EJ-420, which is a commercial neutron detector with 95% (* ^6Li *content dispersed in a ZnS:(Ag) matrix), excellent flexibility, and superior gamma-ray rejection (GRR below* 9×10^{-11}*), making it a viable alternative to* ^3He *detectors. For gamma-ray detection, configurations of EJ-276G and EJ-309 organic scintillators coupled with AdvanSiD, Hamamatsu, and Ketek SiPM arrays were tested. The Hamamatsu array showed the best overall performance in energy resolution (10%), time resolution (0.52 ns), and neutron/gamma-ray discrimination (FoM=2). However, the Ketek array outperformed others when normalized to the number of photoelectrons. This research advances SNM detection technology by providing a compact, low-power system with precise discrimination capabilities, supporting the development of advanced photofission systems. Both characterization studies have already been published in scientific journals [60, 61]*

7.1 Motivation

In the ENTRANCE and MULTISCAN 3D projects, the photofission interrogation technique is applied to identify the illegal transportation of SNM inside containers, functioning as a second-line technology. High-energy photons are directed at the suspected area of the container, inducing fission in actinides. During this process, the nuclei of the actinides undergo fission, emitting two fission products along with prompt neutrons and gamma-rays. Additionally, delayed gamma-rays and neutrons are emitted. These delayed particles can be detected to help identify and quantify SNM, making this one of the most reliable techniques for identifying SNM.

As described in Subsection 3.3.2, in the ENTRANCE project, the detection of delayed particles is achieved through the use of two independent photofission portals. Each portal is equipped with two detection systems: a long EJ-200 plastic scintillator for gamma-ray detection, and a thermal neutron detection system composed of Helium-3 gas proportional counters. These Helium-3 tubes are embedded within high-density polyethylene and encased by a cadmium layer. The cadmium absorbs thermal neutrons, protecting the Helium-3 detector from sources other than the fission of SNM, while the polyethylene thermalizes the fast neutrons before they reach the Helium-3 detector [37].

Intending to improve and innovate these detection systems in the ENTRANCE project, and exploring new ideas in the MULTISCAN 3D project, this work studies different alternatives for the detection systems used in the photofission applications. The proposed system involves using a novel flexible and conformable composite thermal neutron scintillator based on fully enriched Lithium Tetraborate ($^{6}Li_2{}^{10}B_4O_7$) for thermal neutron detection, substituting the Helium-3 detector. This new detector can be built in large areas, has flexible physical characteristics, good thermal neutron detection efficiency, and very low sensitivity to gamma-rays. For the gamma-ray detection, it is proposed a compact detection system capable of detecting and discriminating between gamma-rays and fast neutrons (discrimination capability not offered by the EJ-200) using an EJ-276G plastic scintillator or an EJ-309 liquid scintillator coupled to a SiPM array, instead of the PMTs currently used in the ENTRANCE project. This change would also make the system a low-SWaP (Size, Weight, and Power) solution.

Therefore, this chapter is divided into two sections: the first section presents the characterization of a thermal neutron detection system, and the second section details the characterization of gamma-ray and fast neutron detection systems to be used in the photofission system of the ENTRANCE and MULTISCAN 3D projects. Both characterization studies have already been published in scientific journals [60, 61].

7.2 Characterization of a thermal neutron detector for photofission applications

7.2.1 Introduction and previous work

Neutron detection is a field of increasing interest in nuclear and particle physics research, with applications spanning homeland security, neutron monitoring in power plants and radioactive waste repositories, material analysis, hydrology, radiation protection, industrial procedures, and nuclear medicine. Particularly in this work, neutron detection is crucial for identifying Special Nuclear Materials (SNM) in the photofission system. Currently, the ENTRANCE project makes use of ^{3}He proportional counters for this purpose.

The ^{3}He proportional counter is one of the most commonly used devices for neutron detection, thanks to its high neutron efficiency, insensitivity to gamma-rays, and lack of toxicity or flammability. However, a significant shortage of ^{3}He in recent years has led to a dramatic increase in its cost, making the search for alternative neutron detectors an urgent priority.

Besides ^{3}He proportional counters, various thermal neutron detectors with negligible or recognizable responses to gamma-rays have been researched. Different scintillation materials have been developed for this purpose, often combining neutron converters like ^{6}Li or ^{10}B with inorganic scintillators such as ZnS:Ag, ZnS:Cu, GYAGG, or perovskite nanocrystals, spread over substrates like aluminum or polymethyl methacrylate. More recent developments include scintillation compounds like $Gd_2O_2S:Tb^{3+}$, CLYC, and CLLB, where the neutron converter is included in the scintillator composition. While these materials achieve high neutron detection efficiency, they are typically rigid and fragile.

Previously, our research group has identified a promising alternative: a thin sheet combining ZnS:Ag powder with ^{6}LiF nano-crystals dispersed in polysiloxane rubber. This detector has demonstrated excellent performance, providing high thermal neutron detection efficiency comparable to commercial scintillators like the EJ-420 thermal neutron detector [62]. Seeking an even better alternative, it has been combined two potential neutron converters in order to create a more efficient thermal neutron detector (^{6}Li and ^{10}B), taking into account that the ^{10}B has a thermal neutron cross-section approximately four times higher than the ^{6}Li. The detector is synthesized using fully enriched Lithium Tetraborate ($^6Li_2{}^{10}B_4O_7$) nanocrystals embedded in a flexible polydimethylsiloxane (PDMS) matrix, loaded with an inorganic scintillator (ZnS:Ag powder). The PDMS support makes the detector light and flexible. The use of $^6Li_2{}^{10}B_4O_7$ (LiBO) could enhances the probability of capturing thermal neutrons due to its dual neutron capture reaction pathways. When a neutron is captured, light reaction products (alpha particles and tritium, see Figure 7.1) are emitted, potentially escaping the LiBO grain, traveling through the matrix, and striking the ZnS scintillating grains. The resulting scintillation light is then transmitted through the silicone to the read-out device (such as a photomultiplier or SiPM).

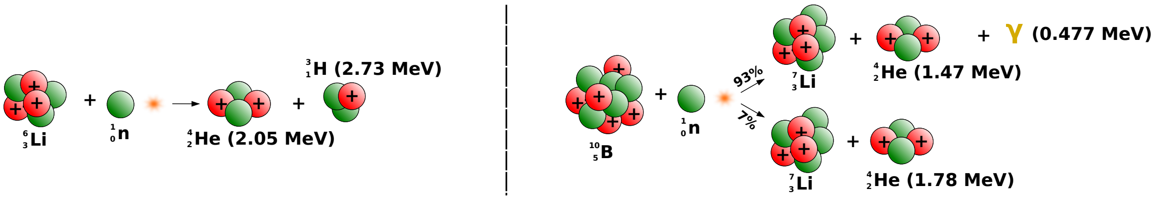

Figure 7.1: Thermal neutron capture reaction scheme of the $^6_3$Li and $^{10}_5$B.

The primary goal of this study is to develop a novel, flexible, and conformable composite scintillator to serve as a highly efficient thermal neutron detector for photofission applications and other needs. This aims to replace the current neutron detector used in ENTRANCE, which employs ^{3}He proportional counters. The proposed innovative detector is easy to assemble, scalable to large areas, resistant to bending, and composed of thermally resistant polysiloxane (PDMS, $T_d = 310°C$), promising a versatile sensing device.

Experimental measurements characterizing and exploring the potential of this detector are reported in this work. Also, the acquired results are compared to those of a commercial analog detector, the EJ-420. It should be noted that in order to implement this novel detector effectively in the photofission interrogation techniques, the configuration described in Subsection 3.3.2 will be necessary. This configuration involves embedding the thermal neutron detector within high-density polyethylene and encasing it with a cadmium layer. The polyethylene serves to thermalize neutrons before they reach the thermal neutron converter, while the cadmium layer prevents the detection of thermal neutrons from other sources.

Furthermore, it was explored the potentiality of this LiBO detector in a hybrid configuration for detecting and discriminating gamma rays, fast, and thermal neutrons. The configuration involves wrapping commercial plastic scintillators (EJ-299 and EJ-276G from Eljen Technology) with the LiBO-based scintillator, leveraging its flexibility. Achieving triple detection and discrimination with a single device is challenging and has been explored using various materials and configurations [63–70]. This proposed configuration represents an innovative detection system applicable in various fields and useful for determining the neutron spectrum during photofission inspections.

7.2.2 Methods and experimental description

Preparation of the LiBO/ZnS:Ag-based scintillator

The LiBO detector was constructed by a group at the Chemical Department of the University of Padova. They synthesized LiBO nanoparticles using the Pechini method, known for its precise size control and crystal quality. This involved mixing $^6Li_2CO_3$ and $H_3{}^{10}BO_3$ in specific ratios and subjecting the mixture to controlled heating processes. The resulting nanocrystals were characterized using high-resolution X-ray diffraction

(HR-XRD) and scanning electron microscopy-energy dispersive X-ray spectrometry (SEM-EDS) to determine crystal structure, composition, and morphology [60].

The scintillator material, consisting of zinc sulfide doped with silver (ZnS:Ag), was chosen for its high light output, making it one of the most efficient scintillation materials available commercially. Additionally, the silicone used (PDMS matrix) for depositing the mixed scintillator material was carefully chosen based on previous successful works, ensuring compatibility, flexibility, and lightness.

To determine the optimal configuration for the detector, various sample compositions were tested. Six samples were prepared, each containing the ZnS/LiBO mixture in the PDMS matrix at different concentrations: 20%, 30%, or 40% of the total volume. Additionally, within the ZnS/LiBO mixture, two weight ratios of ZnS to LiBO (3:1 and 2:1) were tested, reflecting common ratios used in commercial scintillators. All samples underwent thorough testing and characterization to identify the most effective detector composition for detecting thermal neutrons. The acquired results were also compared to a commercial analog detector, the EJ-420.

The EJ-420 thermal neutron detector, used for comparison purposes, from Eljen Technologies Texas-USA, is composed of zinc sulfide doped with silver (ZnS:Ag) as the scintillating material and lithium-6 (^{6}Li) as the neutron converter, whose Li content is enriched to 95% ^{6}Li. The scintillator is embedded in a rigid, durable binder, forming a solid composite layer approximately 6.5 mm thick. It exhibits high sensitivity to thermal neutrons but minimal flexibility.

In Figures 7.2a and 7.2b, two of the LiBO/ZnS:Ag-based scintillators produced are shown. All have the same physical characteristics: white color, excellent flexibility, a diameter of 50 mm, and a thickness of approximately 0.4 mm. Figure 7.2c shows the commercial analog detector EJ-420 (50 mm dia. x 6.4 mm thick). As can be seen, the EJ-420 is supported and surrounded by a rigid plastic material.

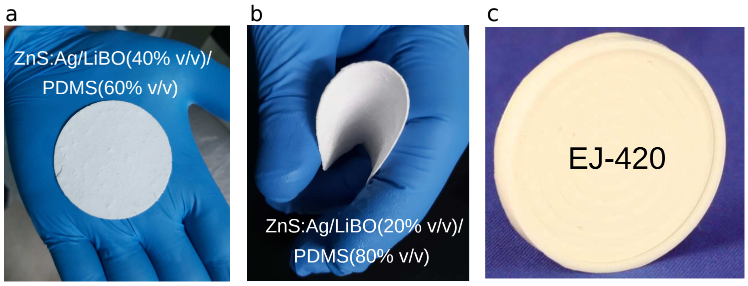

Figure 7.2: Pictures of two samples of the LiBO/ZnS:Ag-based scintillators produced (a) ZnS:Ag/LiBO(3:1)(40% v/v)/PDMS and (b) ZnS:Ag/LiBO(3:1)(20% v/v)/PDMS. (c) Commercial EJ-420 thermal neutron detector.

Experimental description for the characterization of the detector

The performance of the six ZnS:Ag/LiBO-based scintillators was tested with a thermal neutron flux at the Van de Graaff accelerator facility at Legnaro National Laboratories in Italy. Neutrons were generated by directing a proton beam onto a ^{7}Li target, resulting in the ^{7}Li(p,n)^{7}Be reaction (Q value of the reaction is approximately -1.64 MeV). The proton beam had a frequency of 3 MHz, a pulse width of 2 ns, and an energy of 5.5 MeV, producing fast neutrons with an energy of 3.8 MeV. The detector was positioned approximately 68 cm from the target and surrounded by polyethylene blocks (6 cm thick) to moderate the fast neutrons into a thermal neutron flux (see Figure 7.3 to have an overview of the experimental setup).

Additionally, the detectors were tested with a ^{252}Cf source (activity of 2000 kBq on 15/02/2014), which emits both neutrons and gamma rays. The source undergoes alpha decay (96.91%) and spontaneous fission (3.09%), emitting fast neutrons with a mean energy of around 2.1 MeV. A 6 cm thick polyethylene moderator was placed between the source and the detector, with a 15 cm distance between them. For hybrid detector tests, 2 cm of polyethylene was used to enhance the thermal neutron component of the flux.

Two photomultiplier tubes (PMTs) were used: a HAMAMATSU R6233 (operated at +1250 V and 7.6 cm diam.) for absolute light output measurements and a HAMAMATSU H1949-51 (operated at -1700 V and 5.1 cm diam.) for other tests. The emission wavelength peak of ZnS:Ag is around 450 nm, while the typical sensitivity range for PMTs is from about 300 nm to 650 nm. Scintillators were optically coupled to the PMTs with clear silicone grease. Signals were digitized by a fast CAEN digitizer (model V1730) with a 500 MSamples/s sampling rate and 14-bit ADC resolution. The digitizer's FPGA processed the waveforms online, providing timestamps and integrals for each triggered event. Digitized waveforms were also recorded for offline analysis.

A CAEN V6533 power supply module provided bias voltage to the PMTs. The HV unit and digitizer were controlled via a VME to PCI Optical Link Bridge (CAEN V2718) and a CAEN A3818 PCI Express CONET2 Controller, connected to a PC with optical fiber using the CAEN CONET2 protocol. Data acquisition and readout electronics were managed using the ABCD (Acquisition and Broadcast of Collected Data) software [50,51], available as open-source (https://github.com/ec-jrc/abcd). See Figure 7.3 for a schematic view of the DAQ system. A Figure of Merit (FoM) was used to evaluate the particle discrimination capabilities of the proposed assembly with the plastic scintillator (as described in Subsection 3.2).

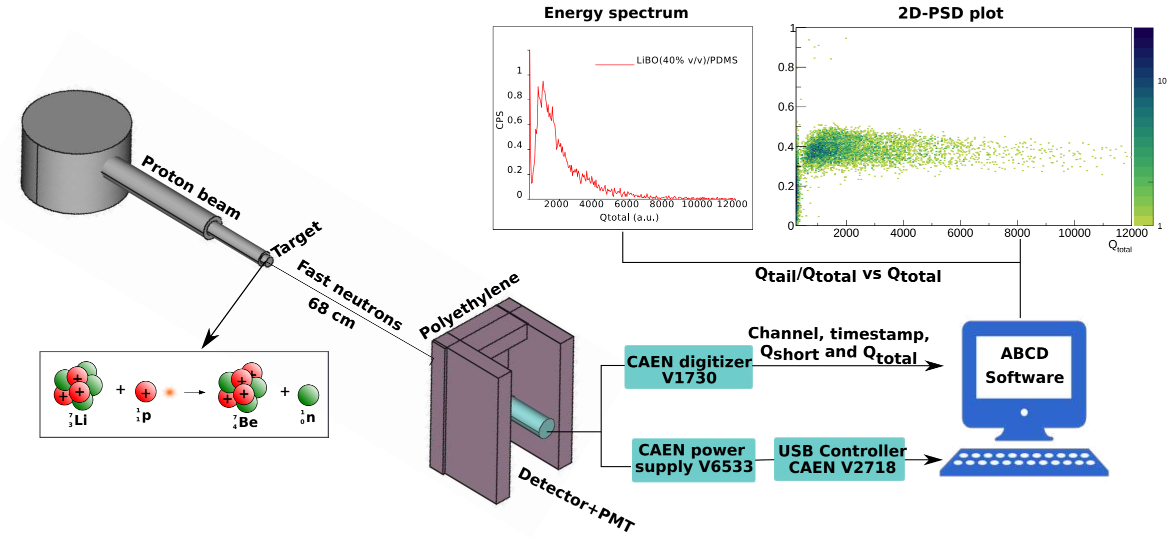

Figure 7.3: Schematic view of the experimental setup at the CN accelerator

Light Output and Gamma Rejection

The ZnS:Ag/LiBO/PDMS detector's light output per neutron capture reaction is calculated using the Bertolaccini method [71]. It compares the position of the PMT's single photoelectron peak (HAMAMATSU R6233) to the mean value of the detector's pulse-height spectrum when exposed to a thermal neutron flux. The calculation employs:

$$N_{ptm}(E) \propto N_{ph}(E) \cdot \eta_L \cdot QE(\lambda) \cdot \epsilon \tag{7.1}$$

where $N_{ptm}(E)$ is the total number of photoelectrons collected at the anode of the PMT when a thermal neutron is detected, η_L is the light collection efficiency, $N_{ph}(E)$ is the number of photons per energy unit produced in the scintillator at a given energy, $QE(\lambda)$ the quantum efficiency and ϵ the efficiency of photo-electron collection. Single photo-electron measurement can be conducted without any nearby source.

Another important parameter in the composite detector is the Gamma Rejection Ratio (GRR) [72], which is the intrinsic response of the neutron detector to the presence of a high γ-ray field when no neutron source is present.

$$GRR = \frac{N_{CPS}}{\Omega \cdot (\sum_{i,j} A_i \cdot \gamma_{i,j})} \tag{7.2}$$

where N_{CPS} is the false neutron counts per second, A_i is the activity of the i-th source, Ω is the solid angle and $\gamma_{i,j}$ is the intensity of the j-th gamma line of the i-th source. This characteristic was examined using five gamma sources (^{241}Am, ^{133}Ba, ^{137}Cs, ^{60}Co, and ^{22}Na) attached to the detector's face.

7.2.3 Results and analysis

Flexibility of the LiBO/ZnS:Ag-based scintillator

To explore the flexibility capabilities of the studied detector, a flexibility test was conducted on the LiBO scintillator. For comparative analysis, the same test was performed on the EJ-426 detector manufactured by Eljen Technologies. The EJ-426 thermal neutron detector shares a similar composition with the EJ-420 but utilizes a colorless binder, resulting in a thin composite layer approximately 0.25 mm thick with minimal flexibility.

The test involved holding a piece of scintillator from two edges and gradually bending it along the line connecting these points, reducing the bending radius without any restrictions. This process is illustrated in Figure 7.4. The results indicated that the ZnS:Ag/LiBO/PDMS scintillator could achieve a curvature radius as small as 1.5 mm, showcasing remarkable flexibility. This feature allows it to be easily adapted to various geometries. In contrast, the EJ-426 detector could not withstand a curvature radius lower than 16 mm.

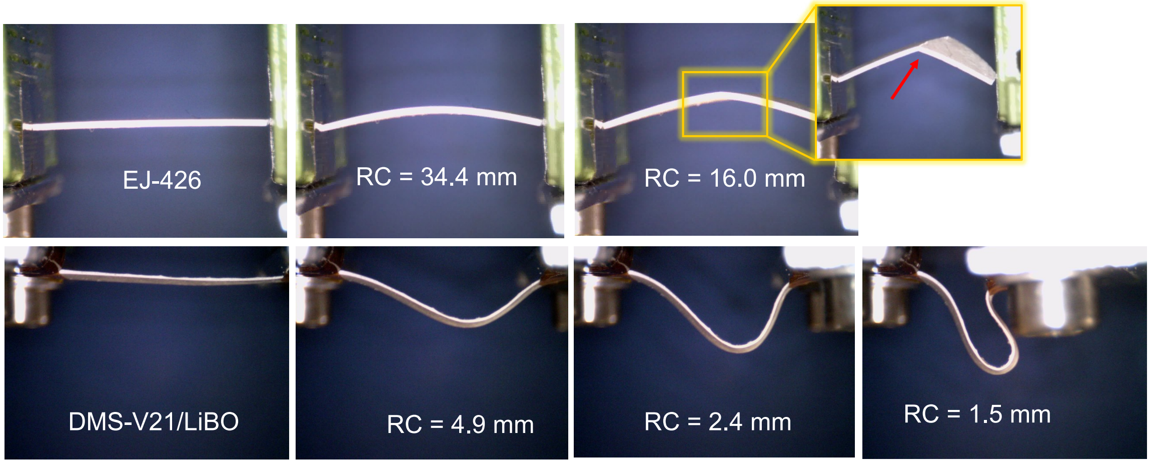

Figure 7.4: Pictures of the commercial scintillator EJ-426 (top row) and the ZnS:Ag/LiBO/PDMS detector (bottom row) clamped in a vice and bent at decreasing curvature radii.

Thermal neutron response of the LiBO/ZnS:Ag-based scintillators

The six different samples of ZnS:Ag/LiBO/PDMS scintillators were tested using the neutron flux generated by the ^{7}Li(p,n)^{7}Be reaction (proton energy $\sim$ 5.5 MeV) at the Van de Graaff accelerator at the Laboratori Nazionali di Legnaro – INFN. The mono-energetic fast neutrons ($\sim$ 3.8 MeV at 0°) were moderated by surrounding the detector assembly with a few centimeters of polyethylene. It has been demonstrated that $\sim$6 cm is a reasonable thickness for effective moderation [66].

In Figure 7.5a, typical waveforms corresponding to thermal neutron-induced events of the tested detectors are shown. The decay time of the ZnS:Ag/LiBO-based scintillator signal is approximately 200 ns, consistent with the decay time exhibited by the EJ-420 signals. Given that the fluorophore in the light-emitting composite sensor is the same (ZnS:Ag) used in EJ-420, a negligible difference in signal shape is expected.

Signal analysis was performed using the double integration method, or charge comparison method (explained in Subsection 3.2), to distinguish thermal neutron-induced events from other events such as gamma-ray induced events and noise. After applying the double integration method to all signals, 2D-PSD plots were generated, as seen in Figures 7.5b and 7.5c, illustrating the 2D-PSD plots of the EJ-420 and one of the ZnS:Ag/LiBO-based scintillators, respectively. The long (G_L) and short (G_S) integration gates of the signals were optimized to achieve the best visual distribution and separation of thermal neutron events in the 2D-PSD plots. The optimal values were found to be $G_L = 1.7\ \mu s$ and $G_S = 0.6\ \mu s$ for all six detectors under studied.

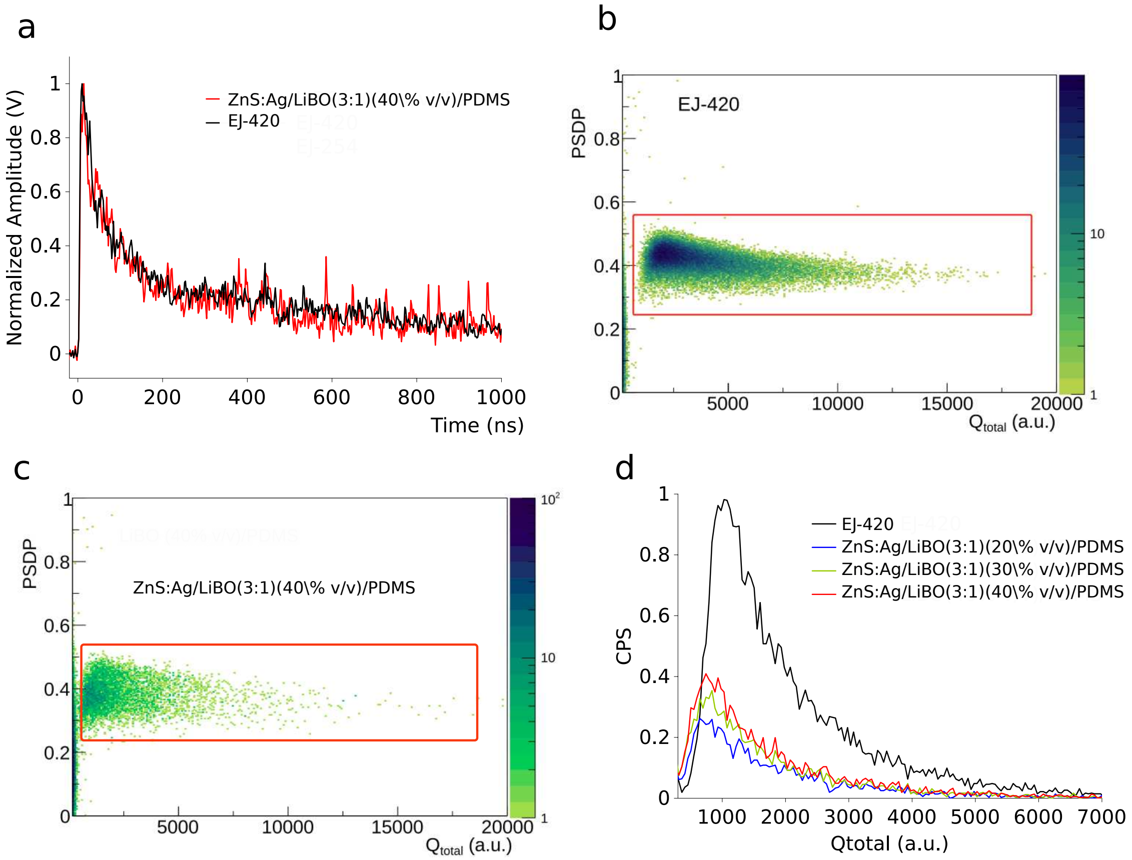

Figure 7.5: Typical waveform of the detector tested (a). 2D-PSD plots corresponding to the measurements with the neutron flux at the CN accelerator with the EJ-420 detector (b) and the ZnS:Ag/LiBO(3:1)(40% v/v)/PDMS detector (c). Energy spectrum of the detector tested with the ^{252}Cf source (d)

Given the 2:1 ratio of ^{10}B to ^{6}Li nuclei in LiBO and the approximately four times higher thermal neutron capture cross-section for ^{10}B, it is reasonable to assume that most recorded thermal neutron events are due to capture reactions on ^{10}B. However, signals from ^{10}B neutron capture have smaller amplitudes and integrals than those from ^{6}Li. This is because ^{10}B capture primarily generates alpha particle-induced scintillation (about 1.5 MeV), while the signal from ^{7}Li is highly quenched, which is the other ion resulting from this reaction (see reaction scheme in Figure 7.1). The quenching effect in scintillators is proportional to the particle's specific energy loss (dE/dx). Since Li ions are heavier and have a higher atomic number than alpha particles, they exhibit a higher dE/dx and thus a greater quenching effect. Conversely, in ^{6}Li capture, both reaction products, alpha particles ($\sim$ 2 MeV) and tritium ($\sim$ 2.7 MeV), contribute to signal generation. As it is in Figure 7.5d, where the Q_{total} mean values of the ZnS:Ag/LiBO-based scintillator spectra ($\sim$ 1200) are lower than the EJ-420 mean value ($\sim$ 2000).

Measuring the absolute detection efficiency of a neutron detector is a challenging task if there is no access to a well-characterized neutron field with known emission rates and angular distributions. Therefore, the neutron detection efficiency is reported relative to the EJ-420 commercial detector's performance. The thermal neutron counting rate for each detector was determined by integrating the light output (Q_{total}) spectrum (see Figure 7.5d). Figure 7.6 shows the relative thermal neutron detector efficiency compared to the EJ-420 for each tested scintillator. Uncertainties were calculated using standard error propagation procedures, taking into account error contributions from counting statistics.

In terms of detection efficiency, samples with a 2:1 weight ratio between ZnS:Ag powder and LiBO preparation showed the best responses. The ZnS:Ag/LiBO(2:1)(40% v/v)/PDMS scintillator achieved the highest thermal neutron detection efficiency, about 57% of the EJ-420. It is also notable from the data in Figure 7.6 that efficiency increases steadily with higher LiBO concentration, suggesting that even higher values could be achieved with further loading of thermal neutron-sensitive nuclei. However, in the last sample, no linear growth is observed, and a much higher efficiency is obtained. Various factors could have contributed to this result, such as variations in the detector composition or the increased proximity of the source.

As reported in [73], the typical absolute thermal neutron detection efficiency of ZnS-series phosphors with neutron converters (including commercial ones) ranges between 25% and 40%. The proposed LiBO-based scintillator, offers a response as good as other similar scintillation detectors, with an estimated absolute efficiency between 13% and 31% (considering the absolute thermal neutron detection efficiency of the EJ-420, which, according to its producer, exhibits an efficiency of 55%). This encouraging outcome, combined with the demonstrated outstanding mechanical properties, makes the ZnS:Ag/LiBO-based scintillator an optimal choice for thermal neutron detection in specific challenging applications, in particular to be used in photofission interrogation techniques.

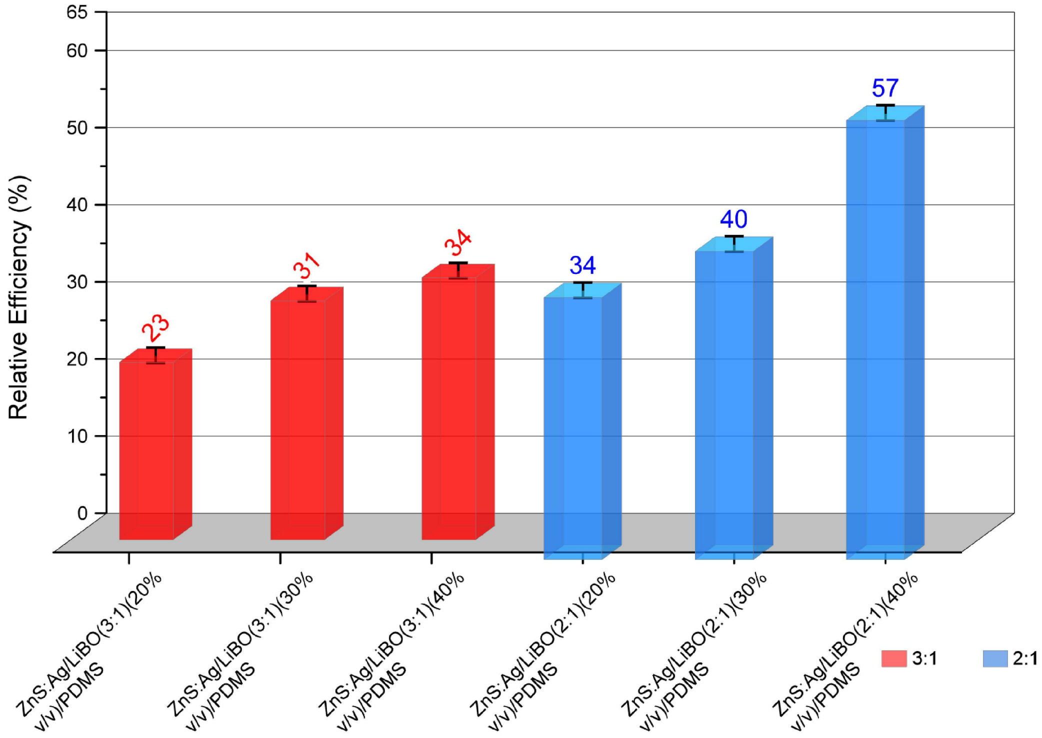

Figure 7.6: Thermal neutron relative efficiencies of the ZnS:Ag/LiBO-based detectors with respect to the EJ-420 detector.

According to the manufacturer, the lithium content of the EJ-420 scintillator is 9.03×10^{20} ^{6}Li atoms/cm^2 ($\sim$ 9 mg/cm^2). Our ZnS:Ag/LiBO-based scintillator, with 40 % v/v of ZnS:Ag/LiBO(2:1), contains 1.34×10^{20} ^{6}Li atoms/cm^2 ($\sim$1.3 mg/cm^2) and 2.67×10^{20} ^{10}B atoms/cm^2 ($\sim$4.4 mg/cm^2), that is $\sim$45% of neutron converter atoms with respect to the EJ-420. Considering only the ^{6}Li atoms, this proportion is further reduced to 15%. However, despite the expectation of observing a higher counting rate due to the fourfold larger cross-section of neutron capture on ^{10}B compared to ^{6}Li, we observed lower counts collected with the LiBO detector relative to the EJ-420. This discrepancy can be attributed to the fact that the alpha particles generated by the ^{10}B capture reaction may lack sufficient kinetic energy to reach a ZnS:Ag nanocrystal and produce scintillation light. Supporting this, calculations performed with the LISE++ code [74] indicate that the ranges of 1.5MeV and 2.0 MeV alpha particles in polydimethylsiloxane are approximately 7.3 and 10.6 μm, respectively, while the range of 2.7 MeV tritium ions is 60 μm (for better comprehension, an illustration of the range can be seen in Figure 7.7). Additionally, even if light is produced, it may be easily self-absorbed, due to the ionization quenching effect. This observation is consistent with previous research by our group, where a scintillation material based on ^{6}LiF nanoparticles, possessing a higher ^{6}Li content (2.6 mg/cm^2) and devoid of ^{10}B [62], exhibited greater thermal neutron detection efficiency relative to EJ-420 (up to 90%).

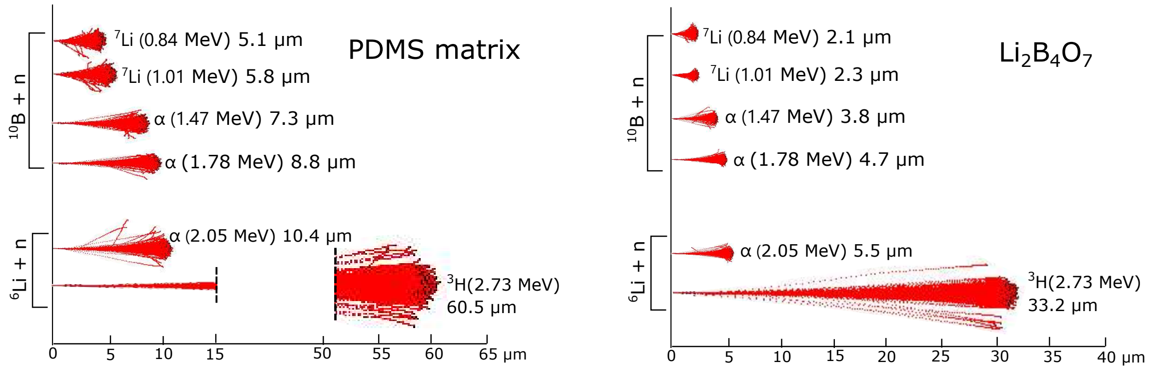

Figure 7.7: Simulated paths range on the polydimethylsiloxane matrix and on a LiBO target of the daughter products coming from the ^{6}Li and ^{10}B thermal neutron reaction. The simulation has been performed using the code Transmission of Ions in Matter (TRIM) [75].

Computational Model of the ZnS:Ag/LiBO-based Scintillator

To estimate the fraction of neutron capture reactions (on both ^{6}Li and ^{10}B nuclei) that produce measurable electric signals, we compared experimental thermal neutron detection responses of three ZnS:Ag/LiBO-based scintillators with predictions from a computational model. This model, based on Monte Carlo simulations using Geant4 v10.7, was developed based on measurements performed with a ^{252}Cf source.

The comparison focused particularly on scintillator samples with a weight ratio of 3:1 between ZnS:Ag powder and LiBO preparation. Additionally, a sample with a 2:1 ratio was studied and showed no significant difference compared to the 3:1 ratio.

The computational model represents the LiBO-based scintillator as a homogeneous disc with a diameter of 50 mm and a thickness of 0.4 mm, consistent with average real samples. While the actual light production in the scintillator depends on its heterogeneity, the Monte Carlo model does not simulate scintillation light yield and transport; such simulations would require consideration of compound heterogeneity.

The primary objective of the Monte Carlo model is to quantify neutron capture reactions. By comparing these with experimentally observed counting rates, the model provides an estimation of the fraction of neutron captures that result in measurable events.

The simulation included isotropic emission of primary neutrons with energies sampled from the ^{252}Cf spontaneous fission spectrum [76]. Approximately 4×10^7 primary neutron events were simulated, replicating experimental setups including scintillator composition and geometry, and a polyethylene moderator (as seen in the experimental setup in Figure 7.3).

Neutron transport was simulated using the QGSP_BERT_HP physics list, which includes a high-precision neutron model for low-energy neutrons (< 20 MeV). Detailed event tracking was achieved using the G4Step and G4Track classes within the G4UserSteppingAction class (see Subsection 3.5.1 for a detailed explanation of the classes). The model recorded neutron capture reactions by monitoring energy deposition when reaction products (e.g., α particles or tritium for ^{6}Li, and α particles or ^{7}Li for ^{10}B) were detected within the scintillator volume.

Table 7.1 presents a comparison of experimental and simulated total neutron efficiencies. Experimental efficiency was calculated by dividing the neutron count rate (events per second) by the emission rate of neutrons from the source. Similarly, simulation results were derived by dividing total neutron capture reactions by the number of primary neutrons emitted.

Across all investigated scintillators, the ratio of experimental to simulated efficiencies was approximately 10%, indicating that only a fraction of neutron captures in the scintillator material result in quantifiable events. This loss of events can be attributed to factors such as the non-interaction of emitted reaction products with the ZnS:Ag scintillator (specially from the boron reaction) and light scattering within the detector, resulting in light loss before reaching the photomultiplier window.

Table 7.1: Experimental and simulated thermal neutron efficiencies registered by three of the ZnS:Ag/LiBO-based detectors, using the ^{252}Cf source moderated with 6 cm of polyethylene.

ZnS:Ag/LiBO scintillator	Experimental eff. ± 0.0004%	Simulation eff. ± 0.0004%	Exp. to sim. eff. ratio ±0.05%
LiBO 20% v/v	0.0133	0.1308	10.19
LiBO 30% v/v	0.0175	0.1622	10.76
LiBO 40% v/v	0.0201	0.1791	11.19

Absolute light output of the ZnS:Ag/LiBO-based scintillator

Using the Bertolaccini method [71], we determined the average absolute light output of the ZnS:Ag/LiBO-based detector per neutron capture event. This method involves comparing the peak centroid position of the single photoelectron spectrum from the photomultiplier tube (PMT) with a specified position on the pulse-height spectrum of the scintillator under experimental conditions, in particular using a ^{252}Cf source moderated with 6 cm of polyethylene.

The average absolute light output, determined using the position of the average total charge (Q_{total}), was $9000 \pm 5\%$ photoelectrons per neutron capture event, with a maximum estimated at around 30000 photoelectrons. Figure 7.8 illustrates the pulse-height spectra comparison. For comparison purposes, a typical detector using ZnS:Ag/^{6}LiF has a high light output of 160000 photons per neutron, while Ce^{3+}-doped Li glasses have a low light output of 7000 photons per neutron [77].

To verify that the measurement was performed correctly and the technique was applied properly, tests were also conducted with BGO and EJ-200 scintillators using a gamma source. The results were in agreement with previous studies [71, 78].

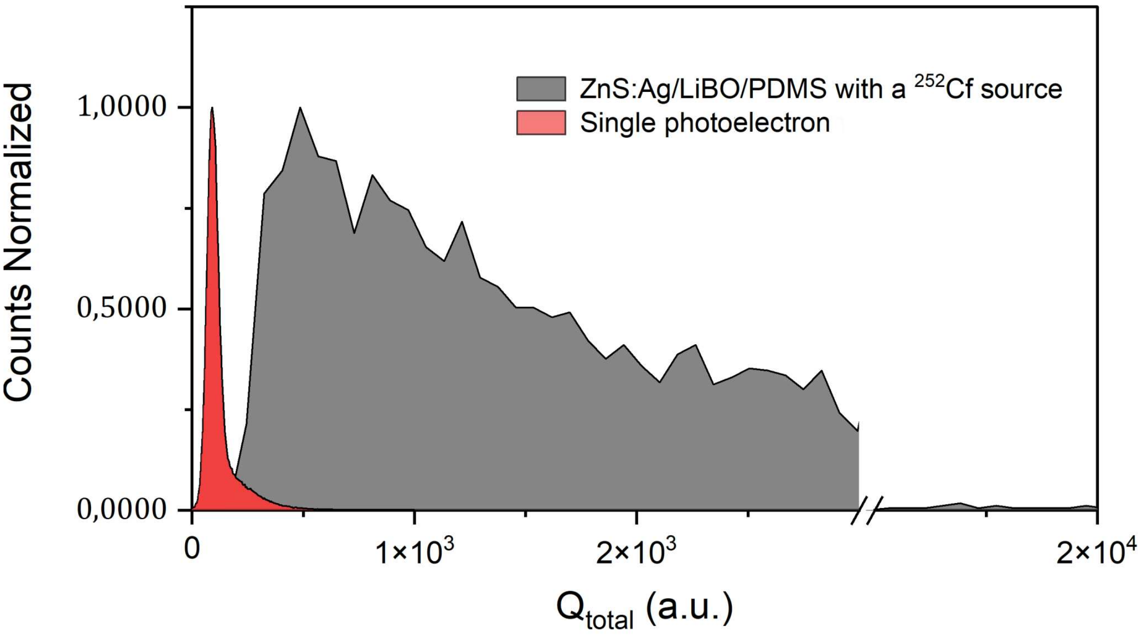

Figure 7.8: Pulse-height spectra of the single photoelectron response of the PMT, and the ZnS:Ag/LiBO-based detector using a ^{252}Cf source moderated with 6 cm of polyethylene.

Response of ZnS:Ag/LiBO-based Scintillator under a High Gamma Rate Field

The response of ZnS:Ag/LiBO-based detectors under a high gamma field, without a neutron source present, was tested using five gamma sources (^{241}Am, ^{133}Ba, ^{137}Cs, ^{60}Co, and ^{22}Na), each with an activity of approximately 300 kBq. A 12-hour measurement was conducted with the gamma sources placed extremely close to the detector's face. The number of false counts in the thermal neutron region was identified using a 2D-PSD plot, similar to the one shown in Figure 7.5c. The resulting counting rate was $0.006 \pm 5\%$ cps, yielding a Gamma Rejection Ratio (GRR) parameter of less than (10^{-11}). This demonstrates the ZnS:Ag/LiBO-based scintillator's remarkable lack of sensitivity to gamma-rays.

This low sensitivity to gamma-rays enhances the ZnS:Ag/LiBO/PDMS detector's suitability for neutron detection across various applications, including photofission, where high gamma rates can significantly interfere with neutron detection.

Notably, the EJ-420 scintillator exhibits higher gamma-ray sensitivity than the LiBO-based scintillator, with a GRR of 10^{-7}, according to the manufacturer.

ZnS:Ag/LiBO/PDMS Scintillator Coupled to a Plastic Scintillator: Triple Particle Discrimination with a Single Hybrid Assembly

By coupling a ZnS:Ag/LiBO/PDMS scintillator (specifically, ZnS:Ag/LiBO 3:1; 20% v/v, chosen due to material availability) to a plastic scintillator with fast neutron/gamma-ray discrimination capability, it is possible to construct a highly efficient detector unit capable of simultaneously discriminating between thermal neutrons, fast neutrons, and gamma-rays. For this purpose two plastic scintillators were used: a 1"×1" EJ-276G and a 2"×2" EJ-299. Figure 7.9a shows both plastics covered by the thermal neutron scintillator, with circular pieces used to cover one of the flat surfaces of the plastic scintillators also shown. In particular, the EJ-299 plastic was coupled to an H1949-51 Hamamatsu PMT (operated at -1700 V and 5.1 cm diam.), while the EJ-276G plastic was coupled to an array of silicon photomultipliers (Hamamatsu MPPC 4x4 array model S14161-6050HS-04) (see Figure 7.9b).

To evaluate the ZnS:Ag/LiBO/PDMS scintillator, three types of assemblies were tested with the EJ-299 plastic scintillator. The first assembly involved covering one flat face of the plastic with the ZnS:Ag/LiBO-based scintillator, with the other face coupled to the PMT window. In the second assembly, the flexible ZnS:Ag/LiBO-based scintillator was wrapped around the curved surface of the plastic scintillator (see Figure 7.9a). The third assembly, used for comparison, consisted of an EJ-420 disk (2" in diameter) optically coupled to one face of the EJ-299. A ^{252}Cf source, moderated with 6 cm of polyethylene, was placed in front of the detector. The thermal neutron efficiencies, compared to the EJ-420, were (0.16 ± 2%) for the first configuration and (0.28 ± 2%) for the second, indicating a 75% enhancement in thermal neutron detection efficiency when the curved walls of the 2" plastic scintillator were fully covered.

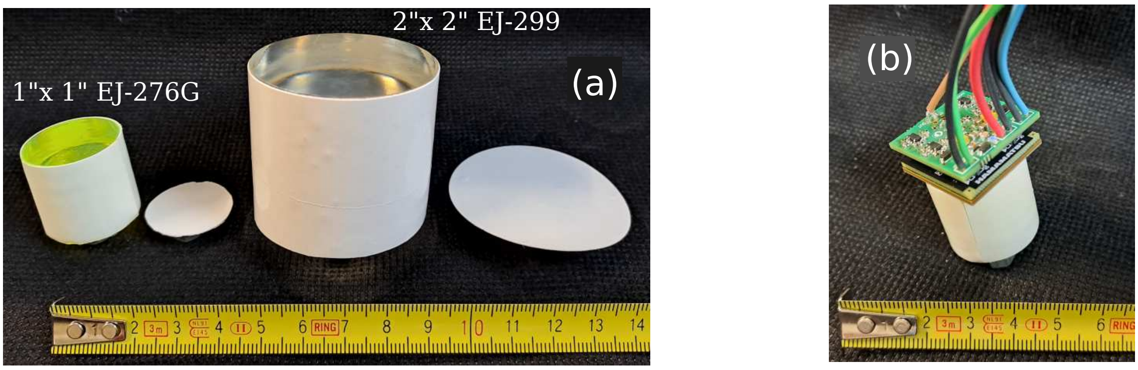

Figure 7.9: Picture of the hybrid assemblies 1"×1" EJ-276G and 2"×2" EJ-299 wrapped with the LiBO-based scintillator (a). Picture of the EJ-276G/LiBO hybrid detector coupled to a Hamamatsu S14161-6050HS-04 MPPC array (b).

Figures 7.10a and 7.10b show the 2D-PSD and 1D-PSD plots for the measurement when the EJ-299 plastic scintillator is completely wrapped with the ZnS:Ag/LiBO(3:1) (20% v/v)/PDMS scintillator. In these figures, clusters of gamma-rays, fast neutrons, and thermal neutron-induced events are clearly recognizable. The Figures of Merit (FoM) for discrimination between fast neutrons and gamma-rays, and between fast and thermal neutrons, were FoM[n-γ] = (1.29 ± 0.02) and FoM[n-n$_{th}$] = (3.75 ± 0.02), respectively. The light output of the events in the shaded region ranges approximately from 0.5 to 1 MeVee. Few events are located between the fast and thermal neutron zones, corresponding to pile-up events. The gamma-ray region in the 2D-PSD plot is slightly curved at high energies, likely due to the PMT's non-linear behavior, which can be minimized by operating the PMT at a lower bias or using silicon photomultipliers instead, which have shown a highly linear response, over a wide energy range of through-passing particles. Figures 7.11a and 7.11b show the 2D-PSD and 1D-PSD plots of the EJ-276G/LiBO assembly coupled to the MPPC array, demonstrating excellent particle discrimination and linearity. FoM values were obtained using the events in the shaded region in Figure 7.11a FoM values obtained FoM[n-γ] = (1.60 ± 0.02) and FoM[n-n$_{th}$] = (3.56 ± 0.02) (light output ~0.4-0.6 MeVee).

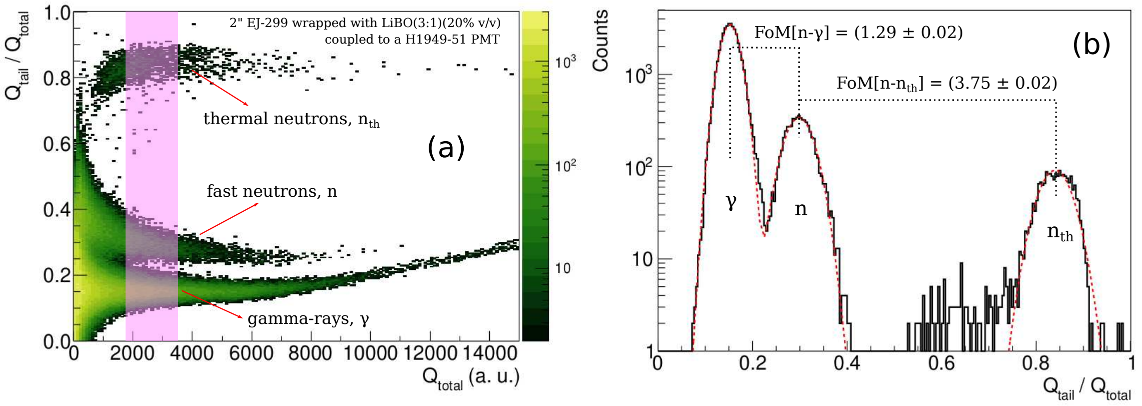

Figure 7.10: 2D-PSD (a) and PSD (b) plots of the hybrid assembly 2"×2" EJ-299 completely wrapped with the ZnS:LiBO(3:1)(20% v/v)/PDMS-based scintillator coupled to an H1949-51 Hamamatsu PMT, using a moderated ^{252}Cf source.

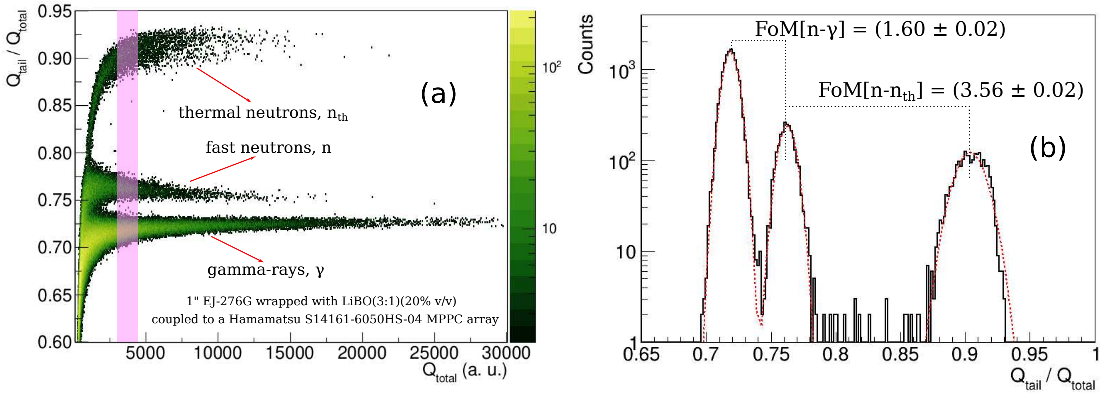

Figure 7.11: 2D-PSD (a) and PSD (b) plots of the hybrid assembly 1"x1" EJ-276G wrapped with the ZnS:LiBO(3:1)(20% v/v)/PDMS-based scintillator, coupled to a Hamamatsu S14161-6050HS-04 MPPC array, using a moderated ^{252}Cf source.

For both types of read-out devices (PMT and MPPC), the long (G_L) and short (G_S) integration gates were optimized to maximize the FoM for fast neutron and gamma-ray discrimination. In both cases, events with a light output larger than 0.4 MeVee, are completely separated between gamma rays and fast neutrons, with a FoM value greater than FoM > 1.2, and thermal neutron events are entirely separated from other events. This represents a significant improvement compared to previous works exploring triple particle discrimination, such as those involving lithium tetraborate nanoparticles-loaded plastic scintillators [79], where thermal neutron events were almost indistinguishable from fast neutron events, and other comparisons made by our group [67], and Sharma et al. [68], where the assembly of heterogeneous detectors posed challenges due to poor flexibility.

Studying this configuration holds significant value for the photofission interrogation techniques utilized in the ENTRANCE and MULTISCAN 3D projects. This setup allows for the determination of the spectrum of fast neutrons emitted by Special Nuclear Material (SNM) during photofission. In this process, fast neutrons initially interact with the plastic scintillator, emitting prompt signals. While most of these neutrons escape the detector, some are slowed down within the plastic scintillator and transformed into thermal neutrons. These thermal neutrons can then be captured by the LiBO scintillator, producing delayed scintillation signals. By correlating these prompt and delayed signals, it becomes possible to determine the energy spectrum of the neutrons. The calculation of the neutron spectrum can be performed as done in the following work: [80]. This paper presents a compact, broad-spectrum neutron spectrometer capable of measuring thermal, epithermal, and fast neutrons up to 10 MeV, using three detectors: a fast neutron detector (plastic scintillator EJ-254), a thermal neutron detector (NaI(Tl+Li) scintillator in an Al shell), and an epithermal neutron detector (same NaI(Tl+Li) scintillator in a Cd shell). For fast neutron energy determination, the capture-gated method combined with the Maximum Likelihood Expectation Maximization (MLEM) unfolding algorithm was used to obtain the energy spectrum from 0.5 to 10 MeV.

7.2.4 Summary

In conclusion, the development and characterization of the ZnS:Ag/LiBO/PDMS scintillator implies a significant breakthrough in thermal neutron detection, specifically designed to replace current Helium-3 detectors used in the photofission interrogation technique within the ENTRANCE project. The urgent need for a substitute arises due to the ongoing shortage of ^{3}He, prompting exploration into new detection technologies.

This study has demonstrated the scintillator's ability to achieve acceptable thermal neutron detection efficiency, coupled with exceptional mechanical flexibility and robust gamma-ray rejection capabilities. By integrating fully enriched Lithium Tetraborate (LiBO) nanocrystals within a polydimethylsiloxane (PDMS) matrix alongside ZnS:Ag scintillating powder, the detector mechanics adapts to diverse geometries and environmental conditions.

Experimental results have validated the scintillator's efficacy, achieving up to 57% relative thermal neutron detection efficiency with respect to a commercial detector (EJ-420), with the potential for further enhancement through optimized LiBO concentrations or the use of a lithium-based detector only. The scintillator's mechanical resilience was highlighted by its capability to achieve a curvature radius as small as 1.5 mm, ideal for compact and flexible applications.

Furthermore, comprehensive gamma-ray rejection capabilities were demonstrated with a Gamma Rejection Ratio (GRR) below 10^{-11}, crucial for precise neutron detection among high photon backgrounds encountered during SNM irradiation.

Monte Carlo simulations using Geant4 v10.7 further validated the detector's performance, showing that only 10% of neutron captures in the scintillator material produce measurable events. The scintillator exhibited an reasonable light output of $9000 \pm 5\%$ photoelectrons per neutron capture event.

Moreover, leveraging the flexibility of the LiBO detector, a hybrid assembly was tested using the ZnS:Ag/LiBO/PDMS scintillator coupled with plastic scintillators (EJ-276G and EJ-299). The tests demonstrated good discrimination between thermal neutrons, fast neutrons, and gamma rays, crucial for precise neutron energy spectrum determination in applications like those of the ENTRANCE and MULTISCAN 3D projects, for identifying the isotope corresponding to the interrogated SNM, or for discarding neutrons that do not originate from the SNM.

In summary, the ZnS/LiBO/PDMS scintillator shows potential as an alternative to traditional ^{3}He proportional counters, offering good thermal neutron detection performance, flexibility, and gamma-ray rejection capabilities that are essential for advancing neutron detection technology. This makes it a promising candidate for photofission systems in projects like ENTRANCE and MULTISCAN 3D. Additionally, this technology has great potential in a wide variety of applications, such as homeland security [81], neutron monitoring in power plants and radioactive waste repositories [82], neutron imaging [83], material analysis, radiation protection, and nuclear medicine [84], among others.

Future improvements could be made by developing detectors with similar characteristics but incorporating LiF nanoparticles instead of LiBO. While the inclusion of boron was expected to improve performance due to its higher thermal neutron capture cross-section compared to lithium, our findings indicate that the reaction products from boron do not carry enough energy to reach the ZnS:Ag and generate scintillation light.

7.3 Characterization of gamma-ray and fast neutron detection system for photofission applications

7.3.1 Introduction and previous work

Gamma rays emitted from actinides following fission in the photofission system of the ENTRANCE projects are currently detected using two long EJ-200 plastic scintillators coupled to PMTs. This study aims to innovate and enhance this detection system by proposing the substitution of the current system with an organic scintillator capable of detecting and distinguishing gamma rays and fast neutrons. The organic scintillator will be coupled to a SiPM array instead of a conventional PMT, aiming for a low-SWaP (Size, Weight, and Power) solution. The proposed solution can also be applied in the photofission system of the MULTISCAN 3D project.

The transition from PMTs to SiPMs is driven by the rapid advancements in SiPM technology, which have unlocked promising opportunities across various fields including high-energy physics, medical imaging, astronomy, hazard detection [85–87], and specifically for photofission applications in this case. SiPMs are highly sensitive and efficient light sensors capable of operating across a wide spectrum from near ultraviolet to near-infrared wavelengths. Consisting of an array of micro-cells interconnected in parallel, each micro-cell functions as a Geiger-Mode avalanche photodiode [88], offering advantages such as high photon detection efficiency, significant signal amplification at low voltages, compact design, and immunity to magnetic fields [89, 90].

Despite these strengths, SiPMs do present challenges such as longer single photon response times and higher noise levels due to phenomena like dark pulses and after-pulsing. These challenges influence factors like pixel recovery times and capacitance, particularly in applications requiring fast response times and minimal afterpulsing [91, 92]. Nonetheless, SiPMs have demonstrated impressive outcomes in sensitivity, efficiency, and particle discrimination capabilities.

The SiPM array market is diverse, with manufacturers like Hamamatsu, SensL, Ketek, and AdvanSiD offering arrays customized to specific performance criteria including photon detection efficiency, timing resolution, dark count rates, and after-pulsing probability. Choosing the appropriate SiPM array is critical and depends on the specific application and experimental requirements. To aid in informed decision-making, various studies have compared SiPM arrays across different metrics. For instance, Grodzicka-Kobylka et al. compared SensL and Hamamatsu SiPM arrays in gamma-spectrometry, evaluating parameters like energy resolution and stability [93]. Another study by Gonzalez-Montoro examined SensL, Hamamatsu, and Ketek SiPM arrays under varying conditions, providing insights into their performance with different detector materials [94]. Additionally, research has explored the ability of SiPM arrays coupled to organic scintillators to discriminate between neutron and gamma-ray signals, a crucial capability in radiation detection applications, particularly for identifying SNM [95].

Achieving Pulse Shape Discrimination (PSD) using SiPM arrays is a challenging task, primarily because PSD relies on reconstructing the time profile of scintillation decay. Nevertheless, previous studies have shown effective neutron/gamma-ray discrimination with millimeter-scale scintillators and single SiPMs [91, 96, 97]. However, scaling up to large-area SiPM arrays for medium-sized scintillators remains difficult, as achieving PMT-level discrimination performance is challenging [98–101]. Nevertheless, a prior study by our group demonstrated the feasibility of n/gamma-ray discrimination using large-sized scintillators coupled with large-area SiPM arrays [102]. In that study, three commercial scintillators (EJ-276, EJ-309, and EJ-301) with diameters ranging from 20 to 50 mm were utilized in conjunction with two large-area SiPM arrays from AdvanSiD, NUV (Near Ultraviolet light) and RGB (Red-Green-Blue light). Successfully, optimum n/gamma-ray discrimination results were obtained for all combinations, yielding outcomes comparable to those achieved with a PMT as the read-out. Building upon these advancements, we continue our research but this time focusing on the utilization and comparison of different types of SiPM arrays.

Therefore, this study expands our investigation by evaluating the performance of two medium-sized organic scintillators (EJ-276G and EJ-309) with neutron/gamma-ray discrimination capabilities coupled with three different SiPM arrays (AdvanSiD-NUV ASD-NUV4S-P-4x4TD, Hamamatsu S14161-6050HS-04, Ketek PA3325-WB-0404). Our assessment includes an analysis of energy resolution, time resolution, and neutron/gamma-ray discrimination performance for each configuration [98]. This research aims to provide comprehensive insights into the performance characteristics of these six configurations, offering valuable guidance to future researchers and experimenters in selecting the most suitable SiPM array for specific applications. Furthermore, it introduces an innovative and enhanced gamma-ray detection system for the photofission technique used in the ENTRANCE and MULTISCAN 3D projects. Unlike the EJ-200 used in ENTRANCE projects, which lacks discrimination between gamma rays and neutrons, our SiPM technology enables precise discrimination between these radiation types. Additionally, this new technology offers a compact, lightweight system with low power consumption.

7.3.2 Methods and experimental description

SiPM arrays

The three tested SiPM arrays are the AdvanSiD Hybrid TD Array NUV-SiPM (16 channels, 4 mm x 4 mm active area per channel), the Hamamatsu S14161-6050HS-04 (16 channels, 6 mm x 6 mm active area per channel), and the Ketek PA3325-WB-0404 (16 channels, 3 mm x 3 mm active area per channel). Images of these arrays are shown in Fig. 7.12, and their key characteristics are detailed in Table 7.2. Fig. 7.13 displays the Photon Detection Efficiency (PDE) of these SiPMs in function of the wavelength (with overvoltage specifications of +6 V for AdvanSiD, +2.7 V for Hamamatsu, and +5 V for Ketek), alongside the emission curves of the plastic and liquid scintillators.

All three SiPM arrays cover the wavelength emission range of the organic scintillators, with the best alignment observed between the Hamamatsu SiPM and the emission peak of the liquid scintillator. To quantify the sensitivity match between each SiPM and the emission curves of the scintillators listed in Table 7.3, a convolution value is assigned. This value indicates the likelihood of a scintillation photon, sampled from the emission spectrum, to be converted into a photoelectron by the respective SiPM array. Notably, the highest probability is associated with the EJ-309/Hamamatsu configuration.

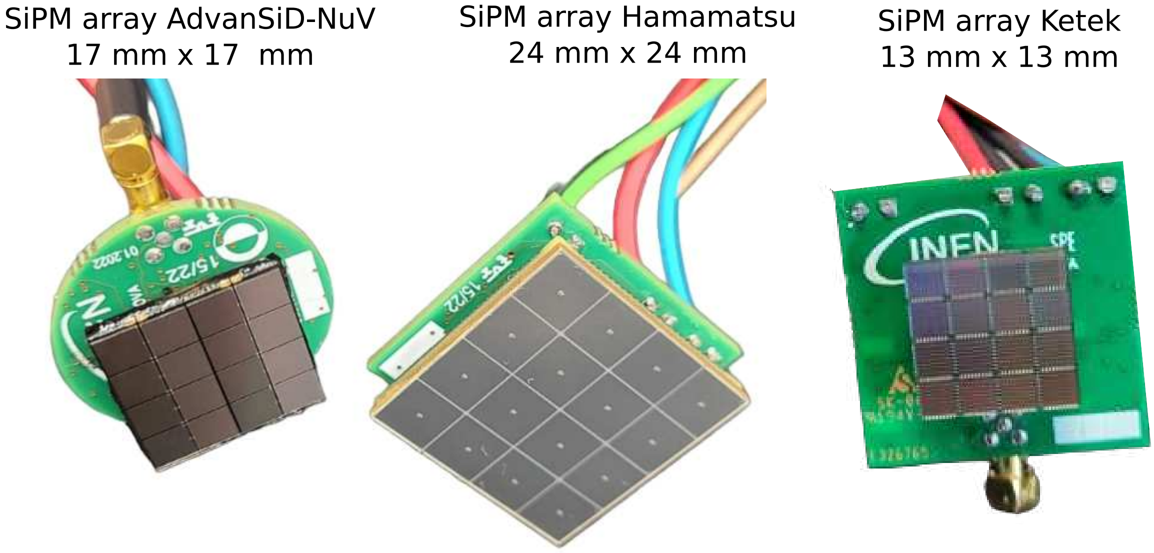
SiPM array AdvanSiD-NuV 17 mm x 17 mm
SiPM array Hamamatsu 24 mm x 24 mm
SiPM array Ketek 13 mm x 13 mm

Figure 7.12: Pictures of the AdvanSiD-NUV, Hamamatsu, and Ketek SiPM arrays.

Table 7.2: Main Characteristics of the SiPM arrays tested

	AdvanSiD-NUV	Hamamatsu	Ketek
Array size	17 mm x 17 mm	24 mm x 24 mm	13 mm x 13 mm
Single SiPM size	4 mm x 4 mm	6 mm x 6 mm	3 mm x 3 mm
Channel number	16 channels	16 channels	16 channels
No. of cells/channels	9340	14331	13920
Cell size	40 μm x 40 μm	50 μm x 50 μm	25 μm x 25 μm
Recharge time	70 ns	$>$ 50 ns	80 ns
Cell capacitance	90 fF	140 fF	72 fF
Peak sensitivity wavelength	420 nm (43%)	450 nm (50%)	420 nm (45%)
Breakdown voltage, typ	26 V	38 V	24.5 V
Dark count rate	$<$ 100kHz/mm^2 @4V OV	7.5μA @4V OV	3.4μA @7V OV

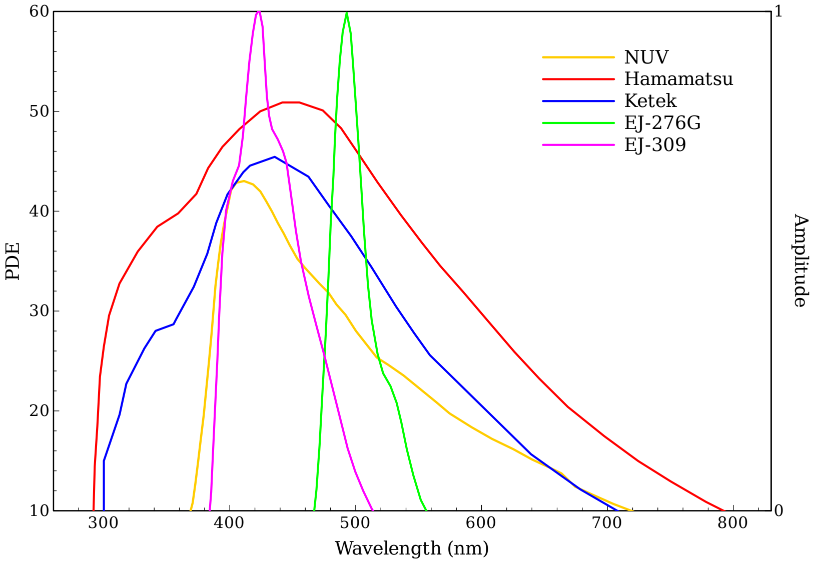

Figure 7.13: Photon Detection Efficiency (PDE) corresponding to the AdvanSiD, Hamamatsu, and Ketek SiPM arrays (left axis) compared with the emission curves of the plastic and liquid scintillators (right axis). Information is taken from the manufacturers.

Table 7.3: Photon detection efficiency multiplied by the normalized emission spectrum for each SiPM array/scintillator combination

Scintillator/SiPM array	I=$\sum_{250nm}^{900nm}$PDE(λ) · A(λ)$\Delta\lambda$
EJ-276G/AdvanSiD	27.3
EJ-276G/Hamamatsu	44.4
EJ-276G/Ketek	35.2
EJ-309/AdvanSiD	37.3
EJ-309/Hamamatsu	48.6
EJ-309/Ketek	42.4

Organic scintillators

To evaluate the SiPM arrays' performance, two organic scintillators capable of discriminating between neutron and gamma ray signals were utilized: a cylindrical plastic scintillator, EJ-276G (25 mm diameter × 25 mm thickness), and a cylindrical liquid scintillator, EJ-309 (50 mm diameter × 50 mm thickness), both sourced from Eljen Technology–Texas, USA. Optical grease was applied to optimize the coupling between the detectors and the SiPM arrays (see Fig. 7.14). The EJ-309 is housed in a sealed, reflective container, whereas the EJ-276G remains exposed. Therefore, the plastic scintillator was carefully covered with Teflon tape, leaving the area where it interfaces with the SiPM uncovered.

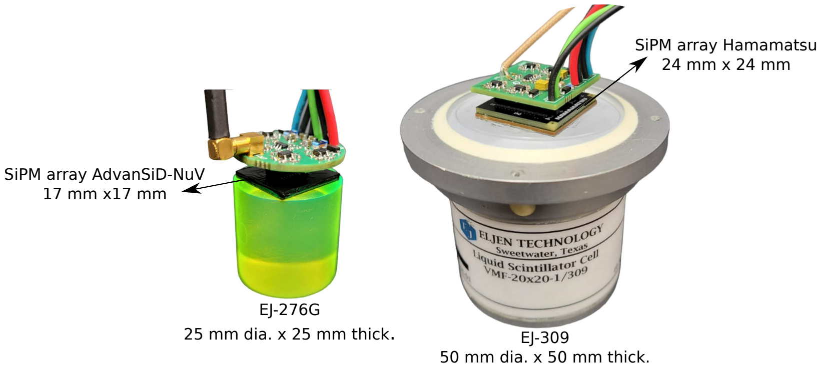

Figure 7.14: Picture of the EJ-276G and the EJ-309 scintillators coupled to the AdvanSiD-NUV and Hamamatsu SiPM arrays, respectively.

Readout board of the SiPM arrays

The SiPM array's output and bias voltage supply were managed through a specialized board organized into sets of four. Each set consists of four SiPMs connected in parallel. The output signals from each set are amplified using trans-impedance preamplifiers featuring an ultra-low noise, high-speed OpAmp (LMH6629). These amplified signals are then combined to produce the overall output signal. Fig. 7.15 provides a simplified diagram of the readout board to clarify the circuit configuration.

Each OpAmp receives voltage inputs of ±2.9 V, while the applied bias voltage ranges from 30 to 40 V, depending on the specific SiPM array used. Importantly, the same bias voltage is uniformly applied to each SiPM across the array.

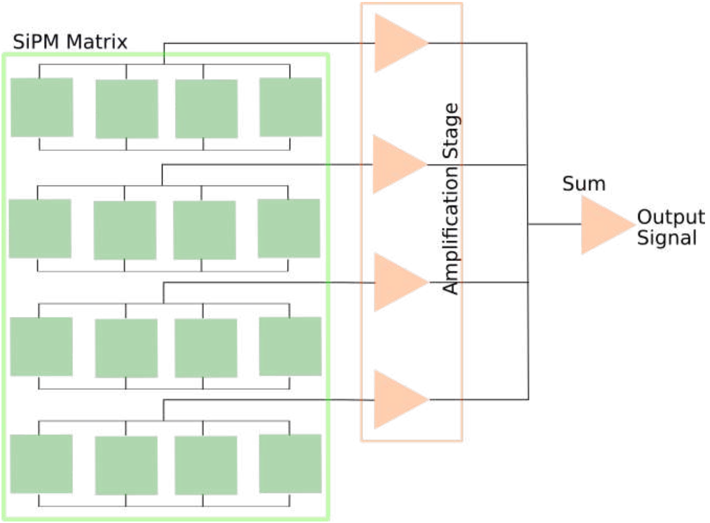

Figure 7.15: Circuit diagram of the SiPM arrays' readout board.

Experimental details

The SiPM arrays' readout boards were powered by an Aim-TTi MX180T multi-range DC power supply. To optimize energy resolution for each detector assembly, the over-voltage (OV) applied to each SiPM was carefully adjusted. For the $LaBr_3$:Ce detector used in coincidence applications, a bias voltage of +800 V was supplied to the PMT (R6231), controlled via a V6533 CAEN power supply unit connected to a USB Controller (CAEN V1718).

Output signals were digitized using a V1730 CAEN digitizer, featuring a sampling rate of 500 MSamples/s and a 14-bit ADC resolution. These modern digitizers utilize programmable FPGA (Field Programmable Gate Array) technology, enabling real-time preprocessing of digitized waveforms. This functionality allows the digitizer to provide various data for each triggered event, including timestamps, total charge (Q_{total}), and partial charge (Q_{short}) waveform integrals.

Data acquisition was facilitated by an optical fiber connection, with the digitizer linked to a PC via a CAEN A4818 USB 3.0 to CONET2 Adapter. The ABCD (Acquisition and Broadcast of Collected Data) software [50, 51], an open-source project, was used to manage electronics and data acquisition.

The experimental setup included measurements with two gamma-ray sources, ^{22}Na and ^{137}Cs (each with activities of approximately 300 kBq), and a n/gamma-ray source ^{241}Am-^{9}Be (neutron emission rate approximately $2{\times}10^5$ s^{-1}). Fig. 7.16 provides a schematic overview of the experimental setup.

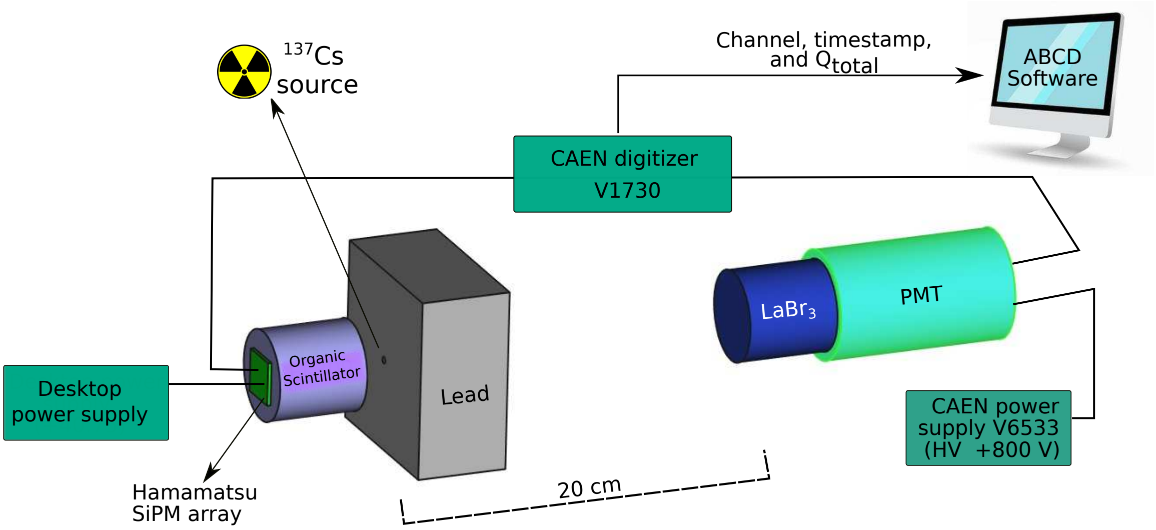

Figure 7.16: Schematic view of the experimental setup, of the Hamamatsu SiPM array coupled to one of the organic scintillators, and in coincidence with $LaBr_3$:Ce detector, using the ^{137}Cs source.

Determination of the energy and time resolution

In this study, the determination of the energy resolution was assessed using a Compton coincidence technique outlined in [103]. This method involved positioning the neutron detector in coincidence with a reference detector, specifically in this case a $LaBr_3$:Ce detector (50 mm diameter × 50 mm thickness, Saint-Gobain), placed face-to-face approximately 20 cm apart. A lead collimator with cuboid dimensions (10 cm × 10 cm × 5 cm) and a 1 cm diameter aperture housed the ^{137}Cs source adjacent to the organic detector, a schematic view of the experimental setup can be seen in Figure 7.16.

The technique takes advantage of the fact that a 661.7 keV gamma ray emitted by the source can be scattered by 180° within the organic scintillator's active volume, depositing approximately 477.4 keV. Subsequently, the back-scattered gamma-ray passes through the collimator's aperture, reaches the reference detector, and deposits its entire energy (184.3 keV). The goal is to construct the energy spectrum of events recorded by the neutron detector in coincidence with the full-energy events corresponding to the back-scattered gamma-rays detected by the $LaBr_3$:Ce detector. In this setup, the spectrum primarily comprises Compton edge events. Then the energy resolution of the detector is determined by fitting a Gaussian function, calculated as $R_E = \mathrm{FWHM}/E_0$, where $E_0 = 477.4$ keV. Considering the geometry, a 1 keV intrinsic resolution of the scattering geometry is attributed to the approximate 3 cm distance between the collimator and the organic scintillator.

For time resolution determination, a similar experimental setup was used without the collimator, employing a ^{22}Na source instead. Coincidences between the two 511 keV gamma rays emitted by the ^{22}Na source were recorded. Offline analysis involved applying a coincidence filter to digitized waveforms from each detector. The Digital Constant Fraction Discrimination (DCFD) parameters (fraction and delay) were optimized to achieve the best time resolution. The delay parameter ranged from 10 ns to 120 ns, and three fraction values (25%, 50%, and 75%) were evaluated. The final time spectrum was constructed using events from the full-energy peak (@511 keV) of the $LaBr_3$:Ce detector and events exceeding 200 keV in the organic scintillation detector.

Determination of the Pulse Shape Discrimination (PSD) capabilities

Each assembled detector's ability to distinguish between neutrons and gamma rays was evaluated using an ^{241}Am-^{9}Be neutron source. Pulse shape discrimination was employed as explained in Subsection 3.2. This method facilitated the calculation of the Figure of Merit (FoM), a parameter indicating the effectiveness of neutron-gamma discrimination. FoM values in this study were derived from events within a light output range approximately corresponding to the Compton edge of the gamma line emitted by the ^{137}Cs source (around ∼480 keVee).

7.3.3 Results and analysis

Signals comparison of the SiPM arrays

Initially, a comparison was made among the output signals generated by the three SiPM arrays. This assessment utilized data obtained from the ^{137}Cs source and the EJ-276G plastic scintillator coupled with the three different SiPM arrays under investigation. Specifically for this section, measurements from the plastic scintillator are presented; however, both plastic and liquid scintillator data are included in the subsequent analyses throughout this study. In Fig. 7.17, typical waveforms for the three scenarios are illustrated. These waveforms correspond to an event with energy equivalent to the Compton edge of the gamma-ray emitted by the ^{137}Cs source.

Upon examining the waveform shapes, it is evident that the rising times are relatively similar across all three cases. However, there is a noticeable difference in decay time, particularly in the Hamamatsu array, which exhibits a slower decay. This distinction is influenced by the recharge time constant of the SiPM microcells, directly related to the cell capacitance (∼RC, see Table 7.2). This parameter characterizes how quickly the microcells can recover after detecting a scintillation photon. Additionally, it is important to note the presence of random fluctuations in the waveform produced by the Ketek configuration, which can impact time resolution.

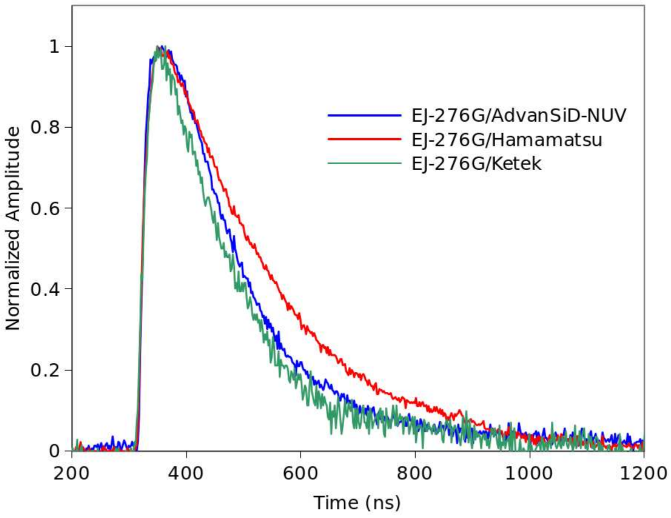

Figure 7.17: Typical waveforms of the EJ-276G scintillator coupled to the Hamamatsu, AdvanSiD-NUV, and Ketek SiPM arrays. The signals correspond to an event of 477.4 keV, so the Compton edge of a 661.7 keV gamma ray.

Energy and Time Performance

The overvoltage applied to each scintillator/SiPM array configuration was meticulously adjusted in function of the energy resolution, with the most favorable performance detailed in Table 4.12. Initially, voltages aligned with the breakdown voltage specified in each SiPM array's datasheet were utilized. Subsequently, overvoltage settings were fine-tuned within the specified range provided by the datasheets.

The energy resolution was evaluated using the Compton coincidence technique outlined in Subsection 7.3.2. Results for one of the configurations are depicted in Fig. 7.18. Figure 7.18a shows the energy spectrum of the $LaBr_3$:Ce detector in coincidence, highlighting red lines indicating energy selections corresponding to the full-energy peak of back-scattered gamma-rays at approximately 184.3 keV. In Fig. 7.18b, the total energy spectrum of the EJ-276G coupled with the Hamamatsu SiPM array is shown as a blue line, while the events coinciding with the full-energy peaks of back-scattered gamma rays are presented as a green line. Energy resolution at 477.4 keV was determined by fitting a Gaussian function to this spectrum.

Detailed energy resolution values for each configuration are summarized in Table 7.5. Notably, the Hamamatsu SiPM exhibits superior performance, particularly when paired with the liquid scintillator. In this specific instance, the Hamamatsu SiPM demonstrates an energy resolution improvement of approximately 45% compared to the AdvanSiD and Ketek configurations.

Table 7.4: Bias voltage applied to each scintillator/SiPM array configuration

Scintillator/SiPM array	OV (V)	Bias Voltage (V)
EJ-276G/AdvanSiD	4	30
EJ-276G/Hamamatsu	2.75	40.75
EJ-276G/Ketek	4.25	29
EJ-309/AdvanSiD	3.5	29.5
EJ-309/Hamamatsu	2.75	40.75
EJ-309/Ketek	3.75	28.5

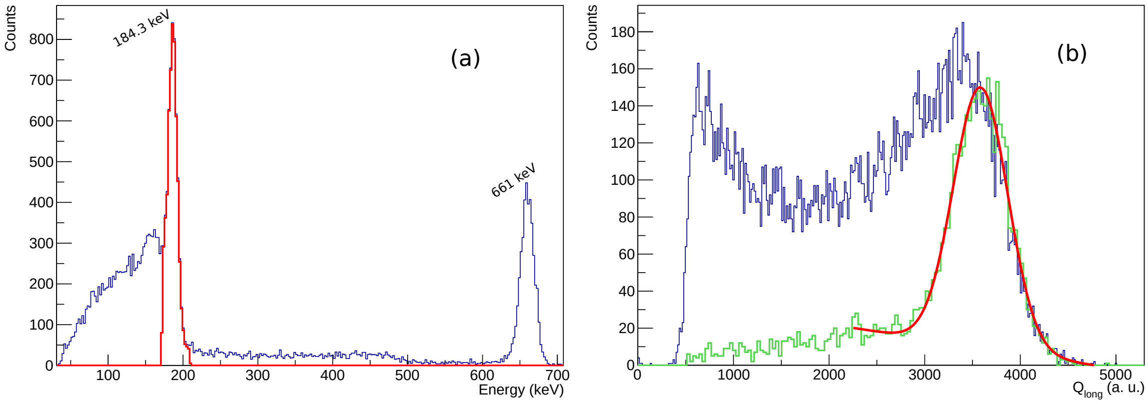

Figure 7.18: Energy spectra corresponding to the ^{137}Cs coincidence experiment between the $LaBr_3$:Ce detector (a) and the EJ-276G/Hamamatsu SiPM array asssembly (b).

For determining time resolution using the ^{22}Na source, we conducted offline waveform analysis. Parameters for Digital Constant Fraction Discrimination (DCFD) were optimized to achieve optimal performance. The best configuration included a 50% fraction for scintillator/SiPM array assemblies, with 120 ns delay for Hamamatsu and AdvanSiD, 80 ns delay for Ketek, and 25% fraction for the LaBr$_3$:Ce detector with 20 ns delay. Subsequently, energy ranges of interest were selected in each detector's spectrum: the 511 keV peak for the LaBr$_3$:Ce detector and all events above 200 keV for the organic detector. A Gaussian fit was applied to the time spectrum to determine the total time resolution (FWHM), calculated as $FWHM^2_{total} = FWHM^2_{LaBr_3} + FWHM^2_{Scintillator/SiPM}$. The LaBr$_3$:Ce detector's time resolution was previously measured as (0.366 ± 0.002) ns, facilitating the determination of the time resolution for each scintillator/SiPM array assembly using the same method.

Figures 7.19 and 7.20 illustrate the time spectra for each scintillator/SiPM array configuration using the ^{22}Na source. Table 7.5 presents the time resolution values for each configuration. Once again, the Hamamatsu SiPM demonstrates superior performance, particularly when coupled with the liquid scintillator. The EJ-309/Hamamatsu configuration exhibits a notable improvement, reducing time resolution by 56% and 59% compared to the AdvanSiD and Ketek configurations, respectively.

It is noteworthy that the Ketek configuration shows poorer results when coupled with the plastic scintillator, likely due to electronic noise evident in Figure 7.17. However, this effect is less pronounced with the liquid scintillator, likely due to its higher light output, which ensures more consistent waveforms.

Table 7.5: Values of the energy and time resolution obtained for each scintillator/SiPM array configuration

Scintillator/SiPM array	Energy Resolution	Time resolution (ns)
EJ-276G/AdvanSiD-NUV	29.0±0.2	1.80 ± 0.01
EJ-276G/Hamamatsu	18.8±0.4	1.043 ± 0.003
EJ-276G/Ketek	25.5±0.2	2.33 ± 0.02
EJ-309/AdvanSiD-NUV	20±2	1.17 ± 0.01
EJ-309/Hamamatsu	10.8±0.4	0.517± 0.004
EJ-309/Ketek	19.7±0.2	1.26± 0.01

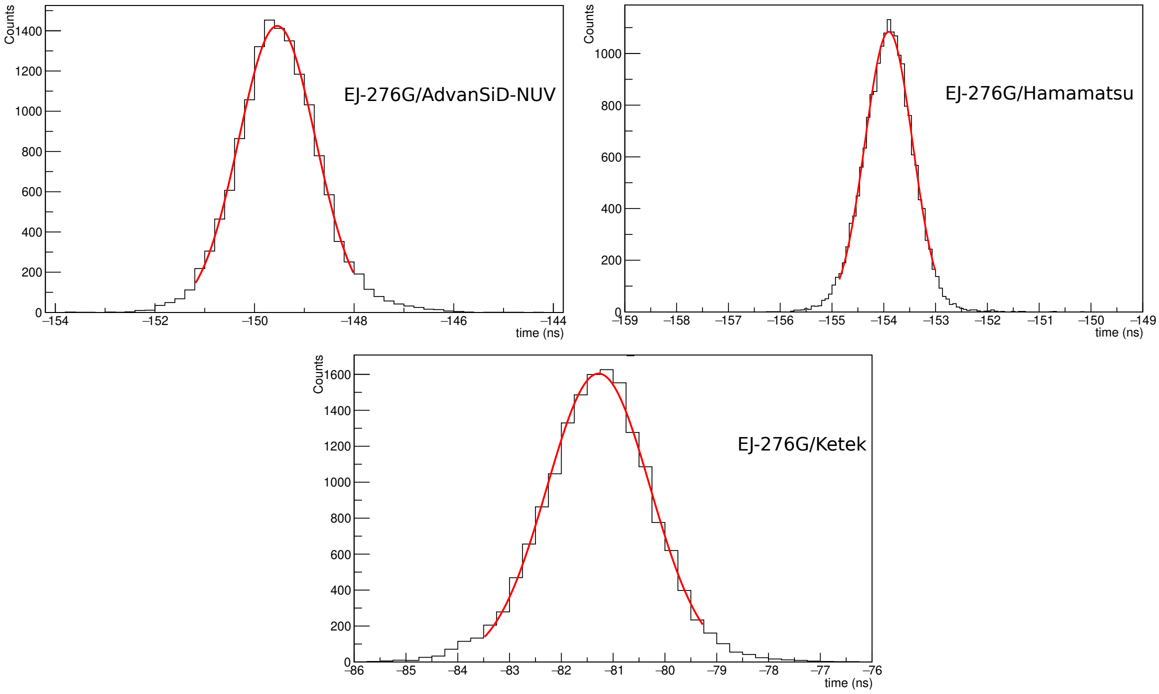

Figure 7.19: Time spectra corresponding to the plastic scintillator (EJ-276G) coupled to each SiPM array, using an ^{22}Na source.

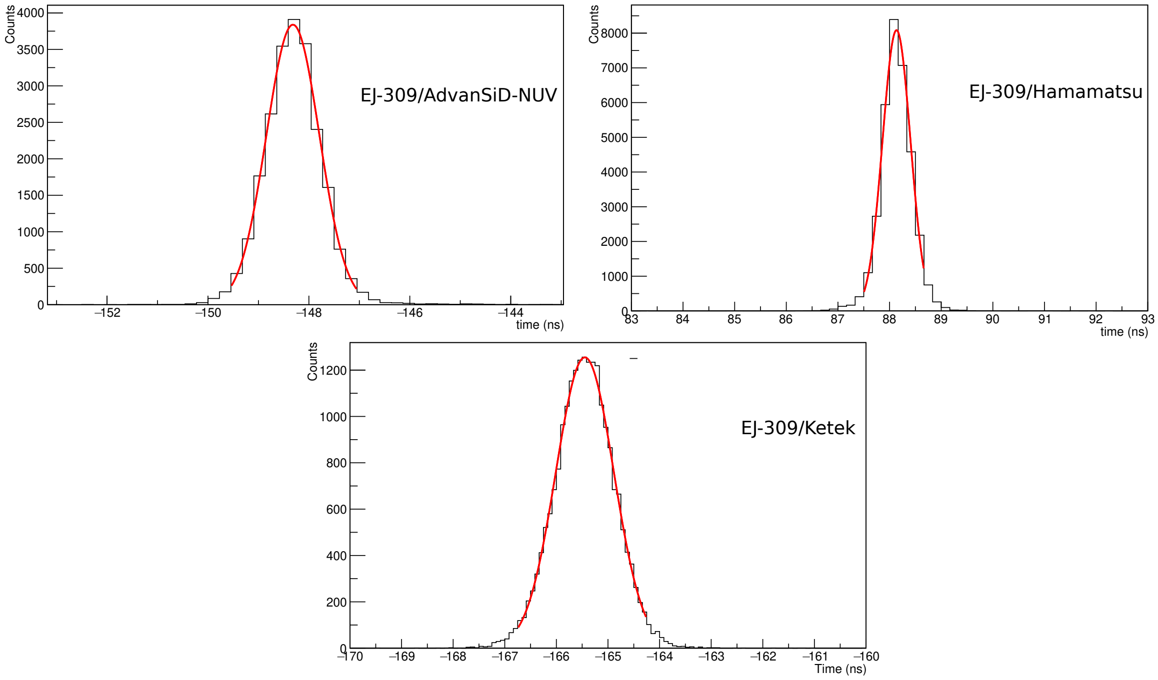

Figure 7.20: Time spectra corresponding to the liquid scintillator (EJ-309) coupled to each SiPM array, using an ^{22}Na source.

Neutron/gamma-ray discrimination capability

We investigated the discrimination capability of each combination of scintillator and SiPM array using an ^{241}Am-^{9}Be source and the double integration method outlined in Subsection 3.2. Initially, we optimized the short and long integration gates for each assembly to maximize the Figure of Merit (FoM). Subsequently, 2D-PSD and PSD plots were generated for each configuration. The 2D-PSD plot represents a histogram of PSD values plotted against Q_{long} values, illustrating events within a light output range corresponding to the Compton edge of the 661.7 keV γ-ray emission from ^{137}Cs. The FoM value was computed from the PSD distribution, as detailed in Subsection 7.3.2.

Figure 7.21 illustrates the 2D-PSD and PSD plots for the EJ-276G coupled with the Hamamatsu SiPM array using an ^{241}Am-^{9}Be source. In the 2D-PSD plot, the events used to construct the PSD distribution are highlighted within a red box. Figure 7.22 presents the 2D-PSD plots for each scintillator and SiPM array configuration. Table 7.6 provides the FoM values and optimized w_{long} and w_{short} values for each configuration. Remarkably, the FoM value for the Hamamatsu configuration when coupled with the EJ-309 outperforms results from AdvanSiD-NUV and Ketek configurations, showing improvements of 43% and 50%, respectively.

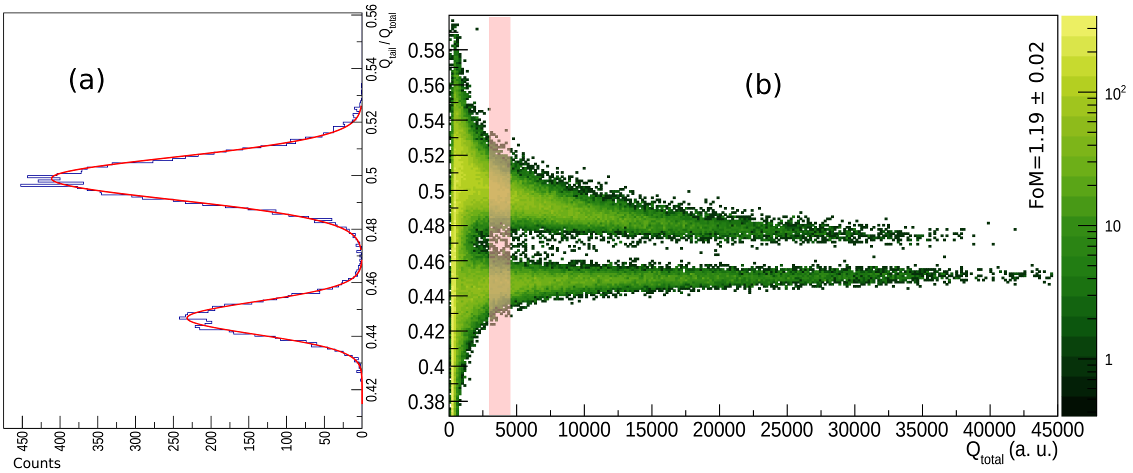

Figure 7.21: 2D-PSD (a) and PSD (b) plots corresponding to the EJ-276G coupled to the Hamamatsu SiPM array, using an ^{241}Am-^{9}Be source.

Table 7.6: Optimized integration windows (w_{long} and w_{short}), and FoM values obtained for each scintillator/SiPM array configuration

Scintillator/SiPM array	w_{long} (ns)	w_{short} (ns)	FoM
EJ-276G/AdvanSiD-NUV	904	240	0.76 ± 0.02
EJ-276G/Hamamatsu	590	220	1.19 ± 0.02
EJ-276G/Ketek	810	176	0.597 ±0.004
EJ-309/AdvanSiD-NUV	586	122	1.15 ± 0.01
EJ-309/Hamamatsu	730	180	2.04 ± 0.01
EJ-309/Ketek	738	190	1.010 ±0.003

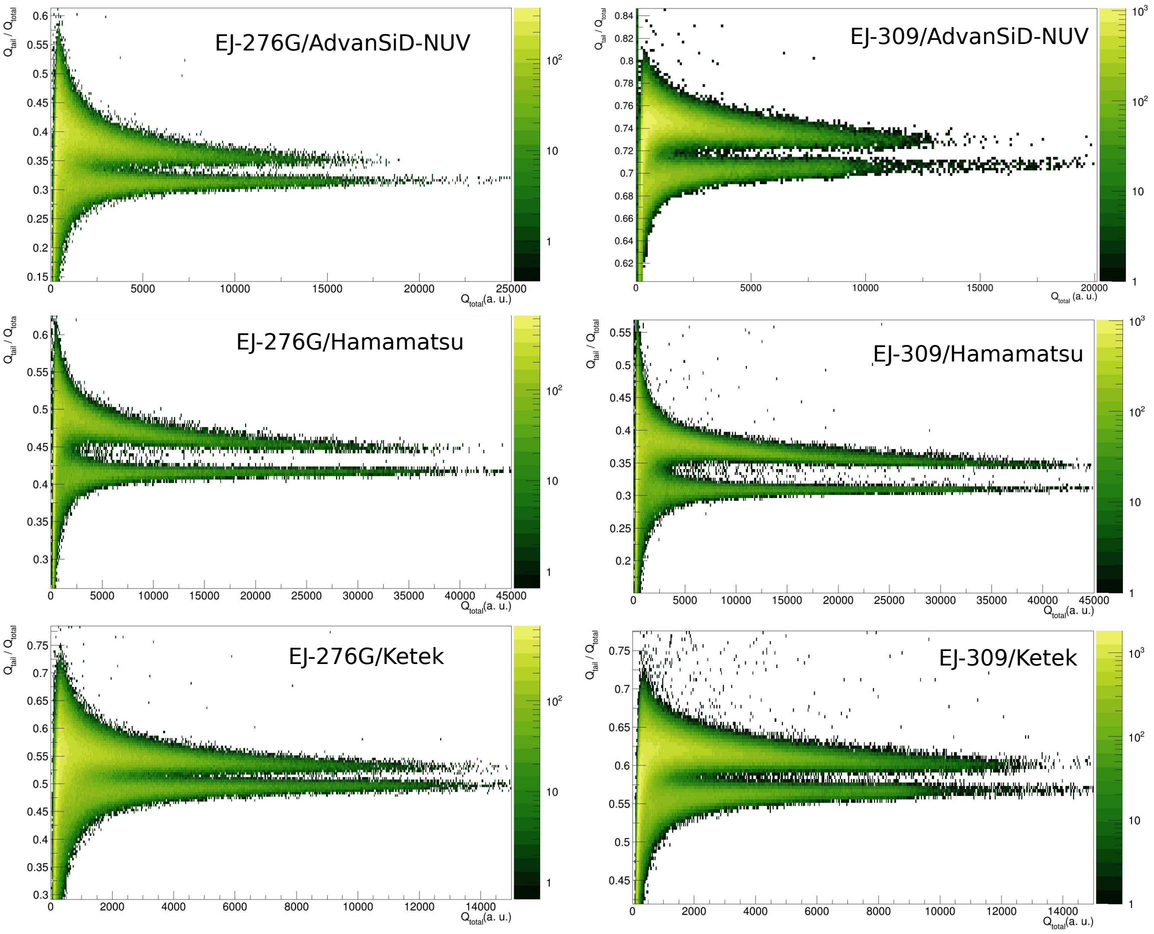

Figure 7.22: 2D-PSD plots corresponding to both organic scintillators (EJ-276G and EJ-309) coupled to the three SiPM arrays, using an ^{241}Am-^{9}Be source.

Discussion of the results

The superior performance of the Hamamatsu SiPM array across all studied parameters in each configuration is attributed to its larger surface area, enabling enhanced light collection per event and thereby generating more photoelectrons per event. Specifically, the Hamamatsu array covers the entire surface of the plastic scintillator and approximately 28% of the liquid scintillator window's surface area. In contrast, the AdvanSiD and Ketek arrays cover about 51% and 28% of the plastic scintillator's surface area, and approximately 13% and 7% of the liquid scintillator's window surface area, respectively. It is important to note that while surface area plays a crucial role in SiPM array performance, other intrinsic characteristics such as photon detection efficiency, dark counts, cross-talk, and after-pulses also impact performance.

To provide a comprehensive comparison of the results reported in previous sections, an analysis based on the number of photoelectrons generated in each scintillator/SiPM configuration is presented. The number of photoelectrons, denoted as N_{phe}, for each scintillator/SiPM array configuration can be estimated using the following equation [104]:

$$N_{phe} = L.O. \times E \times PDE_{int} \times \varepsilon_{L.C.} \tag{7.3}$$

where $\varepsilon_{L.C.}$ is the light output per unit of energy deposited by electrons in the scintillator. According to the manufacturer, for EJ-309, this value is 12300 photons per 1 MeV electron, while for EJ-276G, it is 8000 photons per 1 MeV electron. E is the energy of the electrons generating light inside the scintillator (E = 0.477 MeV, corresponding to the Compton edge of the 0.662 MeV gamma-ray emitted by the ^{137}Cs source). The term PDE_{int} represents the integrated Photon Detection Efficiency of each SiPM at the specific overvoltage used. Lastly, $\varepsilon_{L.C.}$ denotes the light collection efficiency of each scintillator/SiPM array assembly. This includes factors such as the fraction of light reflected off the scintillator walls reaching the window, the area of the window covered by the SiPM array, and the self-attenuation of light by the scintillation material. Given the complexity of these processes, the light collection efficiency for each configuration was determined using a semi-empirical method.

Initially, a gain calibration of the AdvanSiD and Ketek arrays relative to the Hamamatsu array was performed. This calibration was based on the assumption that the response of each SiPM array follows the relationship detailed in the reference [104]:

$$S_{out} = N_{phe} \cdot M + S_{dark} \tag{7.4}$$

where S_{out} represents the output signal (pulse height or integral of the pulse) of a specific event. In our setup, this is equivalent to the Q_{total} value. N_{phe} is the number of photoelectrons, S_{dark} is the detector output charge not generated due to the photoelectric effect, and M is the gain, a particular parameter for each SiPM array.

For this calculation, we assumed S_{dark} to be negligible, an assumption supported by experimental observations. Measurements using a ^{137}Cs source and a LYSO:Ce scintillator (small cube of 10 mm × 10 mm × 10 mm) provided the ratios $M_{Ketek}/M_{Hamamatsu}$

and $M_{AdvanSiD}/M_{Hamamatsu}$.

Subsequently, operating the SiPM arrays at the same overvoltage used for gain calibration with the LYSO:Ce scintillator, we measured the Compton edge position of the 662 keV gamma-ray (^{137}Cs source) with each organic scintillator/SiPM assembly. By applying eqs. 7.4 and 7.3 to each measurement and assuming the $\varepsilon_{L.C.}$ of the EJ-276G/Hamamatsu assembly to be 95% (0.95), we determined the light collection efficiencies of the other configurations. This is a conservative assumption considering the Hamamatsu SiPM array covers the entire scintillator area, the reflector (four layers of polytetrafluoroethylene (PTFE) tape) efficiently reflects most of the produced light, and the light attenuation length of this material far exceeds the scintillator dimensions. Larger uncertainties stem from manufacturer data (light output and emission spectra of the scintillators, and photon detection efficiency curves). However, the overall associated uncertainty does not exceed 10%.

The second column of Table 7.7 presents the number of photoelectrons determined using eq. 7.3 for each scintillator/SiPM array configuration, corresponding to the 0.477 MeV events (Compton edge of the 0.662 MeV gamma-ray). The energy resolution exhibited by a scintillation detector can primarily be expressed by four terms: the intrinsic resolution of the scintillator (non-proportional response), the transfer resolution (quality of reflective material and optical coupling between scintillator and photodetector), which is usually negligible compared to the other terms, the noise contribution, and the statistical contribution of the photoelectrons [105]. In our case, using the same scintillators, if the obtained energy resolution values are normalized to the number of photoelectrons created, the resulting differences will mainly be attributed to the noise contribution of the SiPM (the readout board is the same for the three studied SiPM arrays). The limiting resolution solely based on statistical fluctuations in the number of photoelectrons created in the SiPM array yields the following energy resolution: $R_{E|stat} = \dfrac{2.35}{\sqrt{N_{phe}}}$ [23]. Thus, by multiplying the energy resolution values by the square root of N_{phe}, a constant equal to 2.35 should be obtained if the rest of the terms contributing to the energy resolution are negligible (intrinsic resolution of the scintillator, electronic noise, particularly after-pulsing, and cross-talk [93, 105]). The results are reported in the third column of Table 7.7.

The Ketek SiPM array shows the best performance in terms of energy resolution for both scintillators. AdvanSiD performs better than Hamamatsu only when coupled to the plastic, while both SiPM arrays perform similarly when coupled to the liquid. The configuration with the EJ-309/Ketek yields the closest result to 2.35, indicating that the energy resolution is more influenced by statistical fluctuations, suggesting a low contribution of electronic noise compared to the other configurations. The larger values for the plastic are likely due to the non-proportional response of this scintillation material. It is worth mentioning that the EJ-276G is an EJ-276D scintillator with a secondary dye (wavelength shifter) added, which can introduce this kind of behavior.

Despite the Ketek array covering a smaller area in both detector configurations compared to the other two arrays, resulting in fewer photoelectrons, the detectors assembled using the Ketek array perform better in terms of energy resolution than those assembled with the AdvanSiD array. These results suggest that if a Ketek array covered the same area as the AdvanSiD (or Hamamatsu) array, it would likely achieve better energy resolution.

It is known that the best timing performance is obtained for the fastest detector signals, i.e., organic scintillators coupled to a SiPM array. Rising times are similar (as shown in Fig. 7.17), so signals generated with the greatest number of photoelectrons will exhibit superior timing properties [23]. This fact is verified by the results given in Table 7.5. However, if one wants to compare the results obtained using the studied SiPM arrays, one can proceed similarly to the energy resolution by multiplying the obtained time resolution by the square root of the photoelectrons generated. The outcomes of this multiplication are outlined in the fourth column of Table 7.7, where the result with the lowest value shows the best performance. It is important to note that the energy, E, is used to estimate the number of photoelectrons, according to eq. 7.3, was the average energy of the events considered for the time resolution determination for each detector assembly.

The values obtained suggest that the performance of the Hamamatsu array surpasses that of the other two arrays. However, the AdvanSiD array coupled to the plastic and the Ketek array coupled to the liquid exhibit similar performance to the Hamamatsu-based assemblies. Thus, it is very likely that arrays with similar active areas will produce similar results. The differences between the plastic and liquid results are related to the intrinsic timing properties of the scintillation materials.

The best neutron/gamma-ray discrimination capability with organic scintillators is associated with the number of photoelectrons created per pulse, as verified by the results in Table 7.6. However, normalizing the results by the number of photoelectrons, following the approach used by [101], allows for a comparison of performance between the studied SiPM arrays. The FoM value for each scintillator/SiPM array configuration was divided by the square root of the number of photoelectrons ($\sqrt{N_{phe}}$) created. The results are presented in the fifth column of Table 7.7. Notably, the performances are very similar within a specific scintillator, indicating that the number of photoelectrons is the crucial parameter for achieving better particle discrimination performance.

It is noteworthy that the number of photoelectrons calculated using the semi-empirical method yielded a surprisingly higher value than anticipated. This unexpected finding warrants further investigation. For instance, comparing the EJ-276G/Hamamatsu, where the entire detector area is covered, to the liquid scintillator, which covers only 28% of the detector area, one might assume that the light loss is proportional to the uncovered area. Intuitively, considering the respective light outputs of each scintillator and the fraction of the area covered, one would expect the difference in the number of photoelectrons to be approximately 2.3 times higher in favor of the plastic scintillator. However, the semi-empirical calculation reveals a factor of only 1.1, suggesting a non-linear behavior in the collected light, regardless of the coverage area.

Table 7.7: Number of photoelectrons (N_{phe}) created in each scintillator/SiPM array configuration associated to 0.477 MeV events, energy and time resolutions multiplied by $\sqrt{N_{phe}}$, and the FoM value divided by $\sqrt{N_{phe}}$.

Assembly	N_{phe}	$R_E \cdot \sqrt{N_{phe}}$	$R_T \cdot \sqrt{N_{phe}^*}$	$\frac{FoM}{\sqrt{N_{phe}}} \times 10^{-2}$
EJ-276G/AdvanSiD	555	6.8 ±0.4	25.6±1.4	3.2±0.2
EJ-276G/Hamamatsu	1611	7.5±0.5	25.3±1.3	3.0±0.2
EJ-276G/Ketek	471	5.5±0.3	30.5±1.8	2.8±0.2
EJ-309/AdvanSiD	504	4.5±0.7	16.2±0.9	5.1±0.3
EJ-309/Hamamatsu	1440	4.1±0.4	12.1±0.7	5.4±0.3
EJ-309/Ketek	317	3.5±0.2	13.8±0.8	5.7±0.3

* The number of photoelectrons is associated with the average energy of the events considered for the time resolution determination

7.3.4 Summary

In this research, we compared the performance of two promising organic scintillation materials coupled with three different SiPM arrays, focusing on energy resolution, time resolution, and fast neutron/gamma-ray discrimination. The SiPM arrays tested were the AdvanSiD hybrid array ASD-NUV4S-P-4x4TD (17 mm x 17 mm), the Hamamatsu MPPC S14161-6050HS-04 (24 mm x 24 mm), and the Ketek PA3325-WB-0404 (13 mm x 13 mm). The organic scintillators used were the EJ-276G (plastic) and the EJ-309 (liquid) from Eljen Technology, both known for good neutron/gamma-ray discrimination.

Our objective was to comprehensively assess the performance of these six configurations to identify the most suitable SiPM array for specific applications, particularly for use as an innovative gamma-ray detection system in the ENTRANCE and MULTISCAN 3D projects. The current gamma-detection system in the photofission system of the ENTRANCE project uses a large EJ-200 scintillator coupled to a PMT. In contrast, the proposed detection system will offer good discrimination between gamma rays and neutrons, which is crucial for measuring SNM, and additionally will provide a compact, lightweight, and low-power solution.

To evaluate energy and time resolution, we used a coincidence experiment with a $LaBr_3$:Ce detector. The energy resolution was measured at 477.4 keV using a ^{137}Cs source, while time resolution was determined using a ^{22}Na source by measuring the 511 keV annihilation gamma-rays. Discrimination capability was assessed with an ^{241}Am-^{9}Be source.

The Hamamatsu SiPM array exhibited the best overall performance due to its larger surface area, generating more photoelectrons per pulse. Coupled with the EJ-309 liquid scintillator, it achieved an energy resolution of approximately 10%, a time resolution of 0.52 ns, and a FoM value of about 2. However, when results were normalized by the number of photoelectrons, the Ketek array outperformed in energy resolution and showed comparable time resolution to the AdvanSiD and Hamamatsu arrays. For neutron/gamma-ray discrimination, the Hamamatsu array was superior. Notably, the Ketek array, if it had a similar area to the AdvanSiD, would likely outperform it.

Additionally, the plastic scintillator (EJ-276G) showed better neutron/gamma-ray discrimination when coupled with the studied SiPM arrays compared to a commercial PMT, as demonstrated in our previous work [102]. In conclusion, the findings of this research support the development of future photofission detection systems with compact, lightweight, and low-power solutions suitable for enhancing SNM detection capabilities in projects like ENTRANCE and MULTISCAN 3D. Moving forward, we aim to further optimize these technologies for practical deployment, ensuring robust performance in real-world scenarios.

Chapter 8

Conclusion

The ENTRANCE and MULTISCAN 3D projects, both funded by the EU, represent significant advancements in border security measures. These projects offer innovative solutions to mitigate illicit trafficking and enhance inspection processes through the development of state-of-the-art technologies. By creating user-friendly toolboxes and implementing advanced methods such as X-ray scanning, tagged neutron interrogation, photofission systems, and passive detection technologies, these initiatives aim to revolutionize border control operations.

The primary motivation of this work was to make substantial contributions to both the ENTRANCE and MULTISCAN 3D projects through comprehensive testing, simulation, and refinement of the techniques employed. Recognizing the critical importance of advancing these projects, this work involves a range of activities including experimental tests and field trials, simulations to optimize setups and calculate dose rate maps, proposing enhancements to existing techniques, testing new detectors, and performing proof-of-concept tests to explore alternative neutron source reactions, aiming further to enhance the capabilities and efficiency of these initiatives.

Firstly, this work provides a detailed simulation study of the Rapidly Relocatable Tagged Neutron Inspection System (RRTNIS), a key component of the ENTRANCE project. This system enables the identification of explosives, illicit drugs, and various chemical elements inside containers. The simulation replicated the experimental setup and aimed to optimize the setup geometry, determine the Time of Flight (ToF), analyze energy deposition, investigate back-scattered neutron effects, and compare with experimental data. The determination of Time-of-Flight (ToF) provided valuable insights into the contributions of each component within the inspection area, marking the first successful attempt to accurately simulate the ToF spectrum of the TNIS setup. Furthermore, the comparison between experimental and simulated ToF spectra revealed qualitative agreement, although some discrepancies were noted, likely due to limitations in the simulation's ability to model real neutron interactions. The energy deposition analysis revealed essential gamma-ray peaks for element identification. The study of back-scattered neutrons demonstrated their significant contribution to the correlated background, particularly with a carbon target, which is crucial for interpreting ToF spectra and improving material identification accuracy. Optimization of the configuration setup indicated that attaching the polyethylene box to the detector frame was ideal, but practical constraints required a 22.5 cm distance between the box and the frame. This configuration minimizes background noise and ensures clear event separation between the target and the frame.

Additionally, significant contributions were made during the field tests conducted at the Port of Rijeka in May 2023. The objective of the field test was to evaluate the performance of all the techniques involved in detecting hazardous and illegal contraband within the ENTRANCE project systems. In particular, our group made a substantial contribution to the RRTNIS, including the mounting and dismounting of the system at the port, participating in measurements, and analyzing results. Over three weeks, 18 mock-up containers with various organic materials and 18 commercial containers with diverse items were inspected. The system successfully identified explosive materials and demonstrated a moderate success in detecting cocaine, with some misclassifications due to overestimation of nitrogen content. Challenges included the identification of benign materials, as drugs and difficulties posed by iron in the energy spectrum, suggesting a need for a higher energy threshold in the unfolding process. Enhancements to algorithms and analysis techniques, such as incorporating compound spectra and refining the k-nearest neighbors (kNN) algorithm, were recommended to improve material identification. Despite these areas for improvement, the RRTNIS system demonstrated stable performance and reliability, proving effective in a real-world port setting.

Moreover, this work explored the feasibility of using the ^{9}Be(d,n)^{10}B nuclear reaction to produce the neutron source needed for the MULTISCAN 3D project in the neutron interrogation technique. The experimental investigation at the Van de Graaff CN accelerator at the INFN (National Institute of Nuclear Physics) in Legnaro, using a 4.7 MeV deuteron beam, demonstrated the potential of this nuclear reaction to generate a continuous neutron spectrum for material interrogation and avoids the need for tritium, a radioactive isotope used in the ENTRANCE project for neutron generation. Tritium-based systems presents significant safety and logistical challenges. In contrast, the ^{9}Be(d,n)^{10}B reaction offers a safer and more manageable alternative. The successful proof-of-concept experiments identified characteristic gamma peaks in various materials such as graphite, aluminum, iron, and copper. Despite some discrepancies between experimental and simulated neutron energy spectra, the results validated the ^{9}Be(d,n)^{10}B reaction for neutron interrogation in particular to be use in inorganic materials. Further explorations could involve increasing the deuteron energy to 5.5 MeV, thereby producing higher-energy neutrons. Additionally, tests could be conducted using a lithium target (^{7}Li(d,n)^{8}Be), which may provide more suitable neutron energies for identifying both organic and inorganic materials. However, converting the measured time-of-flight (ToF) into a distance for element localization in the continuous neutron spectrum remains a challenge, which could be addressed in future research. The use of a beryllium target could offer significant advantages for the MULTISCAN 3D project's goal of identifying special nuclear materials (SNM) using thermal neutrons. A beryllium target enables faster neutron thermalization and delivers a higher neutron flux at deuteron energies above 2 MeV, making it a more effective option compared to the DT reaction for this application.

Furthermore, this work introduced two innovative detection systems for the photofission system of the ENTRANCE and MULTISCAN 3D projects, intended for identifying the illegal transportation of SNM inside containers. The innovative detection systems focused on a flexible Lithium Tetraborate thermal neutron scintillator and a compact gamma-ray detection unit. The ZnS:Ag/LiBO/PDMS neutron detector demonstrated high thermal neutron efficiency, excellent flexibility, and superior gamma-ray rejection. For gamma-ray detection, organic scintillators paired with SiPM arrays were tested, with the Hamamatsu array showing the best overall performance.

The novel ZnS:Ag/LiBO/PDMS neutron detector demonstrated a relative thermal neutron detection efficiency of 57% compared to a commercial detector (EJ-420), with potential for enhancement through optimized LiBO concentrations. It showed excellent flexibility, with mechanical resilience allowing for a curvature radius as small as 1.5 mm, suitable for compact and flexible applications. The superior gamma-ray rejection capabilities were demonstrated with a Gamma Rejection Ratio (GRR) below 10^{-11}, essential for precise neutron detection amid high photon backgrounds during SNM irradiation. Monte Carlo simulations using Geant4 v10.7 validated the detector's performance, revealing that only 10% of neutron captures produce measurable events. The scintillator showed a light output of $9000 \pm 5\%$ photoelectrons per neutron capture event. Additionally, a hybrid assembly, tested with the ZnS/LiBO/PDMS scintillator and plastic scintillators (EJ-276G and EJ-299), demonstrated good discrimination between thermal neutrons, fast neutrons, and gamma-rays. The ZnS/LiBO/PDMS scintillator emerges as a promising alternative to traditional ^{3}He proportional counters, offering a good performance and adaptability for various geometries and environmental conditions.

The compact gamma-ray detection unit, consisting of an organic scintillator capable of detecting and distinguishing between gamma-rays and fast neutrons, was coupled to a SiPM array instead of a conventional PMT, aiming for a low-SWaP (Size, Weight, and Power) solution. The performance of two medium-sized organic scintillators (EJ-276G and EJ-309) coupled with three different SiPM arrays (AdvanSiD-NUV ASD-NUV4S-P-4x4TD, Hamamatsu S14161-6050HS-04, Ketek PA3325-WB-0404) was evaluated in terms of energy resolution, time resolution, and neutron/gamma-ray discrimination performance for each configuration. The Hamamatsu SiPM array exhibited the best overall performance due to its larger surface area, generating more photoelectrons per pulse. Coupled with the EJ-309 liquid scintillator, it achieved an energy resolution of approximately 10%, a time resolution of 0.52 ns, and a FoM value of about 2. However, when results were normalized by the number of photoelectrons, the Ketek array outperformed in energy resolution and showed comparable time resolution to the AdvanSiD and Hamamatsu arrays. For neutron/gamma-ray discrimination, the Hamamatsu array was superior. Notably, the Ketek array, if it had a similar area to the AdvanSiD, would likely outperform it.

In conclusion, the detailed study of the two proposed detection systems confirms their suitability for integration into the photofission systems of the ENTRANCE and MULTISCAN 3D projects. Future work will focus on further optimizing these technologies for practical use, ensuring they perform effectively in real-world conditions.

8.1 Future Perspectives

The ENTRANCE project represents a significant advancement in border security, building upon the foundation laid by the C-BORD initiative. While C-BORD set the stage with integrated non-intrusive inspection technologies, ENTRANCE has further refined these techniques, notably by incorporating artificial intelligence to enhance material recognition and decision-making processes. This evolution has resulted in a robust system, as demonstrated by the successful field tests in Rijeka, which highlighted the high accuracy and functionality of the RRTNIS system.

However, despite these successes, there are still areas for improvement. The system's effectiveness can be further enhanced by optimizing algorithmic techniques and refining the geometry of the setup. For the algorithm aspect, the k-nearest neighbors (kNN) method used for triangle identification could be improved with the incorporation of additional samples and more detailed data for each sample. This would enhance its ability to model the behavior of different organic materials, improving classification accuracy.

Regarding the setup geometry, practical constraints, such as the supporting legs of the detector frame, currently prevent the polyethylene box from being fully attached to the frame. Future improvements could focus on overcoming these constraints to achieve this configuration, which would further reduce background noise and enhance the separation of events from the target and the frame.

On the other hand, the MULTISCAN 3D project represents a more ambitious endeavor, aiming to develop a state-of-the-art, all-in-one inspection system utilizing advanced laser-plasma technologies. As this project is still in its early stages, significant research and development are required to fully realize its potential. From our perspective, it would be valuable to investigate the ^{7}Li(d,n)^{8}Be nuclear reaction as an alternative neutron source for the interrogation technique. While our proof of concept has demonstrated promising results with the ^{9}Be(d,n)^{10}B reaction, exploring a lithium target could provide additional benefits. As demonstrated in our simulations, where the lithium reaction produces higher-energy neutrons compared to the beryllium reaction, which increases the likelihood of identifying both organic and inorganic materials more effectively, thus improving the overall performance and sensitivity of the system.

The research team working on neutron source generation using advanced laser-plasma technologies in the MULTISCAN 3D project has primarily focused on the deuterium-deuterium reaction ($d(d,n)^{3}$He). In their experiments, the laser operates at a 1 Hz repetition rate in bursts of 75 shots, with deuterium ions being accelerated to energies up to 1 MeV and directed toward a deuterated polyethylene thin foil. This interaction produces neutrons with an average energy of 2.5 MeV, and the measured neutron yield is 1142 ± 59 neutrons per shot in the 1.5-4 MeV energy range [106].

The group aims to increase the neutron flux to 10^{10} neutrons per second by utilizing a kHz repetition rate laser [107], while maintaining the laser's compact size to ensure its portability for a broad range of applications beyond the MULTISCAN 3D project. Despite increasing the repetition rate will boost the neutron yield, it may be more efficient to use lithium or beryllium targets for the neutron production, rather than relying on the deuterium-deuterium reaction. As shown in Figure 3.7, the deuterium-deuterium reaction produces fewer neutrons compared to reactions involving lithium or beryllium targets. Therefore, the next optimal step could be to test the $^{9}\mathrm{Be}(d,n)^{10}\mathrm{B}$ and $^{7}\mathrm{Li}(d,n)^{8}\mathrm{Be}$ reactions using advanced laser-plasma technologies.

Bibliography

[1] EU position in world trade - European Commission (2024). URL `https://policy.trade.ec.europa.eu/eu-trade-relationships-country-and-region/eu-position-world-trade_en`.

[2] The EU's position in world trade in figures (infographic) (2018). URL `https://www.europarl.europa.eu/topics/en/article/20180703STO07132/the-eu-s-position-in-world-trade-in-figures-infographic`.

[3] Nautic, P. Maritime Industry: The Backbone of Global Trade - Primo Nautic. URL `https://primonautic.com/blog/maritime-industry-global-trade/`.

[4] Maritime - European Commission (2024). URL `https://transport.ec.europa.eu/transport-modes/maritime_en`.

[5] Criminal Networks in EU Ports: Risks and challenges for Law Enforcement. URL `https://www.europol.europa.eu/publications-events/publications/criminal-networks-in-eu-ports-risks-and-challenges-for-/law-enforcement`.

[6] Public perception of illicit tobacco trade - European Commission. URL `https://anti-fraud.ec.europa.eu/public-perception-illicit-tobacco-trade_en`.

[7] Alliance of European ports against drug trafficking launched. EU, 300 tons of cocaine seized each year (2024). URL `https://www.eunews.it/en/2024/01/24/alliance-eu-ports-drug-trafficking/`.

[8] MeesterCor. Leading company in the field of customs and int. trade law. URL `https://dr-customs.eu/`.

[9] Ihantola, S. *et al.* European Reference Network for Critical Infrastructure Protection: - Novel Detection Technologies for Nuclear Security (2018). URL `https://publications.jrc.ec.europa.eu/repository/handle/JRC112304`.

[10] Yang, H. Active Interrogation using Photofission Technique for Nuclear Materials Control and Accountability. Tech. Rep. 11-3035, Battelle Energy Alliance, LLC, Idaho Falls, ID (United States) (2016). `https://doi.org/10.2172/1303155`.

[11] ENTRANCE : Efficient Risk-based Inspection of freight Crossing borders without disrupting business - ENTRANCE at a glance. URL `https://www.entrance-h2020.eu/page/home.php`.

[12] Home - Multiscan3D. URL `https://multiscan3d-h2020.eu/`.

[13] Multiscan 3D project, Laser-plasma based source 3D Tomography for cargo inspection. URL `https://cordis.europa.eu/project/id/101020100`.

[14] EfficieNT Risk-bAsed iNspection of freight Crossing bordErs without disrupting business | ENTRANCE Project | Fact Sheet | H2020. URL `https://cordis.europa.eu/project/id/883424`.

[15] Pérot, B. *et al.* Sea container inspection with tagged neutrons. *EPJ Nuclear Sciences & Technologies* **7**, 6 (2021). `https://doi.org/10.1051/epjn/2021004` .

[16] Perot, B. *et al.* The EURITRACK project: development of a tagged neutron inspection system for cargo containers **6213**, 621305 (2006). `https://doi.org/10.1117/12.665380` .

[17] Cester, D. *et al.* Special nuclear material detection with a mobile multi-detector system. *Nuclear Instruments and Methods in Physics Research Section A: Accelerators, Spectrometers, Detectors and Associated Equipment* **663** (1), 55–63 (2012). `https://doi.org/10.1016/j.nima.2011.10.011` .

[18] MODULAR DETECTION SYSTEM FOR SPECIAL NUCLEAR MATERIAL | MODES_snm Project | Fact Sheet | FP7. URL `https://cordis.europa.eu/project/id/284842/it`.

[19] Agelou, M. *et al.* Detecting special nuclear materials inside cargo containers using photofission 936–939 (2009). `https://doi.org/10.1109/NSSMIC.2009.5401567`, iSSN: 1082-3654 .

[20] Deyglun, C. *et al.* Passive and Active Correlation Techniques for the Detection of Nuclear Materials. *IEEE Transactions on Nuclear Science* **61** (4), 2228–2234 (2014). `https://doi.org/10.1109/TNS.2014.2315714` .

[21] Perot, B. *et al.* Detection of special nuclear materials with tagged neutrons 1–4 (2016). `https://doi.org/10.1109/NSSMIC.2016.8069917` .

[22] C-BORD Project - Effective Container Inspection at BORDer Control Points - Effective Container Inspection at BORDer Control Points. URL `https://www.cbord-h2020.eu/`.

[23] Knoll, G. F. *Radiation detection and measurement* (Wiley, New York, 1979).

[24] Krane, K. S. & Halliday, D. *Introductory nuclear physics* (Wiley, New York, 1987).

[25] Neutron Energy | Classification of Neutrons | nuclear-power.com. URL `https://www.nuclear-power.com/nuclear-power/reactor-physics/atomic-nuclear-physics/fundamental-particles/neutron/neutron-energy/`.

[26] Lamarsh, J. R. & Baratta, A. J. *Introduction to nuclear engineering* 3rd ed edn. Addison-Wesley series in nuclear science and engineering (Prentice Hall, Upper Saddle River, N.J, 2001).

[27] Reilly, D., Ensslin, N., Smith, H. J. & Kreiner, S. Passive nondestructive assay of nuclear materials. Tech. Rep. NUREG/CR-5550; LA-UR-90-732, Nuclear Regulatory Commission, Washington, DC (United States). Office of Nuclear Regulatory Research; Los Alamos National Lab., NM (United States) (1991). `https://doi.org/https://doi.org/10.2172/1303155`.

[28] Delgado Alvarez, J. C. *Design and characterization of the neutron-gamma detection module of the DRAGON project.* Ph.D. thesis, University of Padova, Italy (2021). URL `https://thesis.unipd.it/handle/20.500.12608/1016`.

[29] Sodern | Space Optronics and Neutron Technology. URL `https://sodern.com/en/`.

[30] De Sainte Foy, C. *et al.* Optimization of the ENTRANCE Rapidly Relocatable Tagged Neutron Inspection System 1–7 (2022). `https://doi.org/10.1109/NSS/MIC44845.2022.10399221` .

[31] Perot, B. *et al.* Measurement of 14MeV neutron-induced prompt gamma-ray spectra from 15 elements found in cargo containers. *Applied Radiation and Isotopes* **66** (4), 421–434 (2008). `https://doi.org/10.1016/j.apradiso.2007.11.011` .

[32] Carasco, C. *et al.* In-field tests of the EURITRACK tagged neutron inspection system. *Nuclear Instruments and Methods in Physics Research Section A: Accelerators, Spectrometers, Detectors and Associated Equipment* **588** (3), 397–405 (2008). `https://doi.org/10.1016/j.nima.2008.01.097` .

[33] NNDC | National Nuclear Data Center. URL `https://www.nndc.bnl.gov/`.

[34] El Kanawati, W. *et al.* Acquisition of prompt gamma-ray spectra induced by 14MeV neutrons and comparison with Monte Carlo simulations. *Applied Radiation and Isotopes* **69** (5), 732–743 (2011). `https://doi.org/10.1016/j.apradiso.2011.01.010` .

[35] Gozani, T. Fission Signatures for Nuclear Material Detection. *IEEE Transactions on Nuclear Science* **56** (3), 736–741 (2009). `https://doi.org/10.1109/TNS.2009.2015309` .

[36] Sari, A. *et al.* Evaluation of delayed neutron yields and time spectra from photofission of ^{238} U induced by *Bremsstrahlung* photons below 9 MeV. *EPJ Web of Conferences* **284**, 11002 (2023). `https://doi.org/10.1051/epjconf/202328411002` .

[37] Sari, A. *et al.* Deployment of the First Photofission Measurement System Dedicated to SNM Detection in Europe: Outcomes and Future Prospects 1–2 (2019). `https://doi.org/10.1109/NSS/MIC42101.2019.9059765` .

[38] Kimura, R., Sagara, H. & Chiba, S. Principle validation of nuclear fuel material isotopic composition measurement method based on photofission reactions. *Journal of Nuclear Science and Technology* **53** (12), 1978–1987 (2016). `https://doi.org/10.1080/00223131.2016.1177471` .

[39] Bingham, R. & Trines, R. Introduction to Plasma Accelerators: the Basics. *CERN Yellow Reports* 67 Pages (2016). `https://doi.org/10.5170/CERN-2016-001.67` .

[40] Hajima, R. *et al.* Application of Laser Compton Scattered gamma-ray beams to nondestructive detection and assay of nuclear material. *The European Physical Journal Special Topics* **223** (6), 1229–1236 (2014). `https://doi.org/10.1140/epjst/e2014-02177-y` .

[41] Alejo, A. *et al.* Recent advances in laser-driven neutron sources. *Il Nuovo Cimento C* **38** (6), 1–7 (2016). `https://doi.org/10.1393/ncc/i2015-15188-8` .

[42] Alvarez, J. *et al.* Laser Driven Neutron Sources: Characteristics, Applications and Prospects. *Physics Procedia* **60**, 29–38 (2014). `https://doi.org/10.1016/j.phpro.2014.11.006` .

[43] Chichester, D. L. *Production and Applications of Neutrons Using Particle Accelerators* (The INL is a U.S. Department of Energy National Laboratory operated by Battelle Energy Alliance, 2019).

[44] Francesc Salvat, J., Sempau, J. & Acosta, E. *PENELOPE, a code system for Monte Carlo simulation of electron and photon transport* Nea/nsc/doc(2001)19 edn (Issy-les-Moulineaux, France, 2001).

[45] Geant4. URL `https://geant4.web.cern.ch//`.

[46] EXFOR: Experimental Nuclear Reaction Data. URL `https://www-nds.iaea.org/exfor/`.

[47] Pino, F. *et al.* Advances on the development of the detection system of C-BORD's rapidly relocatable tagged neutron inspection. *International Journal of Modern Physics: Conference Series* **48**, 1860125 (2018). `https://doi.org/10.1142/S2010194518601254` .

[48] Sardet, A. *et al.* Performances of C-BORD's Tagged Neutron Inspection System for Explosives and Illicit Drugs Detection in Cargo Containers. *IEEE Transactions on Nuclear Science* **68** (3), 346–353 (2021). `https://doi.org/10.1109/TNS.2021.3050002` .

[49] Fontana, C. L. *et al.* Detection System of the First Rapidly Relocatable Tagged Neutron Inspection System (RRTNIS), Developed in the Framework of

the European H2020 C-BORD Project. *Physics Procedia* **90**, 279–284 (2017). `https://doi.org/10.1016/j.phpro.2017.09.010` .

[50] Fontana, C. L. *et al.* A distributed data acquisition system for signal digitizers with on-line analysis capabilities 1–5 (2017). `https://doi.org/10.1109/NSSMIC.2017.8533063` .

[51] Fontana, C. L. *et al.* A distributed data acquisition system for nuclear detectors. *International Journal of Modern Physics: Conference Series* **48**, 1860118 (2018). `https://doi.org/10.1142/S2010194518601187` .

[52] Pino, F. *et al.* Detection module of the C-BORD Rapidly Relocatable Tagged Neutron Inspection System (RRTNIS). *Nuclear Instruments and Methods in Physics Research Section A: Accelerators, Spectrometers, Detectors and Associated Equipment* **986**, 164743 (2021). `https://doi.org/10.1016/j.nima.2020.164743` .

[53] CAEN - Tools for Discovery (2011). URL `https://www.caen.it/`.

[54] CEA. CEA/CEA PARIS-SACLAY (2013). URL `https://www.cea.fr/paris-saclay/Pages/Accueil.aspx`.

[55] Carasco, C. *et al.* Photon attenuation and neutron moderation correction factors for the inspection of cargo containers with tagged neutrons. *Nuclear Instruments and Methods in Physics Research Section A: Accelerators, Spectrometers, Detectors and Associated Equipment* **582** (2), 638–643 (2007). `https://doi.org/10.1016/j.nima.2007.09.002` .

[56] What is the k-nearest neighbors algorithm? | IBM (2021). URL `https://www.ibm.com/topics/knn`.

[57] Fontana, C. *et al.* Performance comparison between signal digitizers and low-cost digital oscilloscopes: spectroscopic, pulse shape discrimination and timing capabilities for nuclear detectors. *Journal of Instrumentation* **15** (06), P06020–P06020 (2020). `https://doi.org/10.1088/1748-0221/15/06/P06020` .

[58] Pino, F. *et al.* The light output and the detection efficiency of the liquid scintillator EJ-309. *Applied Radiation and Isotopes* **89**, 79–84 (2014). `https://doi.org/10.1016/j.apradiso.2014.02.016` .

[59] Ene, D. *et al.* Global characterisation of the GELINA facility for high-resolution neutron time-of-flight measurements by monte carlo simulations **618** (1), 54–68. `https://doi.org/10.1016/j.nima.2010.03.005` .

[60] Pino, F. *et al.* Novel flexible and conformable composite neutron scintillator based on fully enriched lithium tetraborate. *Scientific Reports* **13** (1), 4799 (2023). `https://doi.org/10.1038/s41598-023-31675-9` .

[61] Delgado, J. *et al.* Comparative Study of SiPM Arrays Performances for Neutron Detectors. *IEEE Transactions on Nuclear Science* **71** (5), 1144–1153 (2024). `https://doi.org/10.1109/TNS.2024.3387075` .

[62] Fisher, B. *et al.* Fast neutron detection with 6Li-loaded liquid scintillator. *Nuclear Instruments and Methods in Physics Research Section A: Accelerators, Spectrometers, Detectors and Associated Equipment* **646** (1), 126–134 (2011). `https://doi.org/10.1016/j.nima.2011.04.019` .

[63] Pino, F. *et al.* Detecting fast and thermal neutrons with a boron loaded liquid scintillator, EJ-339A. *Applied Radiation and Isotopes* **92**, 6–11 (2014). `https://doi.org/10.1016/j.apradiso.2014.05.025` .

[64] Cester, D. *et al.* A novel detector assembly for detecting thermal neutrons, fast neutrons and gamma rays. *Nuclear Instruments and Methods in Physics Research Section A: Accelerators, Spectrometers, Detectors and Associated Equipment* **830**, 191–196 (2016). `https://doi.org/10.1016/j.nima.2016.05.079` .

[65] Bergeron, D. *et al.* Optimum lithium loading of a liquid scintillator for neutron and neutrino detection. *Nuclear Instruments and Methods in Physics Research Section A: Accelerators, Spectrometers, Detectors and Associated Equipment* **953**, 163126 (2020). `https://doi.org/10.1016/j.nima.2019.163126` .

[66] Nguyen, L. Q. *et al.* Boron-loaded organic glass scintillators. *Nuclear Instruments and Methods in Physics Research Section A: Accelerators, Spectrometers, Detectors and Associated Equipment* **988**, 164898 (2021). `https://doi.org/10.1016/j.nima.2020.164898` .

[67] Grodzicka-Kobylka, M. *et al.* Comparison of detectors with pulse shape discrimination capability for simultaneous detection of gamma-rays, slow and fast neutrons. *Nuclear Instruments and Methods in Physics Research Section A: Accelerators, Spectrometers, Detectors and Associated Equipment* **1019**, 165858 (2021). `https://doi.org/10.1016/j.nima.2021.165858` .

[68] Carturan, S. *et al.* Flexible scintillation sensors for the detection of thermal neutrons based on siloxane 6LiF containing composites: Role of 6LiF crystals size and dispersion. *Nuclear Instruments and Methods in Physics Research Section A: Accelerators, Spectrometers, Detectors and Associated Equipment* **925**, 109–115 (2019). `https://doi.org/10.1016/j.nima.2019.01.088` .

[69] Khalilzadeh, N. *et al.* Formation and characterization of ultrafine nanophosphors of lithium tetraborate (Li2B4O7) for personnel and medical dosimetry. *Journal of Materials Research and Technology* **5** (3), 206–212 (2016). `https://doi.org/10.1016/j.jmrt.2015.11.002` .

[70] Frangville, C. *et al.* Nanoparticles-loaded plastic scintillators for fast/thermal neutrons/gamma discrimination: Simulation and results. *Nuclear Instruments and Methods in Physics Research Section A: Accelerators, Spectrometers, Detectors and Associated Equipment* **942**, 162370 (2019). `https://doi.org/10.1016/j.nima.2019.162370` .

[71] Moszynski, M., Kapusta, M., Mayhugh, M., Wolski, D. & Flyckt, S. Absolute light output of scintillators. *IEEE Transactions on Nuclear Science* **44** (3), 1052–1061 (1997). `https://doi.org/10.1109/23.603803` .

[72] Neutron detection for portal monitors perfomance evaluation. Tech. Rep., Luxium Solutions (2011).

[73] Katagiri, M. *et al.* Scintillation materials for neutron imaging detectors. *Nuclear Instruments and Methods in Physics Research Section A: Accelerators, Spectrometers, Detectors and Associated Equipment* **529** (1-3), 274–279 (2004). `https://doi.org/10.1016/j.nima.2004.04.165` .

[74] Tarasov, O. & Bazin, D. LISE++: Radioactive beam production with in-flight separators. *Nuclear Instruments and Methods in Physics Research Section B: Beam Interactions with Materials and Atoms* **266** (19-20), 4657–4664 (2008). `https://doi.org/10.1016/j.nimb.2008.05.110` .

[75] Ziegler, J. F., Ziegler, M. D. & Biersack, J. P. SRIM – The stopping and range of ions in matter (2010). *Nuclear Instruments and Methods in Physics Research Section B: Beam Interactions with Materials and Atoms* **268** (11), 1818–1823 (2010). `https://doi.org/10.1016/j.nimb.2010.02.091` .

[76] Al-Adili, A. *et al.* Prompt fission neutron yields in thermal fission of U 235 and spontaneous fission of Cf 252. *Physical Review C* **102** (6), 064610 (2020). `https://doi.org/10.1103/PhysRevC.102.064610` .

[77] Sykora, G. J., Mann, S. E., Mauri, G., Schooneveld, E. M. & Rhodes, N. J. Review of thermal neutron scintillators: Evaluation metrics and future prospects for demanding applications **24**, 100373. `https://doi.org/10.1016/j.omx.2024.100373` .

[78] Grodzicka-Kobylka, M. *et al.* Fast neutron and gamma ray pulse shape discrimination in EJ-276 and EJ-276G plastic scintillators. *Journal of Instrumentation* **15** (03), P03030–P03030 (2020). `https://doi.org/10.1088/1748-0221/15/03/P03030` .

[79] Pawełczak, I. *et al.* Boron-loaded plastic scintillator with neutron-γ pulse shape discrimination capability. *Nuclear Instruments and Methods in Physics Research Section A: Accelerators, Spectrometers, Detectors and Associated Equipment* **751**, 62–69 (2014). `https://doi.org/10.1016/j.nima.2014.03.027` .

[80] Li, J. *et al.* Design and performance evaluation of a compact thermal and fast neutron spectrometer. *Nuclear Instruments and Methods in Physics Research Section A: Accelerators, Spectrometers, Detectors and Associated Equipment* **1063**, 169247 (2024). `https://doi.org/10.1016/j.nima.2024.169247` .

[81] Guzmán-García, K. A. *et al.* Performance of 10B+ZnS(Ag) neutron detectors in RPM for the detection of special nuclear materials. *Radiation Measurements* **107**, 58–66 (2017). `https://doi.org/10.1016/j.radmeas.2017.11.001` .

[82] Ducasse, Q. *et al.* Design of MICADO advanced passive and active neutron measurement system for radioactive waste drums. *Nuclear Instruments and Methods in Physics Research Section A: Accelerators, Spectrometers, Detectors and Associated Equipment* **1005**, 165398 (2021). `https://doi.org/10.1016/j.nima.2021.165398` .

[83] Lehmann, E. & Boillat, P. Advances in scintillator screen technology for neutron imaging. *Nuclear Instruments and Methods in Physics Research Section A: Accelerators, Spectrometers, Detectors and Associated Equipment* **1053**, 168324 (2023). `https://doi.org/10.1016/j.nima.2023.168324` .

[84] Ishikawa, A. *et al.* A comparison between simulation and experimental results for depth profile of 6Li reaction rate in a water phantom of BNCT using a small 6Li-based scintillator neutron detector with an optical fiber. *Radiation Measurements* **133**, 106270 (2020). `https://doi.org/10.1016/j.radmeas.2020.106270` .

[85] Roncali, E. & Cherry, S. R. Application of Silicon Photomultipliers to Positron Emission Tomography. *Annals of Biomedical Engineering* **39** (4), 1358–1377 (2011). `https://doi.org/10.1007/s10439-011-0266-9` .

[86] Guberman, D. *et al.* The Light-Trap: A novel concept for a large SiPM-based pixel for Very High Energy gamma-ray astronomy and beyond. *Nuclear Instruments and Methods in Physics Research Section A: Accelerators, Spectrometers, Detectors and Associated Equipment* **923**, 19–25 (2019). `https://doi.org/10.1016/j.nima.2019.01.052` .

[87] Bisogni, M. G., Del Guerra, A. & Belcari, N. Medical applications of silicon photomultipliers. *Nuclear Instruments and Methods in Physics Research Section A: Accelerators, Spectrometers, Detectors and Associated Equipment* **926**, 118–128 (2019). `https://doi.org/10.1016/j.nima.2018.10.175` .

[88] Dinu, N. Silicon photomultipliers (SiPM) 255–294 (2016). `https://doi.org/10.1016/B978-1-78242-445-1.00008-7` .

[89] Garutti, E. Silicon photomultipliers for high energy physics detectors. *Journal of Instrumentation* **6** (10), C10003–C10003 (2011). `https://doi.org/10.1088/1748-0221/6/10/C10003` .

[90] Sanaei, B., Baei, M. T. & Sayyed-Alangi, S. Z. Characterization of a New Silicon Photomultiplier in Comparison with a Conventional Photomultiplier Tube. *Journal of Modern Physics* **06** (04), 425–433 (2015). `https://doi.org/10.4236/jmp.2015.64046` .

[91] Preston, R. M., Eberhardt, J. E. & Tickner, J. R. Neutron-Gamma Pulse Shape Discrimination Using Organic Scintillators With Silicon Photomultiplier Readout. *IEEE Transactions on Nuclear Science* **61** (4), 2410–2418 (2014). `https://doi.org/10.1109/TNS.2014.2335208` .

[92] Introduction to SiPM. technical note. Tech. Rep., SensL (2017).

[93] Grodzicka-Kobylka, M., Szczesniak, T. & Moszyński, M. Comparison of SensL and Hamamatsu 4×4 channel SiPM arrays in gamma spectrometry with scintillators. *Nuclear Instruments and Methods in Physics Research Section A: Accelerators, Spectrometers, Detectors and Associated Equipment* **856**, 53–64 (2017). `https://doi.org/10.1016/j.nima.2017.03.015` .

[94] Gonzalez-Montoro, A. & Gonzalez, A. J. Performance comparison of large-area SiPM arrays suitable for gamma ray detectors. *Biomedical Physics & Engineering Express* **5** (4), 045013 (2019). `https://doi.org/10.1088/2057-1976/ab0f6e` .

[95] Pino, F. *et al.* Characterization of a medium-sized CLLB scintillator: single neutron/gamma detector for radiation monitoring. *Journal of Instrumentation* **16** (11), P11034 (2021). `https://doi.org/10.1088/1748-0221/16/11/P11034` .

[96] Taggart, M. & Sellin, P. Comparison of the pulse shape discrimination performance of plastic scintillators coupled to a SiPM. *Nuclear Instruments and Methods in Physics Research Section A: Accelerators, Spectrometers, Detectors and Associated Equipment* **908**, 148–154 (2018). `https://doi.org/10.1016/j.nima.2018.08.054` .

[97] Ruch, M. L., Flaska, M. & Pozzi, S. A. Pulse shape discrimination performance of stilbene coupled to low-noise silicon photomultipliers. *Nuclear Instruments and Methods in Physics Research Section A: Accelerators, Spectrometers, Detectors and Associated Equipment* **793**, 1–5 (2015). `https://doi.org/10.1016/j.nima.2015.04.053` .

[98] Shen, F. *et al.* PSD performance of EJ-276 and EJ-301 scintillator readout with SiPM array. *Nuclear Instruments and Methods in Physics Research Section A: Accelerators, Spectrometers, Detectors and Associated Equipment* **1039**, 167148 (2022). `https://doi.org/10.1016/j.nima.2022.167148` .

[99] Boo, J., Hammig, M. D. & Jeong, M. Pulse shape discrimination using a stilbene scintillator array coupled to a large-area SiPM array for hand-held dual particle imager applications. *Nuclear Engineering and Technology* **55** (2), 648–654 (2023). `https://doi.org/10.1016/j.net.2022.10.016` .

[100] Ruch, M. L., Flaska, M. & Pozzi, S. A. Pulse shape discrimination performance of stilbene coupled to low-noise silicon photomultipliers. *Nuclear Instruments and Methods in Physics Research Section A: Accelerators, Spectrometers, Detectors and Associated Equipment* **793**, 1–5 (2015). `https://doi.org/10.1016/j.nima.2015.04.053` .

[101] Grodzicka-Kobylka, M. *et al.* Study of n - gamma discrimination by zero-crossing method with SiPM based scintillation detectors. *Nuclear Instruments and Methods in Physics Research Section A: Accelerators, Spectrometers, Detectors and Associated Equipment* **883**, 159–165 (2018). `https://doi.org/10.1016/j.nima.2017.11.045` .

[102] Pino, F. *et al.* Novel Detector Assembly for Neutron/Gamma-Ray Discrimination Applications Based on Large-Sized Scintillators Coupled to Large Area SiPM Arrays. *IEEE Transactions on Nuclear Science* **69** (4), 668–676 (2022). `https://doi.org/10.1109/TNS.2022.3154015` .

[103] Swiderski, L. *et al.* Measurement of Compton edge position in low-Z scintillators. *Radiation Measurements* **45** (3-6), 605–607 (2010). `https://doi.org/10.1016/j.radmeas.2009.10.015` .

[104] A. Ghassemi, K. K., K. Sato. A technical guide to silicon photomultipliers (MPPC) - Overview | Hamamatsu Photonics. Technical note (2017).

[105] Grodzicka-Kobylka, M. *et al.* Characterization of large TSV MPPC arrays (4 × 4 ch and 8 × 8 ch) in scintillation spectrometry. *Nuclear Instruments and Methods in Physics Research Section A: Accelerators, Spectrometers, Detectors and Associated Equipment* **869**, 153–162 (2017). `https://doi.org/10.1016/j.nima.2017.07.006` .

[106] Osvay, K. *et al.* Fast neutron generation with few-cycle, relativistic laser pulses at 1 hz repetition rate **14** (1), 25302. `https://doi.org/10.1038/s41598-024-75855-7` .

[107] Osvay, K. *et al.* Towards a 10^{10} n/s neutron source with kHz repetition rate, few-cycle laser pulses **139** (7), 574. `https://doi.org/10.1140/epjp/s13360-024-05338-1` .